AN ABSTRACT OF THE DISSERTATION OF

Joel Walenza-Slabe for the degree of Doctor of Philosophy in Materials Science presented on November 28, 2016.

Title: Electronic Conduction and Ionic Diffusion in $(Bi_{0.5}Na_{0.5})TiO_3$-$(Bi_{0.5}K_{0.5})TiO_3$-based Thin Films.

Abstract approved: _____

Brady J. Gibbons

Solid solutions based on the perovskite ferroelectrics $Bi_{0.5}Na_{0.5}TiO_3$ (BNT) and $Bi_{0.5}K_{0.5}TiO_3$ (BKT) might someday replace current Pb-based ferroelectric and piezoelectric devices. This is one goal of the Restrictions on Hazardous Substances (RoHS) guidelines seeking to limit Pb in consumer devices. Although the Bi-based ferroelectrics are well suited to the task for their overall high Curie temperature and good piezoelectric properties, there are still questions about reliability. The primary goal of this research was to advance the understanding of long term reliability in polycrystalline BNT-BKT thin films fabricated by chemical solution deposition (CSD). The constituent cations are highly volatile at the crystallization temperatures, and oxygen vacancies are common to all oxide perovskites. The resulting defects are associated with higher leakage currents, which can reduce long term stability by increasing the frequency of early failures due to localized breakdown events. Research focused on several topics related to electronic and ionic conduction in BNT-BKT thin films.

Mn-doping is a well known technique utilized to decrease electronic current in many perovskite ferroelectrics. A study of the steady state leakage current in Mn-doped 80BNT-20BKT films was performed, including 0 up to 2 mol% Mn. Space charge-limited conduction was found in all films, although the onset of strong injection increased with dopant concentration. The 2 mol% Mn films showed only Ohmic conduction beyond 180 °C and 400 kV/cm. Additionally, ionic conduction processes also play a role

in fatigue and resistance degradation. High temperature transient currents are believed to be directly related to ionic migration. Analysis of these peaks reveal activation energies and mobilities consistent with migration of oxygen vacancies in the 80BNT-20BKT films. However, the transients for Mn-doped films displayed some unusual characteristic of very short, temperature insensitive transient times. This may indicate that a different mechanism is operating in those films.

The binary system (100–*x*)BNT-*x*BKT for *x*=10, 20, 30, and 40 was studied for the steady state leakage current and ionic transport properties. Leakage current decreased dramatically on moving from the rhombohedral *x*=10~20 films to the tetragonal *x*=30~40 films. Other correlations included some evidence of incipient texturing of the tetragonal films, as well as decreasing roughness with larger *x*. The ionic transport properties were again measured in these films. They appear to show a decrease in the mobility of oxygen vacancies with increasing *x*. This may have implications for improving reliability in the future.

The effects of post-annealing at different oxygen partial pressures (pO_2) was attempted in order to determine the majority electronic carrier type. All films tested, which included 80BNT-20BKT, 95(80BNT-20BKT)-5Bi($Ni_{0.5}Ti_{0.5}$)O_3, and 95(80BNT-20BKT)-5$BaTiO_3$, produced results consistent with *n*-type conduction. Also, while the current is generally space charge-limited, there are several key features of the current density-electric field characteristics which were affected by the post-anneal pO_2. Information on the trap density and distribution and the carrier density can be gleaned from analyzing these curves.

Electronic Conduction and Ionic Diffusion in $(Bi_{0.5}Na_{0.5})TiO_3$-$(Bi_{0.5}K_{0.5})TiO_3$-based Thin Films

by
Joel Walenza-Slabe

A DISSERTATION

submitted to

Oregon State University

in partial fulfillment of
the requirements for the
degree of

Doctor of Philosophy

Presented November 28, 2016
Commencement June 2017

Doctor of Philosophy dissertation of Joel Walenza-Slabe presented on November 28, 2016

APPROVED:

Major Professor, representing Materials Science

Director of the Materials Science Program

Dean of the Graduate School

I understand that my dissertation will become part of the permanent collection of Oregon State University libraries. My signature below authorizes release of my dissertation to any reader upon request.

Joel Walenza-Slabe, Author

ACKNOWLEDGEMENTS

I would like to thank above all my children's mother, Casey, for her sacrifices and love. I would also like to thank my parents, Susan and Patrick for their continual support through hard times and good times. And thank you my brother, Erik, I have gained much from your wisdom. Someday may I repay you all, for I am truly in your debt.

I would like to thank my advisor, Brady, for keeping me on track. You have given me excellent guidance, and taught me to use my wits as well as my instinct in the pursuit of science. He has imparted upon me tons of practical knowledge, since so much of the lab is based on custom built apparatus. He encouraged experimentation and a hands-on ideals of science from day 1. Thank you.

I would like to thank my lab mates for teaching me the ropes. Thanks Yu Hong, and Kirsten, Noon, and Bryan. Thanks to my current lab mates Jose and Ashley, Austin, Maddie, Shidong and Kyle. We've had good times and good conversations. Keep the science party going.

Thanks also to everyone in the Materials Science Department. Thanks Bill Warnes and Dave Cann especially, who were great teachers and whose contributions and advice were invaluable to my research. And to all the staff in the MIME Graduate Office for their cheerful help, Phyllis and Jean, Emma and Matthew. We appreciate it! And I have to thank the Cann group, especially Nitish and Troy for their help with my projects. And to all the others, there are far too many to list, but you better know I love you guys.

CONTRIBUTION OF AUTHORS

As my PhD advisor and principal investigator, Prof. Brady J. Gibbons has contributed to all the work shown in this thesis.

TABLE OF CONTENTS

TABLE OF CONTENTS (Continued)

Page

TABLE OF CONTENTS (Continued)

Page

LIST OF FIGURES

Figure Page

LIST OF FIGURES (Continued)

Figure Page

LIST OF FIGURES (Continued)

Figure Page

LIST OF TABLES

1. Introduction

1.1 Motivation

Solid solutions based on the ferroelectric perovskite $Bi_{0.5}Na_{0.5}TiO_3$ (BNT) and $Bi_{0.5}K_{0.5}TiO_3$ (BKT) might someday replace current Pb-based ferroelectric and piezoelectric devices. The goal of this research was to advance the understanding of long term reliability in polycrystalline BNT-BKT-based thin films fabricated by chemical solution deposition (CSD). The driving force to develop these materials is the Restrictions on Hazardous Substances (RoHS), which seeks to limit Pb in consumer devices [1]. Despite repeated extensions of exemptions for Pb-based ferroelectrics, there is still no material to date which can fully replace Pb-based materials. BNT-BKT-based compounds are a potential alternative for some transducer applications due to a combination of having a depolarization temperature (T_d) ≈150 °C, good piezoelectric properties, and low leakage currents relative to other Bi, Na and K-based ferroelectrics. In order to realize the widest range of applications, BNT-BKT-based materials must be optimized through the use of ternary systems and dopants, as has been done for Pb-based materials. This will have implications for the long term reliability of devices.

It is very common that devices with ac driving sources are operated with an applied dc bias [2]. Large leakage currents can adversely affect device efficiency and reliability. Analysis of leakage current can also give clues towards improving materials and/or processing conditions. The constituent cations; Bi, Na, and K are all highly volatile at the crystallization temperatures employed, and oxygen vacancies are common to all oxide perovskites. The resulting defects can directly be associated with higher leakage currents, which can reduce long term stability by increasing the frequency of early failures due to localized electric-field breakdown events. Mobile defects are also implicated in resistance degradation and cycling fatigue. The importance of studying dc leakage current in ferroelectric and piezoelectric thin films is clear.

Our understanding of the relevant parameters necessary to characterize the robustness of these materials has not developed nearly as completely as, for example, $BaTiO_3$ and Pb-based materials. This is particularly so in the case of leakage current in thin films. These characteristics have implications for both performance and long term stability. Therefore, this thesis is devoted to a study of conduction processes at both short and long time scales, and at elevated temperatures. All of these factors are important for contemporary devices. For instance, dielectric relaxation currents are a function of both temperature and time. Accounting for dielectric relaxation is necessary for a true measurement of the steady state leakage current. Transient currents at high temperatures and on long time scales, encountered in Chapters 4 and 5, can imply ionic migration which is known to have significant implications for reliability. Ionic migration can affect such phenomena as fatigue, resistance degradation, and ferroelectric polarization suppression. A form of positive temperature coefficient of resistivity (PTCR) was observed in many samples, and discussed in Chapters 4 and 7.

This work is designed to convey the rich diversity of conduction behaviors in BNT-based thin films, and possibly to provide guidance how to mitigate them in order to hasten their adoption.

1.2 Objectives

The overarching scientific goal of this work is to illuminate the factors that differentiate the conduction properties of different compositions, so that the underlying reasons for these differences may be understood and capitalized upon. The specific objectives of this research are as follows:

i. To conduct a systematic study of Mn-doping in 80BNT-20BKT thin films. Mn is commonly added to decrease the leakage current in many ferroelectric thin films. It is studied here in detail, comparing different concentrations of Mn, and observing the leakage current as a function of temperature.

ii. To explore the steady state, dc leakage current versus electric field and temperature in BNT-based thin films. To model the results and determine the conduction mechanism(s). The variation of leakage current with x in the binary (100-x)BNT-

*x*BKT system is explored, as even this seemingly basic information is not currently available in the literature. The effect of the partial pressure of oxygen (pO_2) during annealing is also explored. This experiment can help to identify the carrier type of a film. Also, a post-anneal step under various pO_2 is commonly added to improve the stability of capacitors. This will provide a good reference for the optimization of this procedure.

iii. To measure the transient currents in BNT-based thin films. To study the cause of these currents and their relationship to other film properties. The currents are thought to be related to ionic migration. The migration of ions under applied electric field has been implicated in electric-field fatigue, resistance degradation, and polarization suppression in perovskite ferroelectrics. It is desirable to understand the conditions under which ionic migration occurs so that effort can be directed at preventing it.

References

[1] J. Rödel, W. Jo, K. T. P. Seifert, E. M. Anton, T. Granzow, and D. Damjanovic, "Perspective on the development of lead-free piezoceramics," *J. Am. Ceram. Soc.*, vol. 92, no. 6, pp. 1153–1177, 2009.

[2] G. W. Dietz, W. Antpöhler, M. Klee, and R. Waser, "Electrode influence on the charge transport through $SrTiO_3$ thin films," *J. Appl. Phys.*, vol. 78, no. 10, pp. 6113–6121, 1995.

2. Background and literature review

2.1 Review of ferroelectric thin films

2.1.1 Perovskite crystal structure

The entire range of solid solutions (100-*x*)BNT-*x*BKT crystallize into the perovskite structure. The unit cell is shown in Fig. 1. The ideal perovskite structure, with the formula ABO_3, is a simple cubic lattice with space group $Pm\bar{3}m$. The A-site lies on the corners of the unit cell, the B-site cation lies at the center, and oxygen anions sit on the face centers.

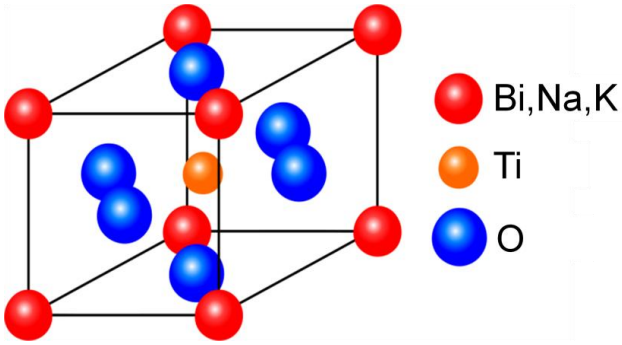

Figure 2.1 – *The perovskite crystal cell, of which BNT and BKT are examples.*

The structure often undergoes slight deviations from its cubic form, becoming either tetragonal or rhombohedral. The Goldschmidt criterion can be used to roughly predict the distortion of the perovskite structure given the ionic radii of the constituent atoms by defining the tolerance factor, t, as [1]

$$t_G = \frac{r_A + r_O}{\sqrt{2}(r_B + r_O)}. \qquad (2.1)$$

For the perovskite ABO_3 to form, generally $0.9>t_G>1.1$. Cubic systems are predicted for $t_G \approx 1$. When $t_G>1$, a polar distortion develops, indicating that the B atom resting in the octahedron is small and the crystal will have a tetragonal distortion. Conversely, when the A atom is small, the distortion will more likely be to the rhombohedral or orthorhombic structure.

2.1.2 Polarization mechanisms

Polarization, *P*, is defined as the separation of electric charge. There are many physical examples including, among others, space charge, ionic, and electronic

polarization. Each of these responds with deformation when placed in an external electric field, *E*. There is also a characteristic frequency associated with each unique source, above which *E* is changing too fast for the source to respond. This is illustrated in Fig. 2.2.

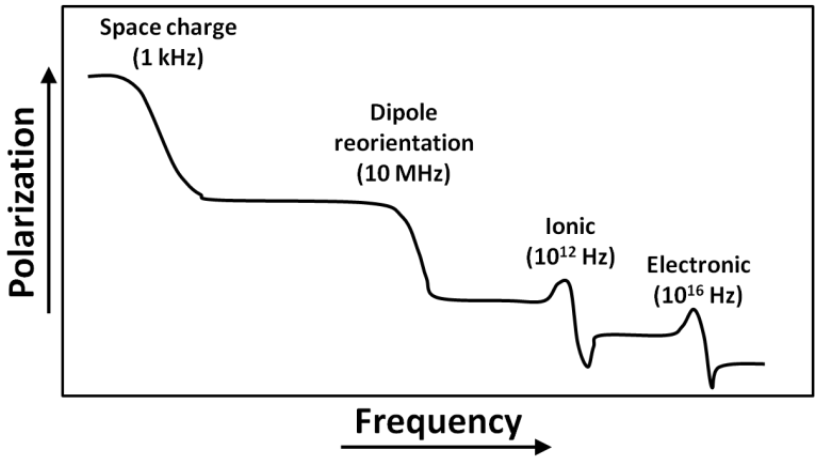

Figure 2.2 – *Frequency dependence of some common polarization mechanisms.*

Dielectric media experience an electric polarization throughout the bulk made up of microscopic electric dipole moments. All dielectrics exhibit some kind of polarization response to an applied electric field, but usually it is linear to a first order approximation. Ferroelectric crystals, on the other hand, are made up of spontaneously polarized regions called domains. Ferroelectrics exhibit a complicated non-linear, hysteretic response to an applied electric field, due largely to this domain structure, and so they are termed non-linear dielectrics.

2.1.3 Dielectrics

The parallel plate capacitor is illustrated in Fig. 2.3. A linear dielectric material, which could be in the form of a thin film, is subjected to *E* placed across two electrodes and develops a uniform *P* normal to the surface. The net effect of the polarization is a bound charge on the surface of the dielectric. In perovskite dielectrics it is the oscillation of the smaller B-site atoms relative to the oxygen octahedra that is the primary contributor to the ionic polarization. These ionic displacements are able to respond to *E* below several GHz.

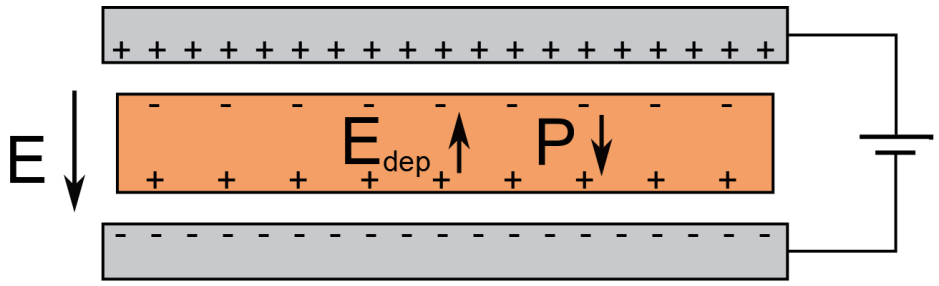

Figure 2.3 – *Parallel plate capacitor.*

The law of proportionality between P and E is

$$P = \chi_e \varepsilon_0 E, \qquad (2.2)$$

where χ_e is the relative dielectric susceptibility, and ε_0 is the permittivity of free space [2]. The dielectric permittivity, ε, is also defined in terms of the χ_e. Thus the permittivity and susceptibility are equivalent concepts and they are related to each other and to the polarization of the material through

$$\varepsilon = \varepsilon_0(1 + \chi_e). \qquad (2.3)$$

The relative permittivity, ε_r, is given by

$$\varepsilon_r = \frac{\varepsilon}{\varepsilon_0}. \qquad (2.4)$$

Real capacitors, which are imperfect insulators, have energy losses associated with them due to dielectric relaxation, as well as electronic conduction. This can be seen when the permittivity is expressed as a complex number:

$$\varepsilon^*(\omega) = \varepsilon'(\omega) + i\varepsilon''(\omega), \qquad (2.5)$$

where $\varepsilon^{'}$ is the lossless permittivity and $\varepsilon^{''}$ is the lossy permittivity due to the energy dissipated. In the case of good insulators, when electronic conduction is minimal, the fraction of energy dissipated versus that stored by the capacitor is known as the loss tangent.

$$\tan\delta = \frac{\varepsilon''}{\varepsilon'}. \qquad (2.6)$$

In perovskite ferroelectrics, the presence of space charge due to defects such as vacancies can result in losses in the region 0.1-10 kHz. Therefore, one sign of the quality

(with small numbers of defects) of a dielectric film is a small tanδ at 1 kHz, at least below 5 %.

2.1.4 Piezoelectricity

The term piezoelectricity is derived from the Greek word "piezo", which means "to press", and "electricity". The phenomenon was discovered by Jacques and Pierre Curie in 1880 [3]. Via the direct effect, piezoelectric materials generate a dielectric displacement under applied stress. The indirect effect is described as a strain, S_{jk}, induced by an externally applied E_i [4].

$$S_{jk} = d_{ijk}E_i \tag{2.7}$$

In Eq. (2.7), d_{ijk} is the piezoelectric coefficient which described the rate of strain under a *E*-field in the *i*-th direction. The subscripts can be compressed to from three components down to two, due to symmetry about two non-polarized axes. One commonly reported piezoelectric coefficient for piezoceramics fabricated in the parallel plate capacitor structure is d_{33}, which describes the mechanical strain in the same direction as the applied field. Piezoelectricity is seen only in crystals with point groups which lack a center of symmetry. The breaking of the center of symmetry is essential to maintaining the long range order responsible for the piezoelectric effect.

2.1.5 Ferroelectricity

The anomalous dielectric properties of what are known as ferroelectrics have been investigated since the discovery of piezoelectricity in Rochelle salt in 1880 by the brothers Curie [3]. The first known perovskite, $CaTiO_3$, is a mineral discovered in the late 1800's. Barium titanate ($BaTiO_3$, BTO), was investigated around 1940 by Wainer and Salomon at the National Lead Company [5]. Research into solid solutions of $Pb(Zr,Ti)O_3$ (PZT) began in earnest in the 1950s, soon finding use in many common products including sonar, ultrasound, actuators, and speakers.

Typical dielectrics exhibit a linear polarization in response to an applied electric field. Ferroelectric crystals, on the other hand, are made up of spontaneously polarized regions called domains. Ferroelectrics exhibit a non-linear, hysteretic response to an applied electric field, which can be explained in terms of this domain structure.

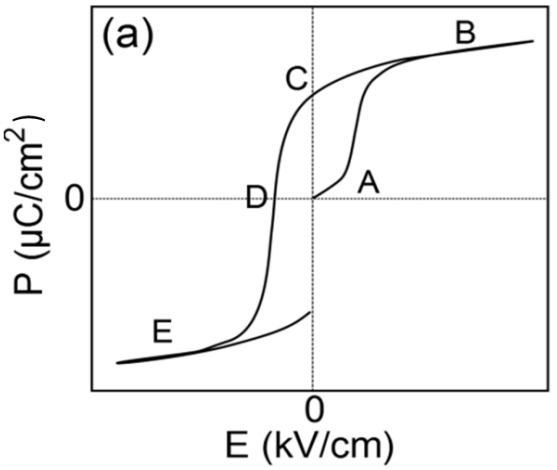

Figure 2.4 – *A typical ferroelectric hysteresis loop.*

Take, for example, the hysteresis loop in Fig. 2.4. Before the field is applied, the sample is assumed to be unpoled (without any polarization present). As the field is initially applied, the polarization is approximately linear, according to the proportionality $\chi_e \varepsilon_0$. At point **A**, the domains begin to rapidly align with the direction of E, and slope of P increases. Eventually there is saturation at some maximum polarization, P_{max}, at point **B**. As the applied field begins to sweep in the reverse direction, some of the domains reverse due to a depolarizing field until E=0, at point **C**, where what remains is some remanent polarization, P_r. The sweep continues in the reverse direction until P=0, at point **D**, where the coercive field, E_c is reached. Continuing the loop results in saturation in the opposite direction, point **E**, and the hysteresis continues, repeating the path.

2.1.6 Phase transitions

Ferroelectricity refers to the collective behavior driving the alignment of the dipoles. In order to reduce the free energy of the crystal the lattice, the dipoles reorient and the crystal becomes divided into smaller regions called domains. The equilibrium size of domains are governed by two competing factors. On the one hand there is a cascade effect whereby the strain of the lattice at a domain boundary induces a dipole in the next site. On the other hand, surface charges from very large domains would form a large depolarization field which would cause some parts of the domains to reorient to minimize the Coulombic force. In the simplest case, domains may become twinned into adjacent domains of opposite polarity. These 180° domain boundaries have a very low energy because the lattice distortion is the same and only the direction of the polarization

is different. It is the motion of domain boundaries which leads to the hysteresis of the response to stress or electric field.

The spontaneous polarization, P_s, is defined as the lattice polarization which minimizes the Gibbs free energy of a crystal. A phase transition can be defined in terms of Landau-Devonshire-Ginzburg (LDG) theory to be of first or second-order. The LGD formalism successfully describes the Curie-Weiss behavior of the permittivity, the hysteresis of polarization vs. electric field and predicts the appearance of ferroelectric domains [6]. At the Curie temperature, T_C, a normal ferroelectric has a maximum in ε_r, while P_s approaches zero [7].

A related class of materials are the relaxor ferroelectrics, the group to which the BNT-BKT solid solutions belong. Rather than being divided into large coherent domains, relaxors are composed of polar nanoregions (PNRs), as fabricated. Relaxors may be thought of as having an ensemble of nano-sized domains with a distribution of T_C. Therefore, relaxors have a non-zero P_s and a broad maximum in ε_r, which also has a strong frequency dispersion.

Many perovskite solid solutions exhibit relaxor behavior over some range of temperatures where the A-site or B-site disorder frustrates the long range order. In the case of BNT-BKT, this is attributed to the disorder caused by A-site mixing between Bi, Na and K. As the temperature is reduced from the high-T cubic phase, PNRs begin to form at the Burns temperature, T_B, indicating the beginning of the ergodic relaxor state [8]. An ergodic relaxor material can be prodded into a ferroelectric state when subjected to a sufficiently strong electric field. The ferroelectric state is metastable and will persist for some amount of time until it is de-poled via thermalization. As the temperature is cooled some PNRs grow and their polarizations become fixed, ceasing the thermally induced fluctuation. As the temperature is cooled below the depolarization temperature, T_d, all of the polarizations are fixed and the crystal enters the nonergodic state. Application of a poling field can transform the nonergodic state to a ferroelectric state composed of domains.

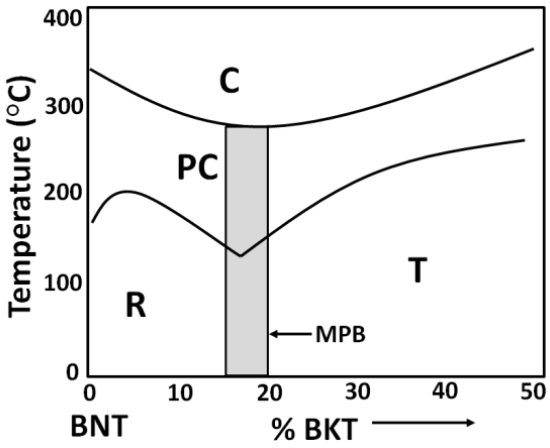

Figure 2.5 – *Approximate phase diagram for (100-x)BNT-xBKT. 'R' and 'T' denote rhombohedral and tetragonal phases, 'PC' denotes the pseudocubic, and 'C' the cubic region. Phase diagram based on that of Leontsev and Eitel* [9].

The phase diagram showing the phase diagram for (100-*x*)BNT-*x*BKT can be seen in Fig. 2.5. At low temperature they are normal ferroelectrics or non-ergodic relaxors depending on kinetics. The material undergoes a polymorphic phase transition (PPT) to an ergodic relaxor state when heated above T_d in the pseudo-cubic region, and become a simple cubic lattice at high temperatures. The shaded region of Fig. 2.5 shows the region of the morphotropic phase boundary (MPB) region, where the combination of rhombohedral and tetragonal phases leads to an increased number of polarization directions, and the presence of lower symmetry (e.g. monoclinic) phases can lead to a lowering of the energy barrier for polarization rotation [10]. This leads to an increase in the polarization and piezoelectric response of materials with compositions in the MPB region.

2.1.7 Thin film considerations

There are many ways in which the ferroelectric thin films differ from bulk materials. Partly this is due to the large surface are of films which result in volatilization of cations and increased defect densities. The large extrinsic polarizations exhibited by ferroelectrics are due to the motion of domain walls whose motion can be impeded by defects which act as pinning sites [11][12].

The electromechanical switching properties are also affected by the substrate clamping effect. The mechanical rigidity of the substrate impedes the strain response as

the film attempts to actuate. In this case, it is more appropriate to think about an effective piezoelectric coefficient, $d_{jk,f}$ (e.g. $d_{33,f}$). There are many excellent demonstrations of the clamping effect. For instance, It was been shown that the extrinsic polarization response of a released film by under-etching is greatly increased [13]. In another study, ferroelectric thin films 'islands' patterned by focused ion beam showed increased piezoelectric properties measured by piezoresponse force microscopy [14].

2.2 Leakage current

Although significant effort has been made towards improving the piezoelectric and polarization properties of Pb-free thin films, it is also important to improve the efficiency and longevity of these materials. If a material has excellent piezoelectric properties, but has poor resistivity and degrades quickly, then its widespread applicability is questionable. Below is a quote which explains well the situation.

"Most researchers put efforts on improving the piezoelectric performance from the 'real part' property's viewpoint: that is, improved displacement, force, responsivity, etc. . . . However, from the viewpoint of efficiency and reliability such as heat generation or performance degradation under high voltage/power drive, the key is the imaginary part, that is, loss and hysteresis mechanisms" (Uchino, *Applications of Lead-Free Piezoelectrics*, 2011) [15].

The leakage current in BNT-based thin films is still several orders of magnitude greater than that of PZT [16][17]. There is still considerable room for improvement, but there are many unknown variables given the relative novelty of the films based on Bi, Na, and K cations. The nature of charge carriers and defects, the competition between bulk and interface-dominated conduction, and the effect of processing are all in their infant stages relative to PZT research. It is expected that many of the fundamental experiments conducted on PZT in the 1980's and 1990's will need to be repeated on Pb-free thin films. While thousands of papers have been published detailing the leakage current observed in PZT thin films, only a handful have appeared dedicated to conduction in Pb-free thin films.

2.2.1 Measurement of leakage current

Leakage current density, J, is the electric current per unit area which 'leaks' through an imperfect insulator when E is applied at temperature, T. When speaking of the J it is important to understand that this value may change with time. There are several regimes in the J-t plot which are of interest to the experimentalist, as shown in Fig. 2.6. Initially there are dielectric relaxation currents due to space charge trapping and redistribution. Then there are the steady state J, which in an ideal case may be modeled as $J(E,T)$ to find the mechanism of electronic conduction. The onset of the steady state current may be preceded or succeeded by some transient currents, if there are any. Eventually, the sample will reach dielectric breakdown and failure. Depending on the sample and applied E, this can occur in milliseconds, days, or even longer. Due to the asymmetric nature of thin film fabrication, leakage characteristics are often different depending on whether E is positive or negative (E^+ or E^-) with respect to the deposition direction and method.

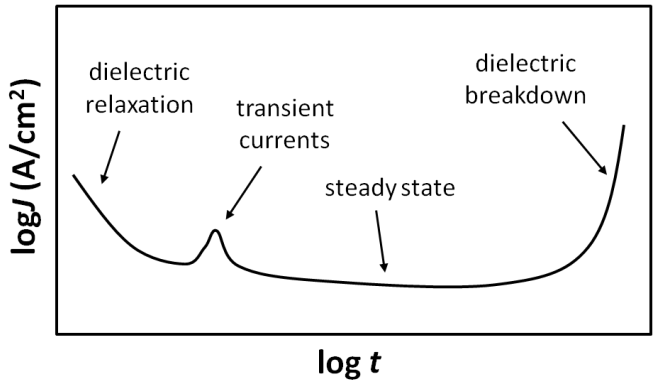

Figure 2.6 – *A schematic of a logJ-logt plot may show several distinct features over the time span of the measurement.*

2.2.2 Relaxation current and the steady state

Initially, the dielectric relaxation current is a decreasing function of time, $J_D(t)$, which is superimposed upon the steady state leakage current, which is defined when

$$\frac{\partial J}{\partial t} = 0, \qquad (2.13)$$

which can be met in anywhere from milliseconds to many minutes depending on the charge voltage, temperature, and carrier mobility. Whether such a condition may be met during the course of experiments depends on the limitations of the instrumentation as

well as the onset of resistance degradation. For instance, if there is a time limitation on the length of a leakage current measurement, steady state might not be reached. In some cases the dielectric relaxation and resistance degradation can overlap. In order to find the true leakage current, it may be necessary to measure the discharging current of the capacitor, found by charging the capacitor and then removing the field and measuring $J(t)$ [18]. In the case, when the steady state could not be reached, the steady state leakage current, J_{SS} may still be calculated from the known depolarization current as

$$J_{SS} = J(t) - |J_D(t)| \tag{2.14}$$

The function $J_D(t)$ should be measured at many voltages as the relaxation current is naturally field dependent.

2.2.3 Steady state leakage current mechanisms

For injection of either n-type or p-type carriers at either electrode, the current can be limited by either a potential barrier at the film interface or by space charge effects inside the volume. Often, a metal-ferroelectric interface has a Schottky barrier. For instance, given an insulator with majority n-type carriers, a Schottky contact will form when the metal work function is larger than the insulator work function.

$$\phi_M > \chi + E_C - E_F = \phi_I \tag{2.14a}$$

$$\phi_B = \phi_M - \chi \tag{2.14b}$$

In Eq. (2.14a), ϕ_M is the metal work function, ϕ_I is the insulator work function for electrons, and χ is the electron affinity of the insulator. The Schottky barrier height at E=0, ϕ_B, is given by Eq. (2.14b). The barrier physically arises from an equilibrium separation of charge at the interface, and the barrier is lowered by an amount proportional to the $\sqrt{E}$ [19]. The equation governing Schottky-limited leakage current in ferroelectric thin films is

$$J = \alpha T^{3/2} E \mu \left(\frac{m^*}{m_0}\right)^{3/2} \exp\left[\frac{-q\left(\phi_B - \sqrt{qE/4\pi\varepsilon_i\varepsilon_0}\right)}{k_B T}\right], \tag{2.15}$$

where the pre-exponent contains the constant α=3x10^{-4} As/cm^{3}K$^{3/2}$, the electron mobility, μ, and the free and effective electron masses, m_0 and m^*, respectively. In the exponent, q is the electric charge, k_B is Boltzmann's constant, and ε_i is the optical dielectric

constant [20][21]. A plot of $\ln(J/T^{3/2}E)$ versus $E^{1/2}$ should be a linear function of $1/T$. A valid Schottky model fit to a particular data set should provide realistic values for ε_i and ϕ_B as determined by analysis of the slope and intercept method.

In the case where the Fermi level has been moved very close to the conduction band or valence band, or when the work function of the metal is low, the metal and insulator may make a non-blocking Ohmic contact. For Ohmic contacts there is essentially no barrier to charge injection and the effects become bulk-limited. The ideal space-charge-limited current (SCLC) model may have several features described by the following equations, which will be discussed [22].

$$J_{Ohm} = qn_0\mu E \tag{2.16a}$$

$$J_{TFL} = \frac{9}{8}\mu\varepsilon\frac{1}{d}N_C G E^2 \exp\left(\frac{E_t - E_c}{k_B T}\right) \tag{2.16b}$$

$$J_{Ch} = \frac{9}{8}\mu\varepsilon\frac{1}{d}E^2 \tag{2.16c}$$

Initially, the *J-E* relationship is linear, governed by Eq. (2.16a) where q is the elementary charge constant, n_0 is the number of charge carriers, and μ is the charge carrier mobility. Other variables keep their previously assigned definitions. Subsequently, the current goes through a traps-filling-limited region, described by Eq. (2.16b), although this is often difficult to resolve. Here, k_B is Boltzmann's constant, ε is the dielectric constant, d the film thickness, N_C is the number of carriers, G is a constant, and E_t–E_c describes the difference between the traps-filled and conduction band energy levels. The current jumps immediately after the traps are filled as the film becomes limited only by the space charge, and the Child's law region of Eq. (2.16c) is observed (if the sample has not reached the breakdown field), where d is the film thickness. The sequence is illustrated in Fig. 2.7. The deviation from Ohmic current occurs at E_{tr}. J_{Ch} begins at E_{TFL}, after any traps have been filled.

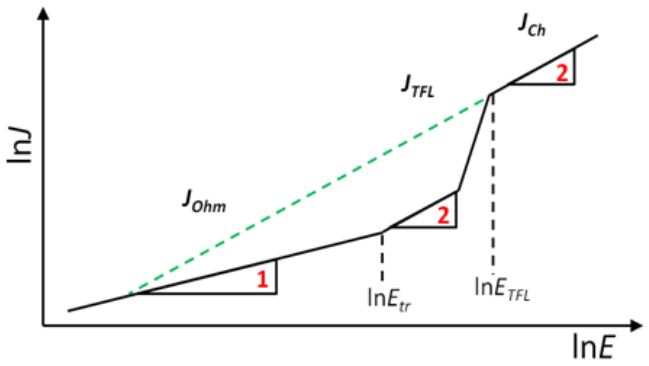

Figure 2.7 – *Schematic of the lnJ-lnE characteristics of data fitting the SCLC model. The numbers in the drawn triangles are the slopes of the lines which they contact.*

Other bulk limited models to consider include Poole-Frenkel (P-F), hopping conduction and Fowler-Nordheim (F-N) tunneling [22]. The basis for verification or exclusion of these mechanisms largely parallels the above discussion of Schottky and SCLC models.

2.2.4 Transient currents and $V_O^{\cdot\cdot}$ migration

A peak in the dc current density-time (*J-t*) plots were first suggested to be related to diffusion of oxygen vacancies, $V_O^{\cdot\cdot}$, by Zafar, *et al*, who studied Ba(Sr,Ti)O_3 thin films [23]. The peak position is given by

$$\tau = \frac{7.8\text{x}10^{-4}d}{\mu_{ion}E}, \qquad (2.17)$$

where μ_{ion} is the ionic mobility, d is the film thickness in units of cm, and E has units of kV/cm. The Einstein equation,

$$k_B T\mu_{ion} = qD_{ion} = q\gamma \exp\left(-\frac{E_{A,ion}}{k_B T}\right), \qquad (2.18)$$

relates μ_{ion} to the thermally activated diffusion coefficient, D_{ion}. γ is a constant which can be interpreted as the diffusion coefficient at infinite temperature. The activation energy for ion migration, $E_{A,ion}$, can then be obtained by an Arrhenius plot.

The subject was revisited and a simulation was developed based on a finite differences method was used to calculate the densities of electrons, holes, and oxygen vacancies by diffusion and drift [24]. The transient peak was revealed to be due to a modulation of the electronic conductivity due to redistribution of $V_O^{\cdot\cdot}$. The electron

mobility is many orders of magnitude higher than the μ_{ion}, so it is thought that a true ionic current could not account for the observed current peak. The technique has been in several instances to characterize $V_O^{\bullet\bullet}$ migration in dielectric thin films [25][26].

2.3 $(Bi,Na)TiO_3$-based solid solutions

2.3.1 Piezoelectric properties

The large signal d_{33}, d_{33}^*, for bulk BNT-BKT and BNT-BKT-BT in the MPB region are around 240 and 270 pm/V, respectively [27]. However, ternary compositions of BNT-BKT-KNN ceramics have reached very high d_{33}^* near 570 pm/V, at the cost of reduced T_d. Recently, BNT-BKT-BMgT and BNT-BKT-BNiT ceramics were fabricated with very high piezoelectric coefficients, around 570 pm/V and 520 pm/V, respectively [28][29][30]. Due to the relative scarcity of DBLI measurement capabilities, there are very few reports on the $d_{33,f}$ for Pb-free thin films in general. As it pertains to Bi, Na, and K-based films there may be only a single report from Jeon, *et al.*, who published strain loops on BNT-BKT-$Bi(Mg,Ti)O_3$ and found $d_{33,f} \approx 75$ pm/V [31].

The non-vertical MPB line can result in unreasonably large variations in piezoelectric properties with temperature. Often, it is seen that T_d is depressed while the same time the piezoelectric coefficient is increased, on addition of a ternary end member [32][27]. For some applications search for systems with more vertical MPB's and higher T_d almost as important as the search for higher piezoelectric coefficients. For other applications, the binary systems may be augmented with ternary end members which may improve the room temperature coefficients.

2.3.2 Defects in BNT-based thin films

There are many types of electronic point defects which can be created when the film is heated to the crystallization temperature. Volatilization of cations Bi, Na and K can create compensating oxygen vacancies, in an attempt to maintain charge neutrality, as in the vaporization of bismuth oxide. Eqs. 2.19-20 show what happens when oxygen

leaves the lattice site as gas after diffusing to the surface. The vacancy then oxidizes, forming two n-type charges.

$$O_O \rightarrow 1/2O_2 + V_O^x \quad (2.19)$$

$$V_O^x \rightarrow V_O^{\cdot\cdot} + 2e^/ \quad (2.20)$$

Bi, Na and K can also leave the film as Bi_2O_3, Na_2O, or K_2O, creating both holes and electrons. For example, Bi leaves by the reaction

$$2Bi + 3O \rightarrow 2V_{Bi}^X + 3V_O^X + Bi_2O_3(g), \quad (2.21)$$

which is followed by reduction and oxidation of the vacancies as in

$$2V_{Bi}^X + 3V_O^X \rightarrow 2V_{Bi}^{///} + 3V_O^{\cdot\cdot} + 6h^{\cdot} + 6e^/. \quad (2.22)$$

There is also a pO_2 dependence to the number of charge carriers and traps in the film. Free oxygen may recombine with vacancies via Eq. (2.23), with the consequence being additional positive electron-holes, or *p*-type carriers. Or oxygen may exit the lattice on its own leaving behind electrons, or *n*-type carriers. This is shown in Eq. (2.24), which represents an oxygen leaving a vacancy and migrating to the surface to eventually react with another adsorbed oxygen, while the vacancy doubly ionizes.

$$V_O^{\cdot\cdot} + 1/2O_2 \rightarrow O_O^x + 2h^{\cdot} \quad (2.23)$$

$$O_O \rightarrow V_O^{\cdot\cdot} + 2e^/ + 1/2O_2(g) \quad (2.24)$$

Many dopants, both acceptor and donor, have been added to ferroelectric ceramics, for many reasons. One of the most popular dopants is Mn, which tends to increase the resistivity in many different compositions in both ceramic and thin film form. Mn-doping has been shown to mostly dope for Ti on the B-site with a +2 or +3 charge, and so can result in several kinds of point defects.

$$2Mn^{3+} \rightarrow 2Mn_{Ti}^/ + V_O^{\cdot\cdot} \quad (2.25)$$

$$Mn^{2+} \rightarrow Mn_{Ti}^/ + V_O^{\cdot\cdot} \quad (2.26)$$

There are also interstitial sites, dislocations, and also chemical terminations and voids at grain boundaries which can provide conditions to trap charged and uncharged species. Thus grain size, residual stress and other morphological and mechanical factors can mediate the formation and residence of defects.

2.3.3 Leakage current in Pb-free ferroelectrics

It may be helpful to summarize the published leakage current results for BNT, $(K,Na)NbO_3$ (KNN) and $BiFeO_3$ (BFO)-based thin films and compare them to the more well established $Ba(Sr,Ti)O_3$ (BST) thin films. All of these materials share some volatile A-site cations (Bi and/or Na and K). However, BST thin films are a more mature technology with different, and less volatile, A-site cations. The properties of these solid solutions will be briefly discussed beginning with BNT-based films.

Cao, *et al*. have measured the band gap of BNT thin films and found it to be around 3.5 eV, although due to the strong Urbach absorption, the results required some approximations [33]. The sign of the dominant charge carriers is not known definitively. BNT-based films typically make Ohmic contacts to Pt, however there are still many things which are not understood, such as the depletion width and the presence or absence of a charge inversion. Despite a decade of research there are only a couple reports on the conduction properties of BNT-based thin films, however there are quite a few more, which show at least some isolated leakage data which could potentially be aggregated to some use. For convenience, the abbreviation FE will be used to represent the ferroelectric layer in the capacitor structure.

Films of 88BNT-8BKT-4BT were deposited by PLD (Au/FE/SRO/STO) and leakage current was measured out to only 250 kV/cm at relatively low temperatures (200 to 350 K) [17]. Almost perfect adherence to the SCLC conduction mechanism was found for positive bias and a variety of useful parameters were obtained, e.g. electron mobility of 5.82×10^{-3} $cm^2V^{-1}s^{-1}$ and shallow trap levels of 0.19 eV. The temperature dependence of conductivity in BNT thin films deposited by rf-magnetron sputtering (FE/Pt/Ti/SiO_2/Si, top electrodes not reported) was studied by Zhou, *et al*. [34]. The ac conductivity was measured at 100 kV/cm from room temperature to 523 K. At low temperatures they also report shallow traps with activation energy around 0.08 eV. Above 473 K they found a transition to grain boundary conduction limited by hopping over oxygen vacancies, having an associated activation energy near 1 eV. This was not the only reference to grain boundary conduction. An increase in the room temperature leakage current in chemical solution deposited deposited BNT-BKT-6BT thin films doped with >5 mol% Rb (Au/FE/Pt/Ti/SiO_2/Si) was also correlated to the grain boundary

density, although the doping of the grain boundaries may have changed as well as the area [35].

Films of 95(80BNT-20BKT)-5STO doped with {0, 0.2, 0.5, 1} mol% Mn were made by CSD (Au/FE/Pt/Ti/SiO_2/Si) [36]. For fields < 125 kV/cm, Ohmic current was found in all films which increased in magnitude with Mn-doping. A transition voltage was identified, marking a rapid increase in current, which increased for 0.2 and 0.5 mol% Mn. At those doping levels the current remained Ohmic almost until 400 kV/cm. At high field the mechanism appears to be SCLC, though this could not be known positively without a study at temperature. Room temperature leakage current was also reported for 76BNT-20BKT-4BLT films deposited by PLD and doped with 2 mol% Mn (Au/FE/SRO/STO) [37]. The leakage current showed some complicated features, which will be discussed later, but the Mn-doping did result in a decrease in the leakage current out to 400 kV/cm.

Next, the KNN-based films will be discussed. The number of detailed reports on leakage current through KNN-based films is greater than that for BNT-based films, although still it is hard to find reports on the leakage current above 150 kV/cm.

For KNN thin films the cation excesses used are typically 10-15 mol% Na and K when deposited by CSD but using a stoichiometric target when depositing by PLD. Leakage testing of the films was often restricted to electric fields <150 kV/cm [38][39][40]. This was the case for both Au and Pt top electrodes and for films deposited on SRO/STO and Pt/Ti/SiO_2/Si. Most times the leakage current was asymmetric, even for the case with both Pt top and bottom electrodes. This is likely due to an asymmetry of the defect distribution. Tian, *et al*., later made films via PLD, also from a stoichiometric target, which withstood fields >400 kV/cm and showed clear SCLC in several of samples deposited at various temperatures [41]. Mn-doping has shown to be effective at reducing leakage current in KNN-LT-LS [42]. Mn-doping have the similar effect as BNT-based films whereby the E_{tr} is increased which decreases the high field leakage while leakage current rises in the Ohmic region.

The leakage current of BFO films is covered here. BFO films are often leaky ferroelectrics, and most reports appear to be described by Ohmic contacts with SCLC. Doping with La and Mg has been attempted in order to reduce leakage currents in BFO

thin films, but determination of the conduction mechanism was extremely complicated. Wang, *et al*., reported on changing the conduction mechanism from P-F for undoped and Mg-doped BFO while the La-doped samples showed SCLC [43]. Work several years later determined interfacial F-N tunneling dominated leakage in Mg and La-doped films, while co-doping obeyed SCLC [44]. However, it seems the SCLC mechanism cannot be ruled out for any of these films since often the Child's law region is not reached before breakdown. Furthermore, non-uniformity of space charge through the film thickness may complicate SCLC identification. Others have had difficulty positively identifying a conduction mechanism as well, even for undoped films [45]. Common suspects are P-F, Schottky and SCLC.

The Mn-doping approach was also successful in BFO. In these studies SCLC was identified as the mechanism with Mn-doping having similar effects in the Ohmic and transition regions as in BNT-based and KNN-based films [46][47]. However, a study on very thin films (5-70 nm) found excellent fits for F-N tunneling. The samples in this study were taken up to 3000 kV/cm for the 5 nm thick film.

The last material which will be discussed here is BST. BST has been studied extensively and is a prototype for leakage current and defect studies. The band gap is similar to PZT, around 3.5 eV. The conduction is usually identified as Schottky-limited [19][48]. However, there have been reports of mixed Schottky and P-F at high fields [49]. Schottky barrier height can be reduced by increase in the image force due to an increase oxygen vacancies near the surface [50]. In another report, SCLC was observed for positive bias applied on the Au top electrode [51]. Much of the debate in the literature on BST leakage has had to do with the nature of the depletion region. Some have argued for a small region at the surface, where oxygen vacancies are thought to be depleted due to the electric field created at the Schottky contact [48]. However, others have suggested that the film is fully depleted [19]. It is may be that the depletion region might vary depending on both the voltage and temperature [24][49].

Space charge tends to dominate the leakage current characteristics for ferroelectric thin films containing volatile Bi, Na and K cations. The Child's law region is often not reached before breakdown and often the transition region and the temperature dependence of its onset is the only indication of the SCLC mechanism. In the case of

BFO films, which do not contain Na and K cations, possible P-F, Schottky and maybe even F-N tunneling have been observed. With BST, the A-site cations are less volatile than Na and K, and the technology and fabrication processes are better understood. The net result is a decrease in the space charge density and thus reported leakage current is often dominated by the Schottky mechanism.

References

[1] V. M. Goldschmidt, "Die gesetze der krystallochemie," *Naturwissenschaften*, vol. 14, no. 21, p. 477, 1926.

[2] A. J. Moulson and J. M. Herbert, *Electroceramics: materials, properties, applications*. 2003.

[3] J. Curie and P. Curie, "Development by pressure of polar electricity of hemihedral crystals with inclined faces," *Bull. la Soc. Mineral. Fr.*, vol. 3, pp. 90–102, 1880.

[4] B. Jaffe, W. R. Cook, and H. Jaffe, *Piezoelectric ceramics*. London: Academic Press, 1971.

[5] L. E. Cross and R. E. Newnham, "History of Ferroelectrics," *Ceram. Civiliz.*, vol. III, pp. 289–305, 1987.

[6] P. Chandra and P. B. Littlewood, "A Landau primer for ferroelectrics," *Top. Appl. Phys.*, vol. 105, pp. 69–116, 2007.

[7] D. Damjanovic, "Ferroelectric, dielectric and piezoelectric properties of ferroelectric thin films and ceramics," *Reports Prog. Phys.*, vol. 61, no. 9, p. 1267, 1999.

[8] A. A. Bokov and Z. G. Ye, "Recent progress in relaxor ferroelectrics with perovskite structure," *J. Mater. Sci.*, vol. 41, no. 1, pp. 31–52, 2006.

[9] S. O. Leontsev and R. E. Eitel, "Progress in engineering high strain lead-free piezoelectric ceramics," *Sci. Technol. Adv. Mater.*, vol. 11, no. 4, p. 044302, 2010.

[10] B. Noheda, D. E. Cox, G. Shirane, J. A. Gonzalo, L. E. Cross, and S. E. Park, "A monoclinic ferroelectric phase in the $Pb(Zr_{1-x}Ti_x)O_3$ solid solution," *Appl. Phys. Lett.*, vol. 2059, no. 1999, p. 6, 1999.

[11] D. Damjanovic, "Stress and frequency dependence of the direct piezoelectric effect in ferroelectric ceramics," *J. Appl. Phys.*, vol. 82, no. 4, pp. 1788–1797, 1997.

[12] N. Bassiri-Gharb, I. Fujii, E. Hong, S. Trolier-Mckinstry, D. V. Taylor, and D. Damjanovic, "Domain wall contributions to the properties of piezoelectric thin films," *J. Electroceramics*, vol. 19, no. 1, pp. 47–65, 2007.

[13] F. Griggio, S. Jesse, A. Kumar, O. Ovchinnikov, H. Kim, T. N. Jackson, D. Damjanovic, S. V. Kalinin, and S. Trolier-Mckinstry, "Substrate clamping effects on irreversible domain wall dynamics in lead zirconate titanate thin films," *Phys. Rev. Lett.*, vol. 108, no. 15, pp. 1–5, 2012.

[14] V. Nagarajan, a Roytburd, a Stanishevsky, S. Prasertchoung, T. Zhao, L. Chen, J. Melngailis, O. Auciello, and R. Ramesh, "Dynamics of ferroelastic domains in ferroelectric thin films.," *Nat. Mater.*, vol. 2, no. 1, pp. 43–47, 2003.

[15] K. Uchino, "Applications of lead-free piezoelectrics," in *Lead-free piezoelectrics*, S. Priya and S. Nahm, Eds. 2012, p. 511.

[16] J. C. Shin, C. S. Hwang, H. J. Kim, and S. O. Park, "Leakage current of sol-gel derived Pb(Zr,Ti)O_3 thin films having Pt electrodes," *Appl. Phys. Lett.*, vol. 75, no. 21, p. 3411, 1999.
[17] M. M. Hejazi and A. Safari, "Temperature-dependent leakage current behavior of epitaxial $Bi_{0.5}Na_{0.5}TiO_3$-based thin films made by pulsed laser deposition," *J. Appl. Phys.*, vol. 110, no. 10, p. 103710, 2011.
[18] G. W. Dietz, W. Antpöhler, M. Klee, and R. Waser, "Electrode influence on the charge transport through $SrTiO_3$ thin films," *J. Appl. Phys.*, vol. 78, no. 10, pp. 6113–6121, 1995.
[19] G. W. Dietz, M. Schumacher, R. Waser, S. K. Streiffer, C. Basceri, and A I. Kingon, "Leakage currents in $Ba_{0.7}Sr_{0.3}TiO_3$ thin films for ultrahigh-density dynamic random access memories," *J. Appl. Phys.*, vol. 82, no. 1997, pp. 2359–2364, 1997.
[20] S. Zafar, R. E. Jones, B. Jiang, B. White, V. Kaushik, and S. Gillespie, "The electronic conduction mechanism in barium strontium titanate thin films," *Appl. Phys. Lett.*, vol. 73, no. 24, pp. 3533–3535, 1998.
[21] J. G. Simmons, "Richardson-Schottky effect in solids," *Phys. Rev. Lett.*, vol. 15, no. 25, pp. 967–968, 1965.
[22] F. Chiu, "A review on conduction mechanisms in dielectric films," *Adv. Mater. Sci. Eng.*, p. 578168, 2014.
[23] S. Zafar, R. E. Jones, B. Jiang, B. White, P. Chu, D. Taylor, and S. Gillespie, "Oxygen vacancy mobility determined from current measurements in thin $Ba_{0.5}Sr_{0.5}TiO_3$ films," *Appl. Phys. Lett.*, vol. 73, no. 2, pp. 175–177, 1998.
[24] R. Meyer, R. Liedtke, and R. Waser, "Oxygen vacancy migration and time-dependent leakage current behavior of $Ba_{0.3}Sr_{0.7}TiO_3$ thin films," *Appl. Phys. Lett.*, vol. 86, no. 11, pp. 1–3, 2005.
[25] J. P. Manceau, S. Bruyere, S. Jeannot, A. Sylvestre, and P. Gonon, "Metal-insulator-metal capacitors' current instability improvement using dielectric stacks to prevent oxygen vacancies formation," *Appl. Phys. Lett.*, vol. 91, no. 13, pp. 1–4, 2007.
[26] J. Wang and S. Trolier-Mckinstry, "Oxygen vacancy motion in Er-doped barium strontium titanate thin films," *Appl. Phys. Lett.*, vol. 89, no. 17, pp. 1–4, 2006.
[27] J. Rödel, W. Jo, K. T. P. Seifert, E. M. Anton, T. Granzow, and D. Damjanovic, "Perspective on the development of lead-free piezoceramics," *J. Am. Ceram. Soc.*, vol. 92, no. 6, pp. 1153–1177, 2009.
[28] N. Kumar, T. Y. Ansell, and D. P. Cann, "Role of point defects in bipolar fatigue behavior of $Bi(Mg_{1/2}Ti_{1/2})O_3$ modified $(Bi_{1/2}K_{1/2})TiO_3$-$(Bi_{1/2}Na_{1/2})TiO_3$ relaxor ceramics," *J. Appl. Phys.*, vol. 115, no. 15, p. 154104, 2014.
[29] P. Jarupoom, E. Patterson, B. Gibbons, G. Rujijanagul, R. Yimnirun, and D. Cann, "Lead-free ternary perovskite compounds with large electromechanical strains," *Appl. Phys. Lett.*, vol. 99, no. 15, pp. 1–4, 2011.
[30] Q. Wang, J. Chen, L. Fan, L. Liu, L. Fang, and X. Xing, "Preparation and electric properties of $Bi_{0.5}Na_{0.5}TiO_3$-$Bi(Mg_{0.5}Ti_{0.5})O_3$ lead-free piezoceramics," *J. Am. Ceram. Soc.*, vol. 96, no. 4, pp. 1171–1175, 2013.
[31] Y. H. Jeon, E. A. Patterson, D. P. Cann, P. Mardilovich, W. Stickel, and B. J. Gibbons, "Large piezoresponse and ferroelectric properties of $(Bi_{0.5}Na_{0.5})TiO_3$-

$(Bi_{0.5}K_{0.5})TiO_3$-$Bi(Mg_{0.5}Ti_{0.5})O_3$ thin films prepared by chemical solution deposition," *J. Am. Ceram. Soc.*, vol. 96, no. 7, pp. 2172–2178, 2013.

[32] A. Singh and R. Chatterjee, "Structural, electrical, and strain properties of stoichiometric $1-x-y(Bi_{0.5}Na_{0.5})TiO_3-x(Bi_{0.5}K_{0.5}TiO_3)-y(Na_{0.5}K_{0.5})NbO_3$ solid solutions," *J. Appl. Phys.*, vol. 109, no. 2, p. 024105, 2011.

[33] Z. Cao, A. Ding, X. He, W. Cheng, and P. Qiu, "Optical properties of BNT thin films grown on $Pt/Ti/SiO_2/Si(100)$ substrates by a CSD processing," *J. Cryst. Growth*, vol. 270, no. 1–2, pp. 168–173, 2004.

[34] Z. H. Zhou, J. M. Xue, W. Z. Li, J. Wang, H. Zhu, and J. M. Miao, "Leakage current and charge carriers in $(Na_{0.5}Bi_{0.5})TiO_3$ thin film," *J. Phys. D. Appl. Phys.*, vol. 38, no. 4, pp. 642–648, 2005.

[35] S. K. Acharya, B. G. Ahn, C. U. Jung, J. H. Koh, I. H. Choi, and S. K. Lee, "Effect of Rb doping on ferroelectric and piezoelectric properties of $Bi_{0.5}Na_{0.5}TiO_3$-$BaTiO_3$ thin films," *J. Alloys Compd.*, vol. 603, no. 2014, pp. 248–254, 2014.

[36] W. Li, H. Zeng, J. Hao, and J. Zhai, "Enhanced dielectric and piezoelectric properties of Mn doped $(Bi_{0.5}Na_{0.5})TiO_3$–$(Bi_{0.5}K_{0.5})TiO_3$–$SrTiO_3$ thin films," *J. Alloys Compd.*, vol. 580, pp. 157–161, 2013.

[37] M. M. Hejazi, E. Taghaddos, and A. Safari, "Reduced leakage current and enhanced ferroelectric properties in Mn-doped $Bi_{0.5}Na_{0.5}TiO_3$-based thin films," *J. Mater. Sci.*, vol. 48, no. 9, pp. 3511–3516, 2013.

[38] C. W. Ahn, S. Y. Lee, H. J. Lee, A. Ullah, J. S. Bae, E. D. Jeong, J. S. Choi, B. H. Park, and I. W. Kim, "The effect of K and Na excess on the ferroelectric and piezoelectric properties of $K_{0.5}Na_{0.5}NbO_3$ thin films," *J. Phys. D. Appl. Phys.*, vol. 42, no. 21, p. 215304, 2009.

[39] Y. Nakashima, W. Sakamoto, H. Maiwa, T. Shimura, and T. Yogo, "Lead-free piezoelectric $(K,Na)NbO_3$ thin films derived from metal alkoxide precursors," *Japanese J. Appl. Physics, Part 2 Lett.*, vol. 46, no. 12–16, pp. 4–7, 2007.

[40] M. Abazari, E. K. Akdoğan, and A. Safari, "Dielectric and ferroelectric properties of strain-relieved epitaxial lead-free KNN-LT-LS ferroelectric thin films on $SrTiO_3$ substrates," *J. Appl. Phys.*, vol. 103, no. 10, pp. 0–6, 2008.

[41] A. Tian, W. Ren, L. Wang, P. Shi, X. Chen, X. Wu, and X. Yao, "Effect of deposition temperature on orientation and electrical properties of $(K_{0.5}Na_{0.5})NbO_3$ thin films by pulsed laser deposition," *Appl. Surf. Sci.*, vol. 258, no. 7, pp. 2674–2678, 2012.

[42] M. Abazari, T. Choi, S. W. Cheong, and A. Safari, "Nanoscale characterization and local piezoelectric properties of lead-free KNN-LT-LS thin films," *J. Phys. D. Appl. Phys.*, vol. 43, no. 2, p. 025405, 2009.

[43] Y. Wang and J. Wang, "Modulated charged defects and conduction behaviour in doped $BiFeO_3$ thin films," *J. Phys. D. Appl. Phys.*, vol. 42, no. 16, p. 162001, 2009.

[44] J. Wu, J. Wang, D. Xiao, and J. Zhu, "Leakage mechanism of cation -modified $BiFeO_3$ thin film," *AIP Adv.*, vol. 1, no. 2, pp. 0–10, 2011.

[45] G. W. Pabst, L. W. Martin, Y.-H. Chu, and R. Ramesh, "Leakage mechanisms in $BiFeO_3$ thin films," *Appl. Phys. Lett.*, vol. 90, no. 7, p. 72902, 2007.

[46] C. F. Chung, J. P. Lin, and J. M. Wu, "Influence of Mn and Nb dopants on electric properties of chemical-solution-deposited $BiFeO_3$ films," *Appl. Phys. Lett.*, vol. 88, no. 24, pp. 3–6, 2006.
[47] Z. Zhong and H. Ishiwara, "Variation of leakage current mechanisms by ion substitution in $BiFeO_3$ thin films," *Appl. Phys. Lett.*, vol. 95, no. 11, pp. 2007–2010, 2009.
[48] C. S. Hwang, B. T. Lee, C. S. Kang, K. H. Lee, H. J. Cho, H. Hideki, W. D. Kim, S. I. Lee, and M. Y. Lee, "Depletion layer thickness and Schottky type carrier injection at the interface between Pt electrodes and (Ba,Sr)TiO_3 thin films," *J. Appl. Phys.*, vol. 85, no. 1, pp. 287–295, 1999.
[49] J. F. Scott, "Depletion width in $SrTiO_3$ and $Ba_xSr_{1-x}TiO_3$ films," *Ferroelectrics*, vol. 232, no. 1, pp. 25–34, 1999.
[50] S. Maruno, T. Kuroiwa, N. Mikami, K. Sato, S. Ohmura, M. Kaida, T. Yasue, and T. Koshikawa, "Model of leakage characteristics of (Ba,Sr)TiO_3 thin films," *Appl. Phys. Lett.*, vol. 73, no. 7, p. 954, 1998.
[51] S. T. Chang and J. Y. Lee, "Electrical conduction mechanism in high-dielectric-constant $(Ba_{0.5}Sr_{0.5})TiO_3$ thin films," *Appl. Phys. Lett.*, vol. 80, no. 4, p. 655, 2002.

3. Experimental procedures

3.1 Chemical solution deposition (CSD)

Solutions were fabricated by an inverted mixing order synthesis [1][2]. The process is described visually in Fig. 3.1a. In preparation, bismuth (III) acetate (99.9999%, Alfa Aesar) was dissolved in a known weight of propionic acid (PAc). In another bottle, sodium (I) acetate trihydrate (99%, Macron) and potassium (I) acetate (99%, Macron) were dissolved in a known weight of dry methanol. In a glove box, an approximately correct volume of titanium isopropoxide (98+ %, but better than 99% by assay, Alfa Aesar) was quickly added to four molar equivalents of acetic acid mixed with an equal volume of PAc. The weight of the Ti added to the solvents was recorded. The reaction of the acetic acid stabilizes the Ti against polymerization by exchanging the isopropoxide ligands. The purpose of the PAc is to slow the exothermic reaction and dilute the generated heat.

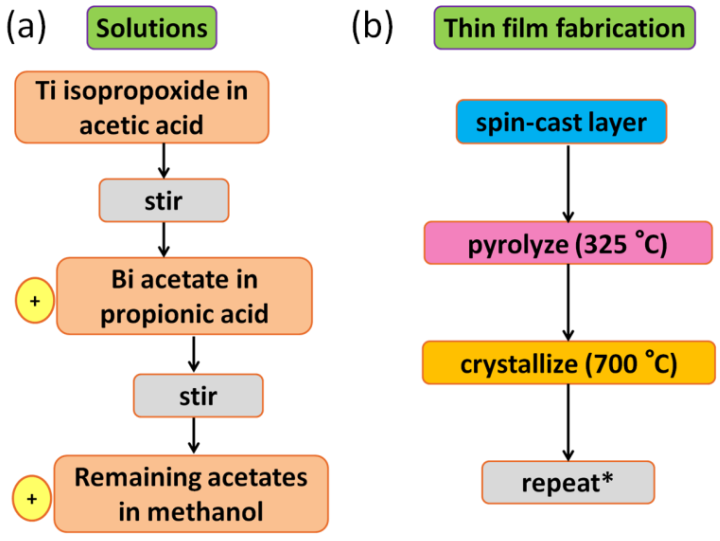

Figure 3.1 – *(a) Solutions were made by an inverted mixing order. (b) The procedure for film fabrication required a pyrolysis and crystallization every layer.*

Exact quantities of Bi and (Na, K) solutions to add to the Ti are calculated based

on the weights of the solutes and solvents, and the known weight of Ti is added. The correct Bi solution was quickly added first to the Ti solution dropwise. This was stirred for at least one hour. Then the Na, K solution was added, also by weight. The resulting solution concentration was approximately 0.5 mol/L solvent. The estimated error in the final ratios of Bi:Ti and (Na, K):Bi is better than 0.6 %. The resulting solutions should be kept away from ultraviolet radiation (e.g. sunlight). This can cause ageing, which is thought to be caused by polymerization of the tetravalent titanium.

Solutions were spin-cast on sputtered platinized silicon substrates at 3000 rpm for 30 s (Fig. 3.1b). Each layer was pyrolyzed at 325 °C for 4 min and crystallized at 700 °C for 10 min. Films crystallized in a box furnace had significantly better properties than those crystallized in a tube furnace, regardless of temperature. It is suspected that this may have been due to the heating rate. Also, a crystallization step between each layer was required in order to achieve good dielectric and ferroelectric properties [3]. Platinum top electrodes were deposited through a shadow mask by dc magnetron sputtering to complete the parallel plate capacitor structure.

The solution and film fabrication procedures above were based on those of Jeon, *et al.*, with only slight modifications [4][5].

3.2 Characterization methods and equipment

X-ray diffraction was performed on a Bruker AXS D8 Discover diffraction system with Cu Kα radiation. Film thickness was modelled from data acquired on a variable angle spectroscopic ellipsometer (V-VASE, J.A. Woollam). Films were modeled Cauchy layer with wavelength (λ) in the range of 500 to 1500 nm,

$$n(\lambda) = A + \frac{B}{\lambda^2} + \frac{C}{\lambda^4}. \qquad (3.1)$$

Equation 3.1 can be used to accurately model the index of refraction and thickness for an isotropic film when λ is sufficiently removed in energy from the band gap, i.e. when the films are transparent.

An Asylum MFP-3D was used for atomic force microscopy in ac (intermittent

contact) mode. Cantilevers (TAP-150G, Budget Sensors) had a stiffness of 5 N/m and a free air resonant frequency of around 150 kHz.

Dielectric measurements were carried out using an HP 4192A impedance analyzer operating with a 50 mV_{RMS} test signal. For a typical 200 nm thick film, for example, this works out to 2.5 kV/cm, or approximately $0.05E_c$. Polarization hysteresis was measured with a Radiant Technologies RT66B, with a loop period of 5 ~ 1000 ms. An aixACCT double beam laser interferometer (DBLI) was used to assess the piezoelectric properties, as well as polarization hysteresis at higher frequencies.

3.3 Leakage current measurements

This section details the collection of dc leakage data using the Radiant RT66B ferroelectric tester and the Keithley 236 source-measure unit (K236). The RT66B provides current-time, $J(t)$, data with up to 1 ms resolution at short times 100 ms>t>8 s, although for larger currents the instrument is limited to t>1 s. The K236 provides J-t data at long times, up to minutes or hours, at the expense of resolution. The combination of these two instruments allows for observation of the conduction behavior over a wide range of times.

For temperature dependent leakage current ($J(T)$ measurements) samples were bonded to a hot plate surface with silver paste. The sample was electrically insulated from the hot plate by first mounting samples on a thin (0.20 mm) glass slide. The temperature of the combined mounting slide and sample was calibrated using an infrared thermometer (Fluke 59 MAX).

For measurements on the RT66B, the leakage current was measured using the software Vision version 5.6.1. A leakage current measurement routine was programmed in the Vision software, to automate testing over a range of voltages. The procedure is detailed below.

i. The leakage current was tested at one voltage level and then the voltage was iterated to a slightly higher level, and this was continued as in Fig. 3.2. As a starting point a

'low' voltage was assumed corresponding to around 10 kV/cm. The voltage increment was set to scale the voltage by a factor, typically 1.12 (e.g. V_1=0.2 V, V_2=0.224, ...). This was done in order to obtain a set number of data points spaced equally when plotted on a log scale.

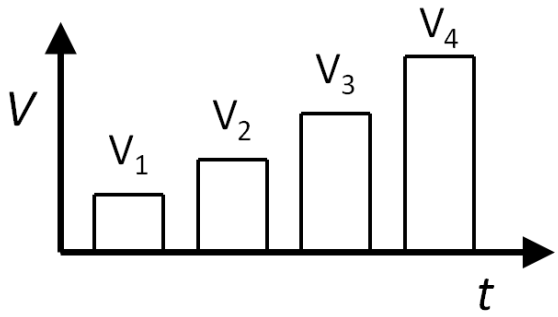

Figure 3.2 – *Leakage current measurement profile showing the voltage increment.*

ii. Within a measurement at each voltage level a soak time of 500 ms was applied, where the voltage was applied but the current was not measured to avoid saturating the unit. The current was then measured for 500 ms. The measurement voltage-time profile is shown in Fig. 3.3.

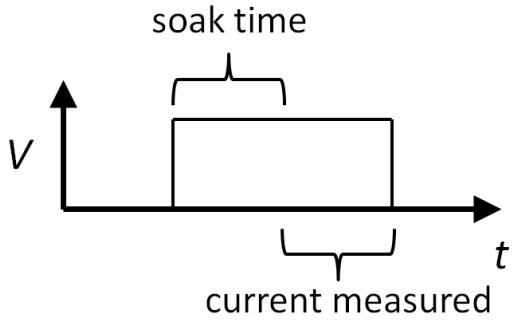

Figure 3.3 – *Leakage current measurement profile showing the soak and measure segments in the voltage-time function.*

iii. The current dependence on voltage was obtained from the $J(t)$ data as follows. The ln$J$-ln$t$ curves were plotted in order to verify that the current had reached the steady state. The average value of the last 5 percent of the *J-t* data was taken as the steady state leakage current at each voltage, $J(V)$.

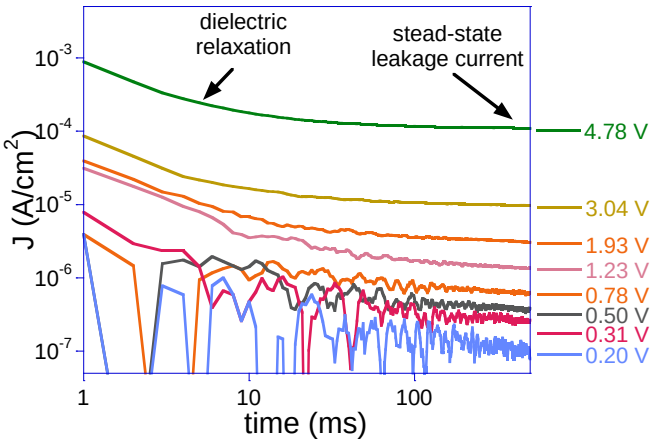

Figure 3.4 – *Steady state leakage current was obtained after the period of dielectric relaxation.*

iv. The leakage current $J(V)$ could then be plotted on different scales in order to determine the leakage current mechanism. For example, it can be ascertained whether the current is space charge-limited by plotting on a ln$J$-ln$V$ scale, as in Fig. 2.7.

For the current measurements $J(t)$ at longer times, the current was measured using the K236. A custom Labview program was used to operate the device. This allowed a voltage or series of voltages to be applied for a set duration (e.g. 500 s), with current measurements taken at preprogrammed intervals (e.g. 500 ms). The longer durations permitted by this instrument made observing the transient current peaks and the onset of resistance degradation possible, at higher temperatures. However, the noise level was higher than the RT66B in the nA range and the limited time resolution made it difficult to see the dielectric relaxation behavior. As a result, both the RT66B and the K236 compliment each other well when attempting to observe a wide range of conduction behaviors.

3.4 Descriptions of materials characterization techniques

3.4.1 X-ray diffraction

X-ray diffraction (XRD) is used for phase identification and crystal texture analysis. A sample is bombarded with a beam of coherent and parallel x-rays of

wavelength λ which diffract and scatter off the crystal lattice planes in the top several microns of the sample to be collected at a detector. The angle between the source and detector is 2θ. Usually the scattering results in destructive interference and a low background signal is detected. However, when the condition of Bragg's law is met:

$$n\lambda = 2d\sin\theta, \quad (3.2)$$

the interference is constructive and an increase in intensity is observed. In Eq. 3.2, d is the interatomic spacing, or lattice parameter, and n is an integer marking the order of the peak. The positions and relative intensities of peaks allow for identification of the material(s) present. In the case of impurity phases being present in the material, extra peaks will show up in the scan of intensity versus 2θ.

3.4.2 Atomic force microscopy

A very useful tool for characterization of the typology of grains and surfaces, atomic force microscopy (AFM) is a different kind of microscope. Rather than using an electron, atomic, or light beam to probe a surface, the AFM uses a sharp tip of nanometer-scale radius (suspended at the end of a cantilever) dragged across the surface, similar to a vinyl record player. There are two basic operating modes: ac mode and contact mode. In ac mode, the cantilever is driven to tap upon the surface by a piezoelectric driving unit. A super luminescent diode (SLD) reflects a beam of light off of the top of the cantilever onto a photodetector array which converts the signal into a voltage. Variations in the terrain are accounted for adjusting the vertical offset-displacement, Z-voltage, of the piezoelectric driving unit to maintain a constant point-to-point voltage in the photodetector. The offset, Z-voltage and photodetector are used to fit the height of the sample at a given point. Contact mode is similar to ac mode except that the ac signal is absent. Contact mode generally gives higher quality images on very smooth surfaces.

3.4.3 Polarization measurements

Dielectric properties are performed by an impedance analyzer, which calculates the complex capacitance from the phase shift of the voltage and current time derivatives, dV/dt and dI/dt. Ferroelectric hysteresis is essentially a careful measurement of integrated current as a function of applied E.

3.4.4 Dual beam laser interferometry

The macroscopic piezoelectric response and $d_{33,f}$ can be determined using dual beam laser interferometry (DBLI). Two in-phase, probing laser beams are split off the reference beam and reflected off of the top electrode and back side of the substrate, as shown in Fig. 3.5.

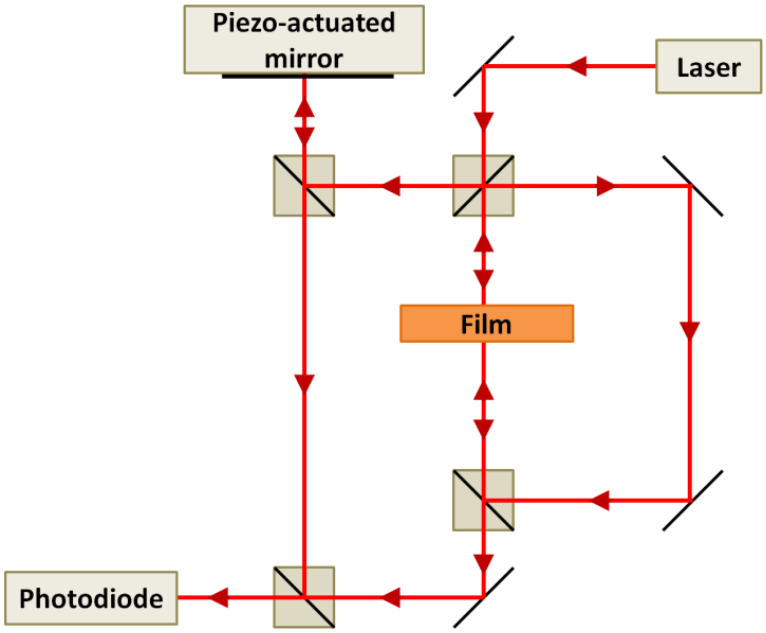

Figure 3.5 – *Schematic of a DBLI showing the beam path.*

The reference beam is Doppler-shifted by a known amount and when recombined with the probe beam generates a low frequency (several tens of kHz) beat intensity on a photodiode. When a low frequency ac voltage is applied to the electrodes the sample is strained out-of-plane causing a shift in the probe frequency. Ideally, the beat frequency is shifted by an amount proportional to the Doppler shift caused by the sample acceleration. In bulk materials, what is reported is often the average piezoelectric coefficient obtained as $d_{33}^{*}=S_{max}/E_{max}$. In thin films, substrate clamping can lead to reduction in the observed strain, and so the relevant parameter is known as the effective piezoelectric, $d_{33,f}$.

References

[1] R. W. Schwartz, R. A. Assink, and T. J. Headley, "Spectroscopic and microstructural characterization of solution chemistry effects in PZT thin film processing," *Symp. Ferroelectr. Thin Film. II*, pp. 245–254, 1991.

[2] R. A. Assink and R. W. Schwartz, "^{1}H and ^{13}C NMR investigations of Pb(Zr,Ti)O_3 thin-film precursor solutions," *Chem. Mater.*, vol. 5, pp. 511–517, 1993.

[3] Y. H. Jeon, “Development of Bi-based lead-free piezoelectric materials: thin film piezoelectric materials via PVD and CSD routes,” 2012.

[4] Y. H. Jeon, E. A. Patterson, D. P. Cann, P. Mardilovich, W. Stickel, and B. J. Gibbons, “Large piezoresponse and ferroelectric properties of $(Bi_{0.5}Na_{0.5})$ TiO_3-$(Bi_{0.5}K_{0.5})$ TiO_3-Bi $(Mg_{0.5}Ti_{0.5})O_3$ thin films prepared by chemical solution deposition,” *J. Am. Ceram. Soc.*, vol. 96, no. 7, pp. 2172–2178, 2013.

[5] Y. H. Jeon, E. A. Patterson, D. P. Cann, and B. J. Gibbons, “Dielectric and ferroelectric properties of $(Bi_{0.5}Na_{0.5})TiO_3$-$(Bi_{0.5}K_{0.5})TiO_3$-$BaTiO_3$ thin films deposited via chemical solution deposition,” *Mater. Lett.*, vol. 106, pp. 63–66, 2013.

4. Leakage current phenomena in Mn-doped $Bi(Na,K)TiO_3$-based ferroelectric thin films

4.1 Introduction

$(100-x)(Bi_{0.5}Na_{0.5})TiO_3$-$x(Bi_{0.5}K_{0.5})TiO_3$ (BNT-BKT) is a good candidate to replace Pb-based materials in ferroelectric and piezoelectric devices, which are to be phased out of consumer products as part of the worldwide restrictions on the use of toxic elements (i.e., the Restrictions on Hazardous Substances (RoHS) guidelines) [1]. In this binary system, a region of enhanced dielectric, ferroelectric, and piezoelectric properties occurs between x=16 and x=20, where it is commonly accepted that a morphotropic phase boundary exists [1][2][3].Because of this, all of the data reported in this work are for 80BNT-20BKT. Although there is a pressing need for commercial alternatives, due to the relatively new interest in these materials and the great variety of Pb-free alternatives the knowledge base of performance-related data is far smaller than that of Pb-based compounds. One example of this for thin film embodiments of these materials is the direct current (DC) leakage behavior. Due to the high electric fields to which they are routinely subjected, large leakage currents are often observed which can affect device efficiency and reliability. Furthermore, the alkali metal and Bi cations on which BNT-BKT is based are highly volatile. This potentially leads to large numbers of defects, including oxygen and cation vacancies, which can affect the long-term stability due to resistance degradation.

There are several decades of literature showing that acceptor doping perovskite ceramics (ABO_3) with Mn can reduce both leakage current and resistance degradation [4][5][6]. Acceptor doping on the B-site is often associated with a reduced leakage current [7]. This has also been demonstrated in BNT-based thin films [8][9][10]. However, the temperature dependence of Mn-doped BNT-based thin films has not been previously reported. Observation and analysis of this temperature dependence is required to validate the conduction model and extract key materials parameters, such as the carrier concentrations and mobilities. The exact mechanism by which Mn-doping works is not entirely clear, with several possible explanations. Mn can be added to the lattice as Mn^{2+}, Mn^{3+}, or Mn^{4+}. When added as Mn^{2+}, the reactions are thought to follow the pathway [8]:

$$MnO \xrightarrow{TiO_2} Mn''_{Ti}+V_O^{\cdot\cdot}+1/2O_2, \quad (4.1)$$

$$1/2O_2+V_O^{\cdot\cdot} \longleftrightarrow O_O^x+2h^{\cdot}, \quad (4.2)$$

$$Mn''_{Ti}+h^{\cdot} \longleftrightarrow Mn'_{Ti}. \quad (4.3)$$

The small radius of the Mn cation substitutes well for Ti^{4+}. Equation (4.1) shows the corresponding extrinsic loss of oxygen. If oxidation is thermodynamically favorable, then those oxygen vacancies can be reoxidized to generate $h^{\cdot}$. The multiple valence states allowed for Mn are shown by example in Eq. (4.3) where $Mn_{Ti}^{//}$ absorbs an $h^{\cdot}$.

These films also contain intrinsic defects due to volatilization of Bi_2O_3, Na_2O, and K_2O. The formation of these defects are described by

$$2Bi_{Bi}+3O_O \longrightarrow 2V'''_{Bi}+3V_O^{\cdot\cdot}+Bi_2O_3, \quad (4.4)$$

$$2Na_{Na}+O_O \longrightarrow 2V'_{Na}+V_O^{\cdot\cdot}+Na_2O. \quad (4.5)$$

Although electrically neutral, these defects form trap states. The $V_O^{\cdot\cdot}$ formed by these reactions may also undergo reoxidation, resulting in p-type conductivity. The generation of electrons may proceed by the reduction reaction

$$O_O \longrightarrow 1/2O_2+V_O^{\cdot\cdot}+2e'. \quad (4.6)$$

The reduction reaction has been repeatedly verified in many different titanate perovskites [11]. Given the likelihood of oxygen vacancies combined with several volatile cations with different valences, films exhibiting both electron and hole conduction are a strong possibility [12]. However, the presence of highly volatile A-site cations suggests that there may be a majority, or at least a significant amount, of p-type carriers present in BNT-BKT thin films [13]. Several authors have linked the reduced leakage current of Mn-doped thin films to $h^{\cdot}$ trapping, although this has not yet been determined rigorously [8][10][13][14].

There are several other interesting phenomena that have previously been observed in other ferroelectric thin films, but have not yet been explored in BNT-based thin films. These are negative differential resistivity (NDR) and positive temperature coefficient of resistance (PTCR), referring to the decrease in the DC current with increasing electric field and temperature, respectively. They have been reported as occurring together in $BaTiO_3$ (BT), $(Ba,Sr)TiO_3$ (BST), $SrBi_2Ta_2O_9$ (SBT) and possibly $Ba(Zr_{0.05}Ti_{0.95})O_3$ [15][16][17]. The PTCR effect is utilized in PTC thermistors, which prevent device failure due to thermal runaway [18]. In the case of $Pb(Zr,Ti)O_3$ (PZT) thin films, apparent

NDR has been shown to be an artifact caused by a change in the dielectric relaxation behavior, though in BST the effect has persisted to longer soak times [15][19][20].

Another feature observed in the DC current versus time (*J-t*) relationship is oxygen vacancy migration. The migration of oxygen vacancies is believed, by some, to be responsible for the resistance degradation and ultimately device failure under DC fields [6]. Transient current peaks were originally thought to be related to oxygen vacancy migration but a later mechanism, proposed by Meyer, *et al.*, links this defect migration to a modulation of electron concentration [21][22]. Mn-doping may limit oxygen vacancy migration by formation of bulky Mn_{Ti}''-$V_O^{\bullet\bullet}$ complexes [23]. Transient current peaks were also found in the BNT-BKT films presented here, and we report on some differences observed between the undoped and doped films.

4.2 Experimental

Films were fabricated by chemical solution deposition (CSD). Bismuth (III) acetate (99.9999%, Alpha Aesar) was dissolved in propionic acid while sodium acetate trihydrate (99%, Macron) and potassium acetate (99%, Macron) were dissolved in methanol. Optimized excesses of Bi (8 mol%), Na (16 mol%) and K (16 mol%) were added to the solutions in order to achieve stoichiometry, since the A-site cations are considered to be highly volatile at the crystallization temperature [24][25]. In an atmosphere controlled glove box titanium (IV) isopropoxide (97 %, TCI) was added to a mixture of 0.6 mL acetic acid and 0.6 mL propionic acid. The total ratio of propionic acid to methanol was 2.25. The Bi solution was added to the Ti solution and allowed to stir for several hours before adding the Na, K solution. Manganese (II) acetate tetrahydrate (99 %, Acrōs Organics) was added at the conclusion of solution preparation. The total solution concentration was 0.5 M.

Films were spin cast on $Pt/TiO_2/SiO_2/Si$ substrates at 3000 rpm for 30 s. Each layer was pyrolyzed at 325 °C for 4 min and crystallized at 700 °C for 10 min in air in a box furnace. This process was repeated to achieve the desired thickness. Platinum top electrodes were deposited by dc magnetron sputtering through a shadow mask and were subsequently annealed *ex situ* at 450 °C in air prior to electrical characterization. The

resulting parallel plate capacitor structures were circular, having an area 7.06×10^{-4} cm^2. The electrode area was measured using an optical microscope.

Variable angle spectroscopic ellipsometry (V-VASE, J.A. Woollam Co. Inc.) was used to determine film thickness and optical properties. X-ray diffraction (XRD) was used to ascertain phase purity and crystallinity (Bruker AXS D8 Discover). Atomic force microscopy (AFM, Asylum MFP-3D) was used to observe the surface topography and roughness. Dielectric measurements were carried out using an impedance analyzer (HP 4192A) at 50 mV_{RMS}. Leakage current and polarization measurements were performed on a Radiant RT66B ferroelectric tester. Leakage current was measured after a 400 ms soak time. The hysteresis behavior was measured with a 5 ms (200 Hz) measurement period. Leakage current measurements on time scales of tens to hundreds of seconds were performed on a Keithley 236 source-measure unit. For all leakage current measurements the convention where bias is applied to the top electrode was utilized.

4.3 Results

The films were deposited in three layers with a final thickness of 210 nm. Phase purity was achievable for undoped films and films with up to 2 mol% Mn. Only perovskite and substrate peaks were observed in the XRD patterns (Fig. 4.1) [26]. Studies on the use of Mn in $BiFeO_3$ and $PbTiO_3$-based multiferroics have used concentrations of Mn as high as 30 mol% without observing a second phase by XRD [27][28]. Peak intensity ratios were roughly the same for all compositions studied here. The films were polycrystalline. An AFM image of an undoped film in Fig. 4.2 shows that the film was composed of small spherical grains of 50-100 nm in diameter. Doped films displayed a very similar microstructure. Overall there appeared to be no difference between the microstructures observed by XRD or AFM in the undoped or Mn-doped films.

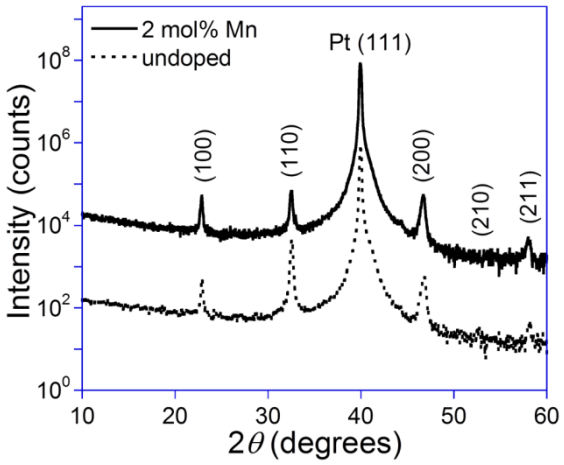

Figure 4.1 – *XRD patterns of undoped and 2 mol% Mn-doped films.*

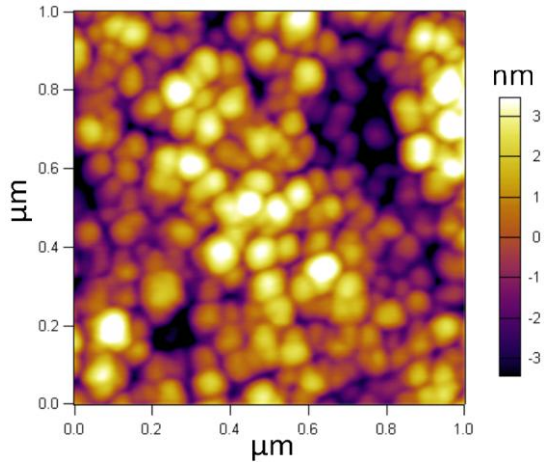

Figure 4.2 – *AFM image of undoped thin film. Similar topography was observed for doped films.*

The dielectric constants, shown in Fig. 4.3, decreased approximately 15% with Mn doping. Similar decreases have been observed in previous work on $SrTiO_3$ and BNT-based thin films [6][8]. Some have reported otherwise [10]. In the bulk, the dielectric constant of Mn-doping of BNT did not change, but decreased significantly in 94($Bi_{0.5}Na_{0.44}Ag_{0.06}TiO_3$)-6BT films doped with 0.4 mol% Mn [29][30]. Dielectric loss was low in all films here, in the range of 2-4 % at 1 kHz.

Typical hysteresis loops for an undoped and 2 mol% Mn doped film are shown in Fig. 4.4. Mn doping of BNT-based films has been variously found to increase and decrease the high-field polarization in epitaxial films deposited by pulsed laser deposition (PLD) on oxide electrodes [8][10]. Here, a small but persistent decrease in the maximum and remanent polarizations was observed in the Mn-doped films. Remanent polarization

was 8 μC/cm^2 with a coercive field near 70 kV/cm, for the undoped films. Measured at room temperature; the loops were initially asymmetric and pinched until application of an electric field equal to or greater than 300 kV/cm. Beyond this field level the loops became symmetric and no longer displayed pinching. This was evidence of some relaxor-like behavior prior to stabilization of the ferroelectric phase on the application of high fields. At 200 Hz films could withstand fields as high as 1.3 MV/cm before electrical breakdown. At lower frequencies (1-20 Hz) space charge effects, such as rounded loops, were noticeable at sufficiently high fields.

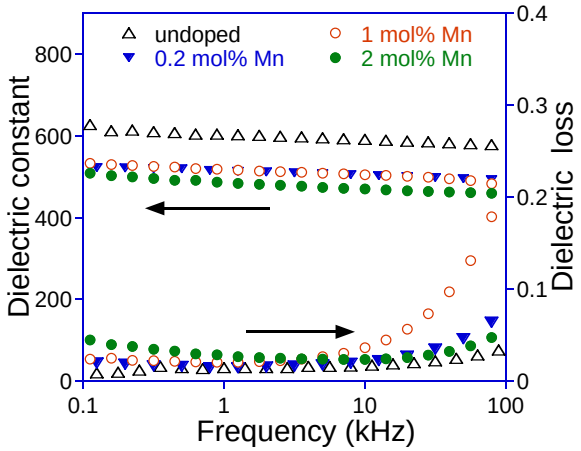

Figure 4.3 – *Dielectric constants and loss for different Mn-doping concentrations of 0 to 2 mol% Mn. The increase in the dielectric loss in at high frequencies is an artifact caused by a resonance in the LCR properties measurement circuit* [31].

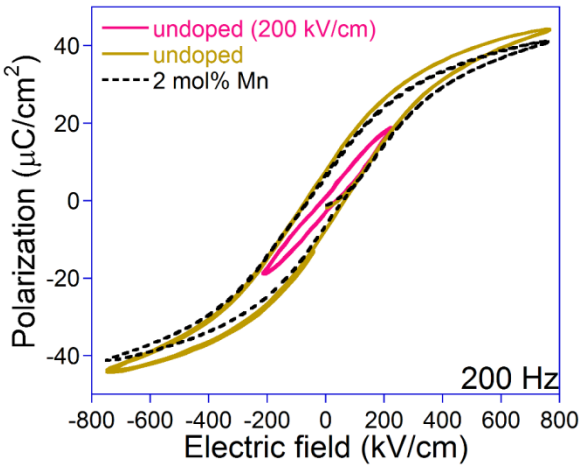

Figure 4.4 – *Hysteresis loops for undoped and 2 mol% Mn films are shown above. The undoped film probed with 200 kV/cm showed some pinching of the loops.*

Several plots of the current-time (*J*-*t*) relationship are shown in Fig. 4.5. At low temperatures we found that the current relaxation continued out to several hundred seconds for positive bias. With negative bias the current relaxation was nearly complete after 100 ms. At high temperatures (>120 °C for the undoped films) we observed a transient current which becomes important even at relatively short time scales (≈1 s). The transient current only appears for positive applied bias. In general, the negative applied bias resulted in larger currents at all time scales, which may have masked the transient effect. This behavior may also have been due to an asymmetric distribution of oxygen vacancies throughout the film, as discussed below.

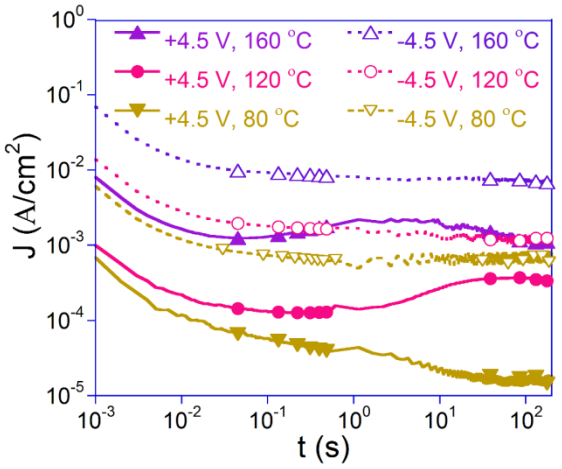

Figure 4.5 – *Leakage current versus time for positive and negative applied bias at intermediate to high temperatures, for an undoped film.*

The transient peaks for an undoped film are plotted on a linear scale in Fig. 4.6a. The time constants (peak positions) were seen to become faster with increasing temperature, and above 160 °C the films began to show signs of resistance degradation marked by a gradual increase in the current. Zafar, *et al*. showed that, for (Ba,Sr)TiO_3 (BST), the current peaks were thermally activated and obeyed equations for diffusion dominated migration [21]. The drift mobility for ionic defects, μ_{ion}, and activation energy, $E_{A,ion}$, can be determined from τ, the peak time constant given in seconds, and D, the thermally activated diffusion coefficient, given in Eqs. (4.7-8), respectively:

$$\tau = \frac{7.8\text{x}10^{-4} d}{\mu_{ion} E}, \tag{4.7}$$

$$D = \gamma \exp\left(-\frac{E_{A,ion}}{k_B T}\right). \tag{4.8}$$

In Eqs. (4.7-8) above, d is the film thickness in units of cm, E is the electric field in units of kV/cm, and γ is a constant giving the maximum diffusion coefficient (at infinite temperature). These are related via the Einstein relation,

$$k_B T \mu_{ion} = qD. \tag{4.9}$$

The Eqs. (4.7-9) can be rearranged to arrive at the form

$$T\mu_{ion} = \left(\frac{\gamma q}{k_B}\right) \exp\left(-\frac{E_{A,ion}}{k_B T}\right), \tag{4.10}$$

which can be used to determine $E_{A,ion}$ from the slope of $\ln T\mu_{ion}$ versus $1/T$.

Fits to data from an undoped film resulted in $\mu_{ion}=1.7\times10^{-12}$ $cm^2V^{-1}s^{-1}$ and $E_{A,ion}=0.92$ eV. These numbers are quite similar to those reported for BT and BST, where the transient currents were ascribed to the diffusion of oxygen vacancies [21][32]. However, Meyer and Waser published a dynamic model for oxygen vacancy diffusion in thin films of BST [22]. They found that the shape of the depletion zone was altered by the oxygen vacancy diffusion and simultaneous charge injection. Thus the appearance of a transient peak is most likely caused by a modulation of the electron concentration due to the oxygen vacancy migration.

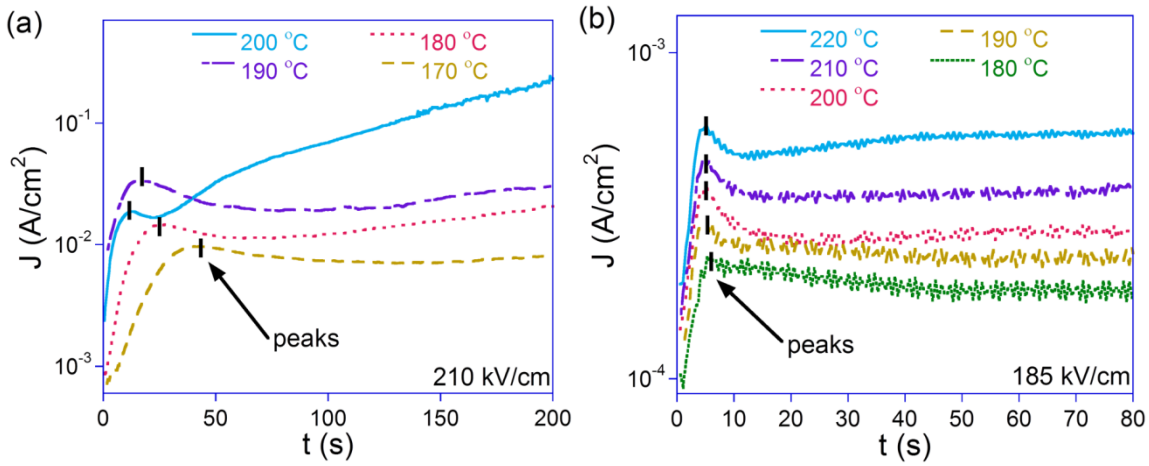

Figure 4.6 – *Oxygen transient current in (a) an undoped film and (b) a film doped with 1 mol% Mn. At these fields (≈200 kV/cm) the leakage current was much lower in the Mn-doped films. At 200 °C the undoped film showed a reduction in total current but also resistance degradation occurring after the peak. Even so, the decrease in the peak time constant was consistent with the model (Eqs. 7-10).*

The transient current peaks of a 1 mol% Mn-doped film, shown in Fig. 4.6b, were much sharper and occurred at much shorter times. The peak had elapsed after only ten seconds and the peak position did not change in the range 180 to 220 °C. The oxygen vacancy diffusion model thus did not provide a good fit for the Mn-doped films. After the current peak there was little sign of resistance degradation, measuring out to 200 s. This is consistent with the known efficacy of Mn-doping on reducing resistance degradation in other systems [6].

With increasing electric field and temperature the current density-electric field (*J-E*) characteristics became asymmetric for the undoped film, as seen in Fig. 4.7a. This

occurred despite the symmetric Pt top and bottom electrodes. The asymmetry gradually diminished by addition of Mn and by 2 mol% the positive and negative voltage leakage current curves in Fig. 4.7b were symmetric. The *J-E* curves are divided into several regions depending on electric field and temperature. At all fields less than around 150 kV/cm the current was Ohmic, increasing proportional to *E* and monotonically with temperature.

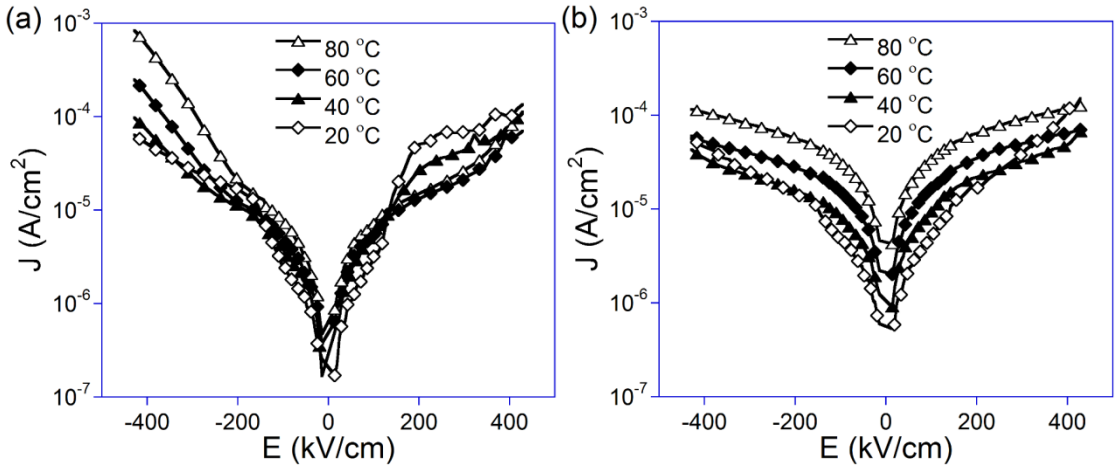

Figure 4.7 – *Low temperature leakage current of (a) undoped film and (b) 2 mol% Mn-doped film. The small PTCR effect in the 2 mol% film became Ohmic at 40 °C and above.*

For the undoped, 210 nm thick films in Fig. 4.7a, the *J-E* characteristics above 150 kV/cm took different forms depending on the measurement temperature. Both PTCR and NDR effects were seen in the temperature range 20~60 °C. Below 60 °C there was an increase in the slope of the *J-E* plot followed by a plateau, which together formed a knee. In thicker films (e.g. 350 nm and 495 nm, data not shown here) a region of NDR appeared in the same *E*-field region. Both the PTCR and NDR were more significant for positive applied bias and the knee vanished at temperatures higher than 60 °C, so it is reasonable to assume that the two phenomena are related. The knee became less noticeable with larger amounts of Mn-doping, and was only minimally noticeable by 2 mol% Mn doping. Above 60 °C in the high-*E* region the *J-E* curves exhibited space-charge-limited current behavior.

4.4 Discussion

4.4.1 Space charge-limited current

Figure 4.8a shows the ln*J*-ln*E* plots for an undoped film at several temperatures from 20-180 °C. Both the Ohmic region at low-*E* and the high-*E* conduction mechanisms are evident. Figure 4.8b shows the *J*-*E* plots for a 2 mol% Mn-doped film, all of which were absent any feature aside from the Ohmic region. In contrast to films with lower Mn-doping levels, Ohmic conduction was preserved until dielectric breakdown even up to 180 °C and 400 kV/cm. Similar Ohmic behavior was previously reported for 2 mol% Mn-doped 76BNT-20BKT-4($Bi_{0.5}Li_{0.5}$)TiO_3 at room temperature and 400 kV/cm [8].

At low electric fields the current appears to be Ohmic. The Ohmic current density is given by

$$J_{Ohm} = q\mu n_0 E, \tag{4.11}$$

where

$$n_0 = N_V \exp\left(-\frac{E_A}{k_B T}\right). \tag{4.12}$$

In Eq. (4.11), μ is the free carrier mobility and n_o is the carrier concentration in thermal equilibrium (at zero field). In Eq. (4.12), N_V is the density of states in the valence band and E_A is an activation energy, being a first approximation of the energy from the shallow trap level to the conduction band. The temperature dependencies are assumed to be $\mu \sim T^{-1/2}$ and $N_V \sim T^{3/2}$, and thus $J_{Ohm} \sim T$. The energy from the Fermi level to the valence band is $E_A = E_F - E_V$, for p-type conduction. Ideally, the slope of ln*J*-ln*E* for the Ohmic region should be unity. While this was in excellent agreement for what was observed with 1-2 mol% Mn-doped films, larger slopes (1.05-1.58) obtained for the 0-0.2 mol% Mn-doped films were possibly related to an *E*-field dependence of charge relaxation dynamics. Also, with increasing amount of Mn the low-field Ohmic current increased in magnitude.

For each doping level, E_A was calculated by plotting ln(J/T) vs. $1/T$. These values were 0.204±0.028, 0.182±0.019, 0.248±0.020, and 0.330±0.016 eV for the undoped, 0.2, 1, and 2 mol% Mn films, respectively. E_A for the undoped and 0.2 mol% Mn-doped films were very similar to that previously obtained for 88BNT-8BKT-4BT, which was 0.19 eV [33]. With larger amounts of Mn-doping the trap levels become deeper, which

would lead to a lower J_{Ohm}. The greater Ohmic current of the Mn-doped films is likely due to an increase in N_V as a result of the higher concentration of acceptor dopant.

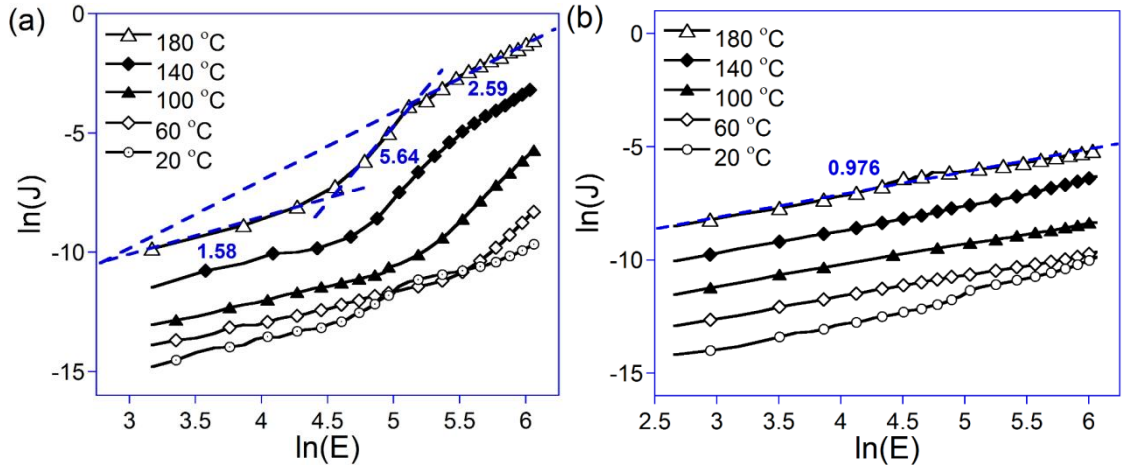

Figure 4.8 – *(a) Plots of lnJ-lnE at different temperatures for an undoped film. (b) The Ohmic region extended to beyond 400 kV/cm for the 2 mol% Mn-doped films, even at high temperature. Slopes are provided for the various segments of the plots at 180 °C. Plots are shown for negative applied bias.*

The leakage current mechanism is best described by the space charge limited current (SCLC) model. This was also the mechanism proposed for epitaxial 88BNT-8BKT-4BT by Hejazi and Safari [33]. The *J*-curves for SCLC follow the format of Fig. 4.9, which shows J_{Ohm}, the traps-limited region, J_{tr}, and the trap-free Child's law current, J_{Ch}. The SCLC model can also be partially validated by extrapolation of J_{Ch} to the intersection with J_{Ohm}, to form Lampert's triangle [34]. This occurs at a voltage,

$$V_{\Omega-Ch} = \frac{8}{9}\frac{(qd^2n_0)}{\varepsilon_s\varepsilon_0}, \qquad (4.13)$$

which is defined by the free carrier concentration, n_0, film thickness, d, and the static dielectric constant, ε_s. Lampert's triangle appears to be completed in these films, as well. Refer to the ln*J*-ln*E* plot in Fig. 4.8a (at 180 °C). At this temperature the intersection occurs at ln*E*≈2.8. Taking d=210 nm and ε_s=700, n_0 was calculated as 3.5×10^{17} cm^{-3}.

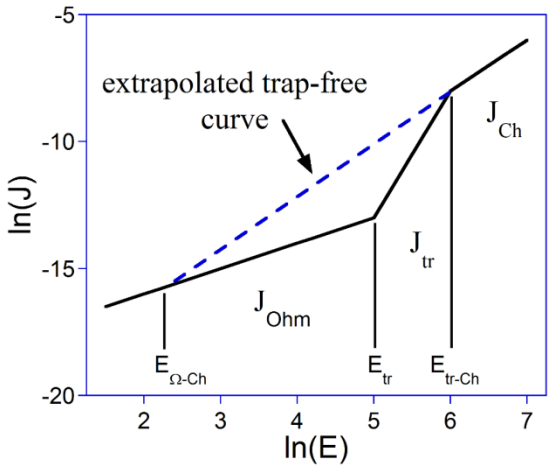

Figure 4.9 – *Diagram of SCLC for an exponential trap distribution, showing J- curves and key electric fields* [36].

The carrier transit time through the dielectric film, τ_c, becomes faster with increasing E until it becomes faster than the field-free dielectric relaxation time, τ_d, at the transition field, E_{tr} (Fig. 4.9), when the Fermi level begins to increase toward the conduction band [35]. This is also when $n>n_0$, where n is the total number of injected carriers. E_{tr} marks the end of J_{Ohm} and the beginning of the trap-filling current, J_{tr}. The trap-filling current is explained by several models, depending on the nature of the trap levels. For a single deep trap level, the plot of $\ln J_{tr}$-$\ln E$ is almost vertical, although the observed slope depends on the dielectric relaxation, and thus the soak time used during measurement [36]. Second, a lesser, and finite slope may imply a distribution of trap levels [37][38]. Third, a slope≈3 can occur from a process of double injection of $e^{/}$ and $h^{\bullet}$ [39].

From Fig. 4.8a it is seen that $\ln J_{tr}$-$\ln E$ has a slope ~5, which is far from vertical. By comparison, Hejazi and Safari found slopes in this region to decrease from 15.65 to 6.64 with temperature. The more shallow slopes seen here appear to be more consistent with the theory of Rose for distributed trap levels, and the analysis proceeds as follows [37]. Moreover, the transition between J_{Ohm} and J_{tr} is rather gradual here compared to the sharply defined E_{tr}, which was observed for the epitaxial 88BNT-8BKT-4BT deposited by PLD [33]. Oxygen vacancies, or other forms of non-stoichiometry, in the presence of A-site cation disorder are suggested as possible factors leading to a

distribution in trap energy levels. Mark and Helfrich derived an equation for J_{tr} given an exponential distribution of shallow traps [38]:

$$J_{tr} = \frac{q^{1-l}\mu N_V}{d^l}\left(\frac{\varepsilon_s l}{N_t(l+1)}\right)^l \left(\frac{2l+1}{l+1}\right)^{l+1} E^{l+1}, \qquad (4.14)$$

where

$$l = \frac{T^*}{T}. \qquad (4.15)$$

Above, T^* is a *characteristic temperature* of the trap energy distribution and N_t is the total trap concentration. Using Eq. (4.14) and the power of E dependence of J_{tr}, the characteristic trap energy, k_BT^*, was calculated to be 0.15, 0.13, and 0.071 eV for undoped, 0.2, and 1 mol% Mn films. The value of k_BT^* for the undoped film is similar to the trap level obtained by Hejazi and Safari.

The exact functional form of the trap level distribution is not known for certain. However, a qualitative comparison of the E_A determined from J_{Ohm} prior to strong injection (and a shift in the Fermi level), and k_BT^* determined from J_{tr} as the traps are becoming filled could suggest a broadening of the trap level distribution commensurate with Mn-doping. The energies thus determined for the 1 mol% Mn-doped films are lower and higher than those of the undoped films below and above the onset of strong injection, respectively. It is suggested that the presence of defect complexes (e.g. Mn_{Ti}''-$V_O^{\bullet\bullet}$), or possibly even A-site cation disorder, can broaden the trap distribution, increasing the number of free carriers accessible to k_BT in the Ohmic region. This may also account for the higher J_{Ohm} upon Mn-doping.

The *J-E* plots for all the films at 120 °C demonstrated an increasing E_{tr} with Mn-doping level (Fig. 4.10). The *J-E* plots were Ohmic for 2 mol% Mn samples and E_{tr} was not observed at all before breakdown at any temperature up to 180 °C. An increase in τ_c relative to τ_d results in an increase in E_{tr}. Also, a decrease in μ results in an increase in τ_c. Therefore, it should be expected that the Mn-doping caused a definite drop in the $e^{/}$ or $h^{\bullet}$ mobility. The slopes of the lnJ_{tr}-ln$E$ plots were 5.3, 4.8, and 3.1 for undoped and 0.2 and 1 mol% Mn films, respectively. The increasing E_{tr} and decreasing slope of J_{tr} combined to cause the reduction in the high-*E* leakage current. The trend in E_{tr}, at least, with respect to Mn doping level has previously been seen in room temperature data for Mn-doped

BNT, (K,Na)NbO_3, and $NaNbO_3$-BT films [8][9][10][13][14][40]. It can be seen from Fig. 4.8 that the behaviors persisted from room temperature up to 180 °C.

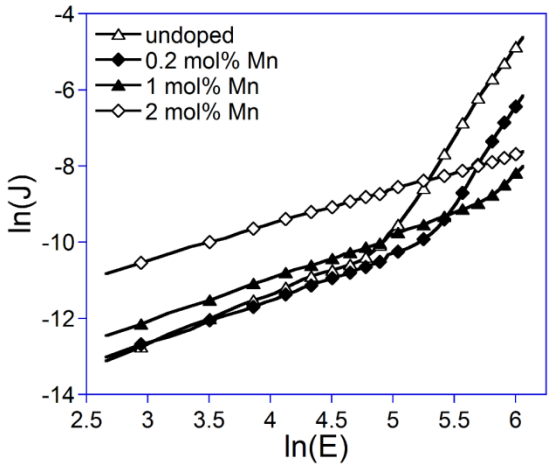

Figure 4.10 – *lnJ-lnE at 120 °C for different Mn-doping levels. The features of this comparison are the increasing Ohmic and decreasing high-E current found for Mn-doped films.*

Above $E_{tr\text{-}Ch}$, as defined by Fig. 4.9, there are more injected electrons than trapped electrons, $n>n_t>n_0$, with n_t the number of trapped electrons [37][38]. In this region the current obeys the trap-free Child's law, $J_{Ch}\sim E^2$ according to

$$J_{Ch} = \frac{9}{8}\frac{\mu\varepsilon_s}{d}E^2. \qquad (4.16)$$

Child's law current was only observed for the undoped and 0.2 mol% films, before dielectric breakdown, and then only above 120 °C. There was an apparent onset of J_{Ch} on some of the 1 mol% Mn films as J_{tr} began to taper off near 160-180 °C, but it was not consistently observed. That J_{Ch} is not always observed is not unusual since SCLC can span a wide range of measured current; often the Ohmic and transition are all that can be seen to indicate the SCLC mechanism [41][42]. However, one matter of concern was that the onset of J_{Ch} only occurred several tens of degrees after the appearance of transient currents, as shown in Fig. 4.5. It must be considered that E_{tr} or other observed quantities might show some dependence on the electrical history of the sample if defects were migrating during measurement. Still, the Child's law curve was extrapolated to the Ohmic curve, with their intersection defining $V_{\Omega\text{-}Ch}$, as in the dashed line in Fig. 4.9, to complete Lampert's triangle and calculate a reasonable value for n_0 [34].

The carrier mobility can be calculated from the intercept of $\ln J_{Ch}$-$\ln E$ plot, using Eq. (4.16). These analyses were made using the high temperature curves from 140-180 °C. The resulting mobilities decreased as 4.0×10^{-7}, 2.1×10^{-8}, and 3.2×10^{-9} $cm^2V^{-1}s^{-1}$ for undoped, 0.2, and 1 mol% Mn-doped films, respectively. These were much lower than the mobility calculated for PLD deposited 88BNT-8BKT-4BT, for which the value 5.82×10^{-3} $cm^2V^{-1}s^{-1}$ was reported [33].

It is not entirely clear why the mobility is so low in this case. Hole mobilities are thought to be much smaller than electron mobilities in ferroelectrics [43]. The dominance of hole conduction would suggest that a process like that of Eqs. (4.1-3). Another possibility is that charge trapping was incomplete for the soak times used during measurement. Mobilities in perovskite ferroelectrics can vary widely, with values from 10^{-2} $cm^2V^{-1}s^{-1}$ to 10^{-7} $cm^2V^{-1}s^{-1}$ having been reported previously for PZT thin films [44]. Still, as was noted above, the decrease in μ (or increase in τ_c) with increasing Mn concentration is consistent with the trend in E_{tr} shown in Fig. 4.10.

Although the mobility was only obtained for the low-doped films, the product μN_V was found using Eqs. (4.11-12). The values for μN_V are 1.5×10^{11}, 1.1×10^{11}, 1.1×10^{12}, and 6.0×10^{13} $V^{-1}s^{-1}cm^{-1}$ for the undoped, 0.2, 1, and 2 mol% Mn-doped films, respectively. It can be seen that the dependence is largely the same for low levels of doping but increases markedly at 1 and 2 mol% Mn. This implies a sudden and dramatic increase in either the effective density of states or the mobility when adding more significant amounts of Mn (i.e. 1-2 mol%).

Having found μN_V, the number of traps, N_t, can be determined from Eq. (14) for samples which exhibited J_{tr}, excluding the 2 mol% Mn samples, which were Ohmic at all fields [38]. The values obtained for N_t were 7.3×10^{18}, 3.4×10^{18}, and 1.8×10^{19} cm^{-3} for the undoped, 0.2 mol% Mn, and 1 mol% Mn, respectively. The slope of J_{tr} weighs heavily on the calculated result for N_t , which can certainly be affected by trapping and detrapping rates [34][42]. The values are comparable to those for N_V for the 0-1 mol% Mn films, and compare well to values reported for PZT thin films [43]. This is reasonable as the carrier concentration is likely due to the introduction of extrinsic defects. The figures are also quite a bit larger than N_t=6.97×10^{15} cm^{-3} reported by Hejazi and Safari for 88BNT-8BKT-4BT [33][45]. The relatively small change in N_t with large doping levels is also

suggestive of significant reoxidation of $V_O^{\bullet\bullet}$, again as in Eqs. (4.1-3). If the films were p-type, this suggests that the $Mn_{Ti}^{//}$ (and $Mn_{Ti}^{///}$) sites were stable and did not contribute to trapping holes. Otherwise, the SCLC would have appeared prominently in 2 mol% Mn-doped films, which was not observed.

Other conduction mechanisms, such as Schottky or Poole-Frenkel, were investigated as part of the analysis, using methods as described by Chiu [36]. None of the slopes in the low or high electric field region consistently produced realistic values for the optical dielectric constant. Furthermore, even when realistic optical dielectric constants were derived, the results were unphysical. For instance, often negative barrier heights were obtained, indicating that these were not the correct mechanisms. Hopping conduction was also ruled out due to an incorrect temperature dependence of the slopes. The leakage current gave results consistent with SCLC as reported for similar material systems [33]. Besides the general agreement of the slopes of ln*J*-ln*E* to the model, a good indication of SCLC is the completion of Lampert's triangle [34].

Mn-doping was shown to reduce the leakage current over a wide temperature range, although the low-field Ohmic current was unexpectedly higher with Mn-doping. This effect was larger than that observed in BNT-based films deposited by PLD, where the Ohmic current was hardly changed by Mn-doping [8]. Other room temperature leakage data on Mn-doped BNT-based films deposited by CSD have demonstrated a higher J_{Ohm} [9]. The difference may be due to the stoichiometry or film morphology, but the literature on leakage current in BNT-based films is still rather sparse.

4.4.2 Transient currents

As mentioned, $E_{A,ion}$ and μ_{ion} extracted for the undoped films (Fig. 4.6a) are suggestive of a modulation of the conductivity due to migration of oxygen vacancies. The transient currents were only observed for positive applied bias, as seen in Fig. 4.5, but the overall magnitude of the currents there and in Fig. 4.7a were larger for the negative bias. Together, these facts may be demonstrative of an asymmetry in the initial distribution of vacancies. The top surface of the film may have a larger concentration of $V_O^{\bullet\bullet}$ prior to application of an electric field, due to oxygen loss occurring during crystallization. The symmetry of the J-E characteristics in Fig. 4.7b and the temperature invariance of the current peak time constant for the 1 mol% Mn-doped film (Fig. 4.6b) may indicate the

strong binding of the defect complex Mn_{Ti}"-$V_O^{\bullet\bullet}$. On cooling from annealing, yet while the temperature is still high enough for significant migration, $V_O^{\bullet\bullet}$ may become bound to fixed Mn_{Ti}" centers to the effect of making the distribution of space charge spatially symmetric.

As was noted above, there was no obvious difference in the microstructures apparent from the AFM images or XRD which might have accounted for the difference in oxygen vacancy diffusion. As noted above, second phases from Mn-doping would are not expected at the concentrations used here [28]. However, in BT ceramics, doping with Mn at concentrations near 0.5-1 mol% tends to cause the grain boundaries to become enriched with the dopant [46][47]. It is reasonable to assume that oxygen vacancies may also become trapped in the grain boundaries. The *J-t* curves in Fig. 4.6b appear very similar to the model of Many and Rakavy for transient current in insulators with varying trapping time constants or free charge density [48]. For example, the former would correspond to our data as a longer trapping time constant with increasing temperature due to a decreased trapping effectiveness.

Although the stability of the high field leakage current was enhanced by doping with 2 mol% Mn-doped, there were some unexpected results at high temperature. These films would abruptly become conductive at and above 180 °C, passing currents ≈1 A/cm^2 at fields as low as 10 kV/cm (e.g. a factor of 10^7 higher than expected). The high conductivity phase was reversed after allowing the film to cool several tens of degrees. Since the contacts were Ohmic, and 10 kV/cm is a very low driving field, the higher current must be due to an increase in the volume conductivity of the film rather than increased charge injection. Current of 1 A/cm^2 was much higher than that observed during breakdown events at higher fields during normal measurements. At 2 mol% Mn the doping level is likely beyond the solubility limit and the higher current could be due to conductive pathways forming at the grain boundaries. The role Mn plays in modifying leakage current characteristics in BNT-BKT thin films is thus complicated. Mn-doping limits oxygen vacancy migration and reduced the high-*E* leakage current but, as mentioned above, the Mn_{Ti}"-$V_O^{\bullet\bullet}$ complex may become unbound at high temperatures.

The transient current also affects the determination of the steady state leakage mechanism. A Child's law region, where the traps are filled and space charge limits

charge injection, did not appear until high temperatures and was not consistent for 1 mol% Mn. Cumulative electric field sweeps could potentially affect the onset of E_{tr}, the slope J_{tr}, or J_{Ch} at temperatures where oxygen vacancies become mobile. Defect migration might cause the *J-E* plots to deviate from theoretical steady state leakage behavior, even at relatively short soak times where the current relaxation would still be significant. Due to the long measurement times required for the transient currents, the current generally recovered to its initially low value only after a delay of several minutes upon removal and subsequent reapplication of the field. However, a generally steady-state current density did appear after the current peak (Fig. 4.6). It is suggested that the *J-E* characteristics could be obtained and compared for both the short soak times, represented by Figs. 4.7-8, and at much longer times after the transient current peak.

4.4.3 NDR and PTCR

There have been previous reports showing NDR-like *J-E* data from BNT-based thin films including BNT-BKT-$(Bi_{0.5}Li_{0.5})TiO_3$ [8][49]. In that case, NDR appeared as a decrease in current just past an apparently Ohmic region in oxygen-poor samples (i.e. films deposited by PLD under low oxygen pressure).

In the temperature range 25-60 °C a knee occurred in the leakage current in three layer films, as in Fig. 4.7a. The knee gradually diminished with temperature and also with addition of Mn. When five and seven layer films were tested, the same region of the *J-E* plot actually displayed a negative slope, rather than a knee. The NDR in those thicker films was prevalent over a wide range of temperatures and electric fields, which prevented a prototypical analysis of the leakage current mechanism. A similar knee has been seen in by Watanabe, *et al*. in SBT [16]. In some leakage measurements the plateau region of the knee actually exhibited a NDR, i.e. current decreasing with increasing electric field.

Since the PTCR and NDR were observed over the same temperature range it is reasonable to consider the model of Dawber and Scott, in which PTCR and NDR are modeled as different aspects of the same phenomena [45]. It has been used to explain the PTCR/NDR in SBT, BT and $(Pb(Fe_{0.67}W_{0.33})O_3)_{0.2}$-$(Pb(Zr_{0.53}Ti_{0.47}O_3)_{0.8}$ thin films [15][18]. It is also somewhat qualitative, as several of the parameters are difficult to

ascertain directly. There is an assumption of Schottky injection and diffusion-limited current at low fields. At high fields the current is limited by the Schottky contact according to Simmons reformulation [50]. In the model, the current is given by

$$J = q\mu N_D E_0 \exp\left[-\frac{q}{k_B T}\left(\phi_b - \frac{qN_D w^2}{2\varepsilon_r\varepsilon_0} + \frac{\varepsilon_r\varepsilon_0}{2qN_D}E_0^2\right)\right], \qquad (17)$$

where E_o is the electric field in the space-charge-free region of the film (which depends on the film polarization state), $N_D \approx N_t$ is the number of active defects, and φ_b is the injection barrier height. The model is highly sensitive to the depletion width, w, of the films and is also likely sensitive to the space charge distribution itself. The model is highly parameterized thus some assumptions must be made. In order to achieve physically appropriate parameters to fit the equation there must be some accounting of the depletion region, which generally changes with temperature. The lack of a dielectric relaxation term and unpredictable dependence on electric field and temperature cycling mean that the model is still somewhat qualitative [15]. When we attempted use Eq. (4.17) to model the knee in our films (Fig. 4.11) it was necessary to shift the E-axis to the end of the Ohmic region, by an amount that became smaller with thicker films. The model does not predict an initial Ohmic region at low fields, which is what was observed in this work.

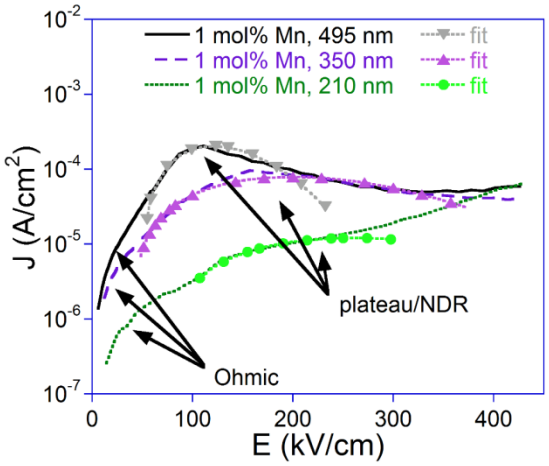

Figure 4.11 – *Fit of the low temperature knee in 1 mol% Mn-doped films to the model of Dawber and Scott.*

In bulk BT, a normal ferroelectric, the PTCR effect has been shown to be due to a double Schottky barrier forming at grain boundaries above the Curie temperature [51]. Below the Curie temperature, spontaneous polarization effectively wipes out the barrier

and the current is higher. In these films, the PTCR and NDR were only observed over a limited range, 25 °C to 60 °C. Further data collection at longer times and lower temperatures is required to demonstrate whether this is true NDR or whether this is an artifact of the short soak/measurement times (< 1 s). For example, although first observing NDR in PZT thin films it was ultimately determined this was caused by a an onset of rapidity in the dielectric relaxation currents [19]. It should also be noted, in connection to the *J-E* characteristics, that Lampert found an expression for double injection of holes and electrons which could give a region of trap-limited SCLC with $J_{tr} \sim E^3$. Interestingly, this also corresponded to a NDR region beginning after the Ohmic region. While our films show $J_{tr} \sim E^{l+1}$ with l+1 as high as 6.5, such high slopes of J_{tr} associated with SCLC did not occur below 60 °C, and so in the low temperature region this is yet another mechanism to consider [39].

4.5 Conclusions

Mn-doping was studied as a function of Mn-dopant concentration and temperature in 80BNT-20BKT thin films. The behavior of E_{tr} and the corroboration of trap levels by previous works, the eventual onset of Child's law-like current at high temperatures, and the absence of another conduction mechanism which fits the data strongly suggest SCLC. Transient oxygen vacancy vacancy migration was observed and a marked difference was found between undoped and Mn-doped thin films. The onset temperature of Child's law coincided with that of oxygen vacancy migration suggesting that the leakage current behavior of polycrystalline BNT-BKT thin films is dependent not only on the exact stoichiometry of the films but also on the defect distribution through the film thickness, which may change during measurement at high temperatures. The time dependence of the leakage current indicates that BNT-BKT thin films cannot automatically be assumed to be in the steady state at temperatures at least as low as 120 °C, even after allowing soak times for the dielectric relaxation.

Acknowledgements

The authors acknowledge support of this work from the National Science Foundation under CAREER Grant No. DMR 115170.

References

[1] K. Yoshii, Y. Hiruma, H. Nagata, and T. Takenaka, "Lead-free piezoelectric ceramics," *Jpn. J. Appl. Phys.*, vol. 45, no. 5B, pp. 4493–4496, 2006.

[2] A. Sasaki, T. Chiba, Y. Mamiya, and E. Otsuki, "Dielectric and piezoelectric properties of $(Bi_{0.5}Na_{0.5})TiO_3$–$(Bi_{0.5}K_{0.5})TiO_3$ Systems," *Jpn. J. Appl. Phys.*, vol. 38, p. 5564, 1999.

[3] J. Rödel, W. Jo, K. T. P. Seifert, E. M. Anton, T. Granzow, and D. Damjanovic, "Perspective on the development of lead-free piezoceramics," *J. Am. Ceram. Soc.*, vol. 92, no. 6, pp. 1153–1177, 2009.

[4] S. Ikegami, I. Ueda, and T. Nagata, "Electromechanical properties of $PbTiO_3$ ceramics containing La and Mn," *J. Acoust. Soc. Am.*, vol. 50, no. 4A, p. 1060, 1971.

[5] K. Okazaki and H. Igarashi, "Processing-property relations in ceramic dielectric capacitors," *Ferroelectrics*, vol. 27, no. 1, pp. 263–268, 1980.

[6] W. Hofman, S. Hoffmann, and R. Waser, "Dopant influence on dielectric losses, leakage behaviour, and resistance degradation of $SrTiO_3$ thin films," *Thin Solid Films*, vol. 305, no. 1–2, pp. 66–73, 1997.

[7] K. H. Ahn, S. Baik, and S. S. Kim, "Significant suppression of leakage current in $(Ba,Sr)TiO_3$ thin films by Ni or Mn doping," *J. Appl. Phys.*, vol. 92, no. 5, p. 2651, 2002.

[8] M. M. Hejazi, E. Taghaddos, and A. Safari, "Reduced leakage current and enhanced ferroelectric properties in Mn-doped $Bi_{0.5}Na_{0.5}TiO_3$-based thin films," *J. Mater. Sci.*, vol. 48, no. 9, pp. 3511–3516, 2013.

[9] W. Li, H. Zeng, J. Hao, and J. Zhai, "Enhanced dielectric and piezoelectric properties of Mn doped $(Bi_{0.5}Na_{0.5})TiO_3$–$(Bi_{0.5}K_{0.5})TiO_3$–$SrTiO_3$ thin films," *J. Alloys Compd.*, vol. 580, pp. 157–161, 2013.

[10] D. Y. Wang, N. Y. Chan, S. Li, S. H. Choy, H. Y. Tian, and H. L. W. Chan, "Enhanced ferroelectric and piezoelectric properties in doped lead-free $(Bi_{0.5}Na_{0.5})_{0.94}Ba_{0.06}TiO_3$ thin films," *Appl. Phys. Lett.*, vol. 97, no. 21, p. 212901, 2010.

[11] D. Smyth, M. Harmer, Materials Research Center, and Lehigh University, "Long term stability in thin film ferroelectric memories.," 1995.

[12] C. W. Ahn, S. Y. Lee, H. J. Lee, A. Ullah, J. S. Bae, E. D. Jeong, J. S. Choi, B. H. Park, and I. W. Kim, "The effect of K and Na excess on the ferroelectric and piezoelectric properties of $K_{0.5}Na_{0.5}NbO_3$ thin films," *J. Phys. D. Appl. Phys.*, vol. 42, no. 21, p. 215304, 2009.

[13] Y. Hamazaki, W. Sakamoto, M. Moriya, and T. Yogo, "Effects of $BaTiO_3$ content and Mn doping on ferroelectric properties of $NaNbO_3$–$BaTiO_3$ thin films prepared by chemical solution deposition," *Jpn. J. Appl. Phys.*, vol. 48, no. 9, p. 09KA08, 2009.

[14] M. Abazari, E. K. Akdoğan, and A. Safari, "Effect of manganese doping on remnant polarization and leakage current in $(K_{0.44},Na_{0.52},Li_{0.04})(Nb_{0.84},Ta_{0.10},Sb_{0.06})O_3$ epitaxial thin films on $SrTiO_3$," *Appl. Phys. Lett.*, vol. 92, no. 21, p. 212903, 2008.

[15] J. F. Scott, F. D. Morrison, M. Miyake, P. Zubko, X. Lou, V. M. Kugler, S. Rios, M. Zhang, T. Tatsuta, O. Tsuji, and T. J. Leedham, "Recent materials characterizations of [2D] and [3D] thin film ferroelectric structures," *J. Am. Ceram. Soc.*, vol. 88, no. 7, pp. 1691–1701, 2005.

[16] K. Watanabe, a. J. Hartmann, R. N. Lamb, and J. F. Scott, "Electronic characteristics of the $SrBi_2Ta_2O_9$–Pt junction," *J. Appl. Phys.*, vol. 84, no. 4, p. 2170, 1998.

[17] A. Mukherjee, P. Victor, J. Parui, and S. B. Krupanidhi, "Leakage current behavior in pulsed laser deposited $Ba(Zr_{0.05}Ti_{0.95})O_3$ thin films," *J. Appl. Phys.*, vol. 101, no. 3, p. 034106, 2007.

[18] A. Kumar, R. S. Katiyar, and J. F. Scott, "Positive temperature coefficient of resistivity and negative differential resistivity in lead iron tunstate-lead zirconate titate," *Appl. Phys. Lett.*, vol. 94, no. 21, p. 212903, 2009.

[19] J. F. Scott, "Negative differential resistivity in ferroelectric thin-film current-voltage relationships," *Integr. Ferroelectr.*, vol. 4, no. 1, pp. 85–92, 1994.

[20] Y. Podgorny, A. Sigov, A. Vishnevskiy, and K. Vorotilov, "Simulation of negative differential resistivity in thin," *Ferroelectrics*, vol. 465, pp. 28–35, 2014.

[21] S. Zafar, R. E. Jones, B. Jiang, B. White, P. Chu, D. Taylor, and S. Gillespie, "Oxygen vacancy mobility determined from current measurements in thin $Ba_{0.5}Sr_{0.5}TiO_3$ films," *Appl. Phys. Lett.*, vol. 73, no. 2, pp. 175–177, 1998.

[22] R. Meyer, R. Liedtke, and R. Waser, "Oxygen vacancy migration and time-dependent leakage current behavior of $Ba_{0.3}Sr_{0.7}TiO_3$ thin films," *Appl. Phys. Lett.*, vol. 86, no. 11, pp. 1–3, 2005.

[23] R. Merkle and J. Maier, "Defect association in acceptor-doped $SrTiO_3$: case study for $Fe_{Ti}^{//}V_O^{\cdot\cdot}$ and $Mn_{Ti}^{//}V_O^{\cdot\cdot}$" *Phys. Chem. Chem. Phys.*, vol. 5, no. 11, pp. 2297–2303, 2003.

[24] Y. H. Jeon, E. A. Patterson, D. P. Cann, P. Mardilovich, W. Stickel, and B. J. Gibbons, "Large piezoresponse and ferroelectric properties of $(Bi_{0.5}Na_{0.5})$ TiO_3–$(Bi_{0.5}K_{0.5})TiO_3$–$Bi(Mg_{0.5}Ti_{0.5})O_3$ thin films prepared by chemical solution deposition," *J. Am. Ceram. Soc.*, vol. 96, no. 7, pp. 2172–2178, 2013.

[25] Y. H. Jeon, E. A. Patterson, D. P. Cann, and B. J. Gibbons, "Dielectric and ferroelectric properties of $(Bi_{0.5}Na_{0.5})TiO_3$–$(Bi_{0.5}K_{0.5})TiO_3$–$BaTiO_3$ thin films deposited via chemical solution deposition," *Mater. Lett.*, vol. 106, pp. 63–66, 2013.

[26] C. J. Kim, D. S. Yoon, J. S. Lee, C. G. Choi, and K. No, "Effects of substrate and bottom electrodes on the phase formation of lead zirconate titanate thin films prepared by the sol-gel method," *Jpn. J. Appl. Phys.*, vol. 33, p. 2675, 1994.

[27] M. Kumar and K. L. Yadav, "Rapid liquid phase sintered Mn doped $BiFeO_3$ ceramics with enhanced polarization and weak magnetization," *Appl. Phys. Lett.*, vol. 91, no. 24, pp. 89–92, 2007.

[28] S. Stoupin, S. Chattopadhyay, T. Bolin, and C. U. Segre, "High concentration manganese doping of ferroelectric $PbTiO_3$," *Solid State Commun.*, vol. 144, pp. 46–49, 2007.

[29] Y. S. Sung and M. H. Kim, "Effects of B-site Donor and Acceptor Doping in Pb-free $(Bi_{0.5}Na_{0.5})TiO_3$ Ceramics," in *Ferroelectrics*, I. Coondoo, Ed. InTech, 2010, p. 217.

[30] L. Wu, D.-Q. Xiao, D.-M. Lin, J.-G. Zhu, and P. Yu, “Synthesis and properties of $[Bi_{0.5}(Na_{1-x}Ag_x)_{0.5}]_{1-y}Ba_yTiO_3$ piezoelectric ceramics,” *Jpn. J. Appl. Phys.*, vol. 44, no. 12, pp. 8515–8518, 2005.
[31] P. C. Joshi and S. B. Desu, “Structural and electrical studies on rapid thermally processed ferroelectric $Bi_4Ti_3O_{12}$ thin films by metallo-organic solution deposition,” *J. Appl. Phys.*, vol. 80, p. 2349, 1996.
[32] F. E. Kamel, P. Gonon, L. Ortega, F. Jomni, and B. Yangui, “Space charge limited transient currents and oxygen vacancy mobility in amorphous $BaTiO_3$ thin films,” *J. Appl. Phys.*, vol. 99, no. 9, p. 094107, 2006.
[33] M. M. Hejazi and A. Safari, “Temperature-dependent leakage current behavior of epitaxial $Bi_{0.5}Na_{0.5}TiO_3$-based thin films made by pulsed laser deposition,” *J. Appl. Phys.*, vol. 110, no. 10, p. 103710, 2011.
[34] M. A. Lampert, “Simplified theory of space-charge-limited currents in an insulator with traps,” *Phys. Rev.*, vol. 103, no. 6, pp. 1648–1656, 1956.
[35] R. H. Parmenter and W. Ruppel, “Two-carrier space-charge-limited current in a trap-free insulator,” *J. Appl. Phys.*, vol. 30, no. 10, pp. 1548–1558, 1959.
[36] F. Chiu, “A review on conduction mechanisms in dielectric films,” *Adv. Mater. Sci. Eng.*, p. 578168, 2014.
[37] A. Rose, “Space-charge-limited currents in solids,” *Phys. Rev.*, vol. 97, no. 6, pp. 1538–1544, 1955.
[38] P. Mark and W. Helfrich, “Space-charge-limited currents in organic crystals,” *J. Appl. Phys.*, vol. 33, no. 1, pp. 205–215, 1962.
[39] M. A. Lampert, “Double injection in insulators,” *Phys. Rev.*, vol. 125, no. 1, pp. 126–141, 1962.
[40] T. Matsuda, W. Sakamoto, B. Lee, T. Iijima, J. Kumagai, M. Moriya, and T. Yogo, “Electrical properties of lead-free ferroelectric Mn-doped $K_{0.5}Na_{0.5}NbO_3$–$CaZrO_3$ thin films prepared by chemical solution deposition,” *Jpn. J. Appl. Phys.*, vol. 51, p. 09LA03, 2012.
[41] X. Tang, J. Wang, X. Wang, and H. L. Chan, “Preparation and electrical properties of highly (111)-oriented $(Na_{0.5}Bi_{0.5})TiO_3$ thin films by a sol−gel process,” *Chem. Mater.*, vol. 16, no. 25, pp. 5293–5296, 2004.
[42] M. A. Lampert and P. Mark, *Current injection in solids*. New York: Academic Press, 1970.
[43] L. Pintilie, V. Stancu, L. Trupina, and I. Pintilie, “Ferroelectric Schottky diode behavior from a $SrRuO_3$-$Pb(Zr_{0.2}Ti_{0.8})O_3$-Ta structure,” *Phys. Rev. B*, vol. 82, no. 8, pp. 1–8, 2010.
[44] L. Pintilie, I. Vrejoiu, D. Hesse, G. LeRhun, and M. Alexe, “Ferroelectric polarization-leakage current relation in high quality epitaxial $Pb(Zr,Ti)O_3$ films,” *Phys. Rev. B*, vol. 75, no. 10, p. 104103, 2007.
[45] M. Dawber and J. F. Scott, “Negative differential resistivity and positive temperature coefficient of resistivity effect in the diffusion limited current of ferroelectric thin film capacitors,” *J. Phys. Condens. Matter*, vol. 515, pp. L515–L521, 2004.
[46] H. Natsui, T. Shibahara, and O. Kido, “Effect of manganese and vanadium valences for the reliability of $BaTiO_3$-based MLCCs,” *Int. Symp. Appl. Ferroelectr.*, pp. 1–4, 2011.

[47] H. Gong, X. Wang, S. Zhang, Z. Tian, and L. Li, "Electrical and reliability characteristics of Mn-doped nano $BaTiO_3$-based ceramics for ultrathin multilayer ceramic capacitor application," *J. Appl. Phys.*, vol. 112, no. 11, p. 114119, 2012.
[48] A. Many and G. Rakavy, "Theory of transient space-charge-limited currents in solids in the presence of trapping," *Phys. Rev.*, vol. 126, no. 6, pp. 1980–1988, 1962.
[49] H. Borkar, V. N. Singh, B. P. Singh, M. Tomar, V. Gupta, and A. Kumar, "Room temperature lead-free relaxor–antiferroelectric electroceramics for energy storage applications," *RSC Adv.*, vol. 4, no. 44, p. 22840, 2014.
[50] J. G. Simmons, "Richardson-Schottky effect in solids," *Phys. Rev. Lett.*, vol. 15, no. 25, pp. 967–968, 1965.
[51] N. Kataoka, K. Hayashi, T. Yamamoto, Y. Sugawara, Y. Ikuhara, and T. Sakuma, "Direct observation of the double Schottky barrier in niobium-doped barium titanate by the charge-collection current method," *J. Am. Ceram. Soc.*, vol. 81, no. 7, pp. 1961–1963, 1998.

5. Leakage Current and Oxygen Vacancy Migration in (100-*x*)($Bi_{0.5}Na_{0.5}$)TiO_3-*x*($Bi_{0.5}K_{0.5}$)TiO_3 Thin Films

5.1 Introduction

Solid solutions based on the ferroelectric perovskite $Bi_{0.5}Na_{0.5}TiO_3$ (BNT) and $Bi_{0.5}K_{0.5}TiO_3$ (BKT) are good candidates to someday replace current Pb-based ferroelectric and piezoelectric devices. This goal is to bring the piezoceramics industry into compliance with the Restrictions on Hazardous Substances (RoHS) guidelines, which seek to limit Pb in consumer devices. Currently, our understanding of the relevant parameters necessary for robust processing and characterization of these materials is not as developed as for current state-of-the-art $BaTiO_3$ and Pb-based materials [1][2][3]. This is particularly relevant in the case of minimizing the leakage current in thin films. To our knowledge, for BNT-based films there have been only two reports of the temperature variation of the current density-electric field (*J-E*) characteristics, which calls for an in-depth analysis if these materials will be used in device applications [4][5].

Previous work has detailed the region of improved properties of (100-*x*)BNT-*x*BKT solid solutions in both the bulk and thin film embodiments [6]. Yet none have systematically investigated the leakage current properties of those films as a function of *x* (the Na/K ratio). As Na and K are volatile they are expected to contribute to many types of defects in the film, and thus exert a great effect on the leakage current.

In order to realize the widest range of applications, BNT-BKT-based materials must be optimized through the use of ternary systems and dopants, as has been demonstrated in Pb-based materials [7][8]. Most ternary systems will have regions of enhanced dielectric, ferroelectric and piezoelectric properties with different Na/K ratios than the simple binary system. Take, for example, BNT-BKT-$BiNi_{0.5}Ti_{0.5}O_3$ and BNT-BKT-$BaTiO_3$ [9][10]. Both material systems are currently being investigated for improved electromechanical properties at a Na/K stoichiometry optimized to nearly 50 percent of the A-site. And yet, both have very different Na/K ratios which may be one

of the most important factors determining the leakage current in BNT-BKT thin films. Therefore, ternary systems which have enhanced properties near specific Na/K ratios should be explored for leakage current optimization.

In addition to ternary systems, there is the possibility to use rhombohedral/tetragonal composition heterostructures to form a structure with the overall composition of the morphotropic phase boundary (MPB) but with optimized properties. Such techniques were extensively explored in the PZT system, but very few if any studies have explored a similar strategy in the BNT-BKT system which is also host to rhombohedral and tetragonal ferroelectric phases [11]. This is yet another reason for which to study and model the leakage current in the binary system.

The dielectric relaxation and steady-state leakage currents have also been shown to be affected by the oxygen vacancy, $V_O^{\bullet\bullet}$, concentration and distribution [12][13][14]. Bulk BNT and other Bi-based ceramics have been widely reported as being excellent oxygen ion conductors [15][16][17][18]. Despite this interest in bulk ceramics, this topic has only just begun to be explored in BNT-BKT thin films [5].

The $V_O^{\bullet\bullet}$ migration can be modeled by analyzing peaks in the dc current density-time (*J-t*) plots [19]. The peak position is a function of temperature and this relationship was used to calculate an ionic mobility (μ_{ion}) and activation energy ($E_{A,ion}$). Later, the subject was revisited and a model was developed to explain the peak position as being due to a modulation of the electronic conductivity due to redistribution of $V_O^{\bullet\bullet}$ [12]. The electron mobility is many orders of magnitude higher than the μ_{ion}, so that a true ionic current could not account for the observed current peak. The concentration of $V_O^{\bullet\bullet}$ is known to have a significant impact on the ferroelectric and piezoelectric fatigue properties and thus the migration of $V_O^{\bullet\bullet}$ under a dc field is highly relevant.

We report on a strong relationship between the Na/K ratio and both the leakage current and $V_O^{\bullet\bullet}$ migration in BNT-BKT thin films. The results have implications for the optimization of leakage current, fatigue, and resistance degradation. They may also be relevant to the search for BNT-BKT-based ternary systems where low leakage current is a priority.

5.2 Experimental

Bismuth (III) acetate (99.9999%, Alpha Aesar) was dissolved in propionic acid. Sodium (I) acetate trihydrate (99%, Macron) and potassium (I) acetate (99%, Macron) were dissolved in methanol. Optimized molar excesses of 8 mol% Bi and 16 mol% Na and K were used to compensate for the volatility of the cations during crystallization. Titanium isopropoxide was stabilized by mixing with propionic acid and acetic acid, in an atmosphere controlled glove box. The bismuth was added to the Ti solution first and stirred for 1 hr, before adding the Na and K solution. The resulting solution was approximately 0.5 mol/L. It was spin-cast on sputtered platinized silicon substrates (U.S. Army Research Lab) at 3000 rpm for 30 s. Each layer was pyrolyzed at 325 °C for 4 min and crystallized at 700 °C for 10 min in air. Platinum top electrodes were deposited by dc magnetron sputtering to complete the parallel plate capacitor structure. The capacitor stacks were then annealed one last time at 400 °C for 20 min in air.

Thicknesses of the films was found by using variable angle spectroscopic ellipsometry (J.A. Woollam). Phase purity was determined by X-ray diffraction (XRD) using a Bruker AXS D8 Discover. Polarization hysteresis and *J-E* characteristics were measured by a Radiant RT66B. The voltage profile for the *J-E* measurement was a stepped pulse, with each voltage measured for a total (soak+measure) of 1 s. Transient current peaks were measured using a Keithley 236 source measure unit (SMU) using the following pattern of applied bias - the sample was set using a +4 V bias applied for 800 s, followed by application of a −4 V bias during which the transient current measurement was made. This was done in order to maximize the change in conduction, and thus transient current peak clarity.

5.3 Results and discussion

Four compositions were studied in the (100-*x*)BNT-*x*BKT system including *x*=10 (90/10), *x*=20 (80/20), *x*=30 (70/30), and *x*=40 (60/40). Following spin-coating and crystallization of six layers, the 425 nm thick films were all determined to be phase pure within the detection limits of laboratory scale XRD. There were several distinguishing

features of the XRD patterns, shown in Fig. 5.1a, which reveal some expected variation in the lattice parameter and some unexpected texturing. There was a marked increase in the intensity of the (h00) reflections on moving from the more tetragonal 60/40 compositions to the more rhombohedral 90/10 compositions (Fig. 5.1b). For instance, the ratio of integrated intensities (100)/(101) of the 60/40 film increased over 15 times relative to the same of the 80/20 film, indicating some crystallographic texturing. The values are summarized in Table 5.1. Lattice constants also increased consistently with decreasing K content, as has been previously reported for the BNT-BKT system [6].

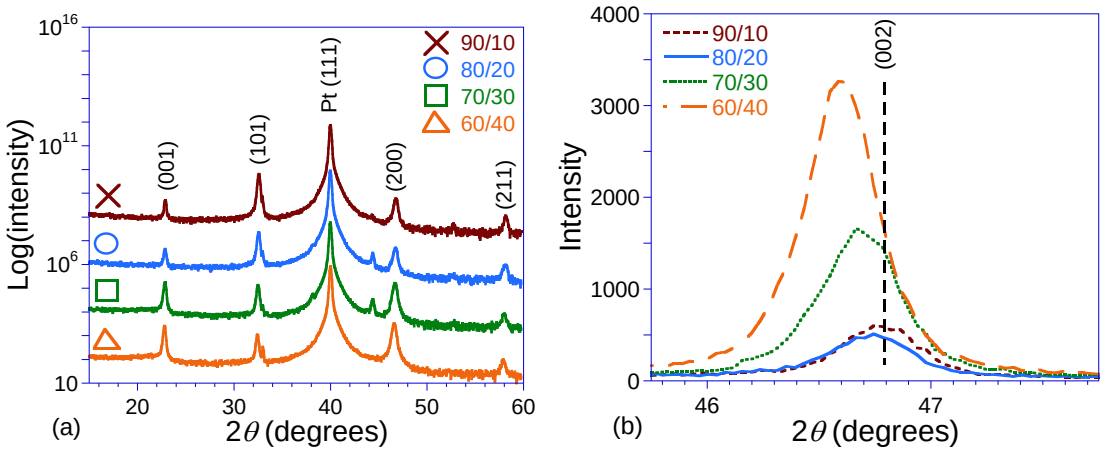

Figure 5.1 – *(a) Full x-ray diffraction patterns of the BNKT-based thin films on Pt/TiO$_x$/SiO$_2$/Si substrates. (b) Magnification of the (200) peak.*

The topography as measured by atomic force microscopy (AFM, Asylum Research MFP-3D) is shown in Fig. 5.2. Grain sizes appeared to be larger at higher Na/K ratio. Root-mean square roughness decreased with the Na/K ratio (Table 5.1). Surface roughness is commonly linked to grain size [20][21][22]. This is indicative of greater crystallite nucleation rates in the 60/40 films.

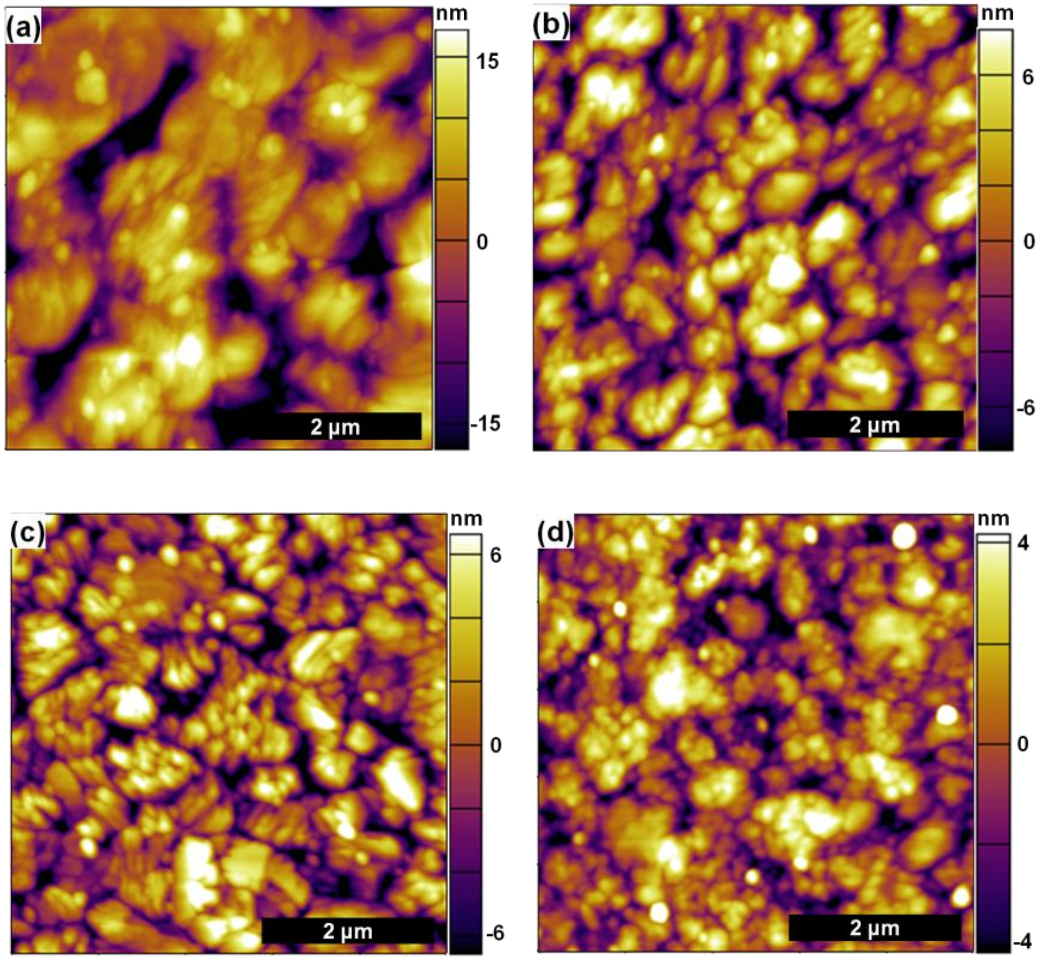

Figure 5.2 – *AFM images for (a) 90/10, (b) 80/20, (c) 70/30, and (d) 60/40 films.*

Bipolar leakage current measurements as a function of temperature made on 80/20 films using positive/negative electric field, *E*, are shown in Fig. 5.3a. By convention, voltage was applied to the top electrode, with the bottom electrode as ground. There was asymmetry in the *J-E* curves with respect to the bias polarity. For *–E*, the current density (*J*) was greater for large *E*, and breakdown often occurred at lower fields. Subsequent measurements were made primarily at *+E* in order to avoid damage to the devices. For 80/20 films, *J* was greater low temperatures (*T*), decreasing to a minimum ~80 °C, where it began to increase again. This did not occur in the data from 70/30 films, displayed in Fig. 5.3b. The leakage current was also highly asymmetric in the 70/30 films, much more so than the 80/20 films.

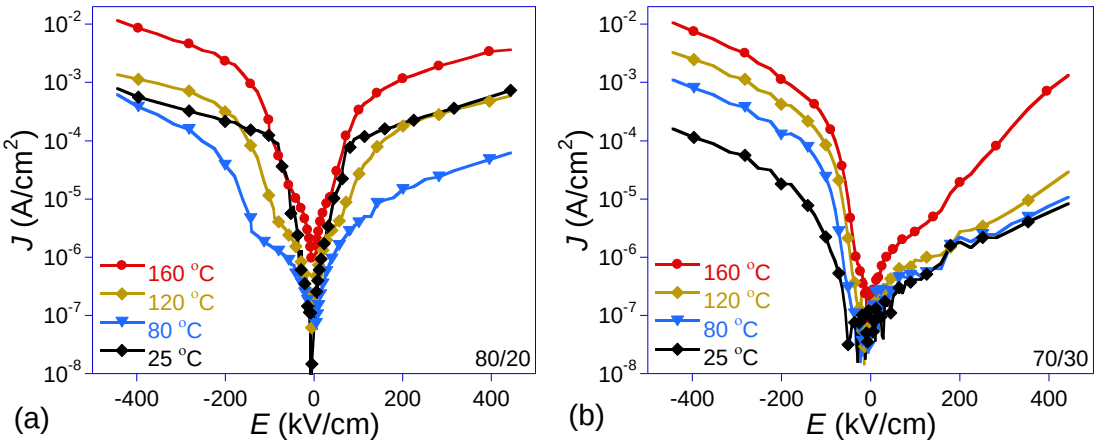

Figure 5.3 – *Leakage current was asymmetric in capacitors made from (a) 80/20 films but not from (b) 70/30 films.*

Leakage current densities were lower as the composition shifted to higher amounts of BKT, as can be seen from the ln*J*-ln*E* plots which show the current at +*E* applied, at 40 °C (Fig. 5.4a) and 160 °C (Fig. 5.4b). In all films, conduction could be well explained by the space charge-limited current (SCLC) model [4][23]. The characteristic leakage current profile of SCLC begins in all films with a region obeying Ohm's law, $J_{Ohm} \propto E$. This is followed by a transition region, $J_{tr} \propto E^{l+1}$ (l>3) marked by a transition electric field, E_{tr}, taken to be the onset of strong injection [23]. After the J_{tr}, the defect traps are mostly filled and the current is dominated by space charge effects and Child's law takes hold, $J_{Ch} \propto E^{(2+\gamma)}$. The power dependence can be explained by double injection of electrons and holes with varying degrees of carrier recombination [24][25][26][27]. The films shown here had $\alpha \approx 0$. The particular instances in which α may change are still being investigated.

Despite the overall reasonable fit to the SCLC model, it can be seen by comparison with Fig. 5.3 that the +*E* current is significantly lower than at –*E* applied for the 70/30 films. We also were not able to see the Child's law current in this data. For these reasons, the +*E* current for the 70/30 films was also fit to the Schottky model.

$$J = A^* T^2 \exp\left[\frac{-q\left(\phi_B - \sqrt{qE/4\pi\varepsilon_i\varepsilon_0}\right)}{k_B T}\right] \qquad (5.1)$$

Equation (5.1) contains several constants including the Richardson constant, A^*, the electric charge, q, Boltzmann's constant, k_B, and the permittivity of free space, ε_0. There are also several fitting parameters, such as the Schottky barrier height (ϕ_B) and the optical dielectric constant (ε_i). By plotting $\ln(J/T^2)$ versus $E^{1/2}$, values were found for ε_i in the range 1.2 ~3.2, which are below typical values for perovskite materials (provide actual literature values, if possible) [28]. The intercept of that fit, given by $-q\phi_B/k_BT$, was plotted against 1/T and the slope was used to calculate ϕ_B =0.061 ±0.053 eV (typical values are 0.5 ~ 1.5 eV). This makes the Schottky model less likely than a SCLC which simply did not reach J_{Ch}.

In the 90/10 and 80/20 compositions, J_{Ohm} was higher than in the 70/30 and 60/40 films. The regime of J_{Ohm} was also greater in the 70/30 and 60/40 films, and thus E_{tr} was larger, further increasing the disparity between the compositions at intermediate fields.

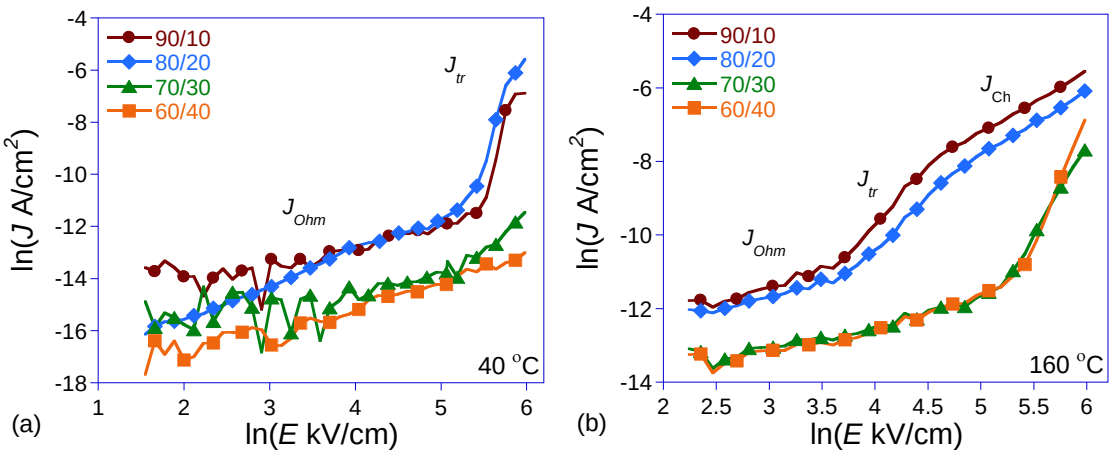

Figure 5.4 – *Leakage current at (a) 40 °C and (b) 160 °C for the 90/10, 80/20, 70/30 and 60/40 films.*

The current-time (*J-t*) relationship was measured for all films. Transient current peaks were observed, shown in Fig. 5.5, with ever shorter time constants at higher Na/K ratio.

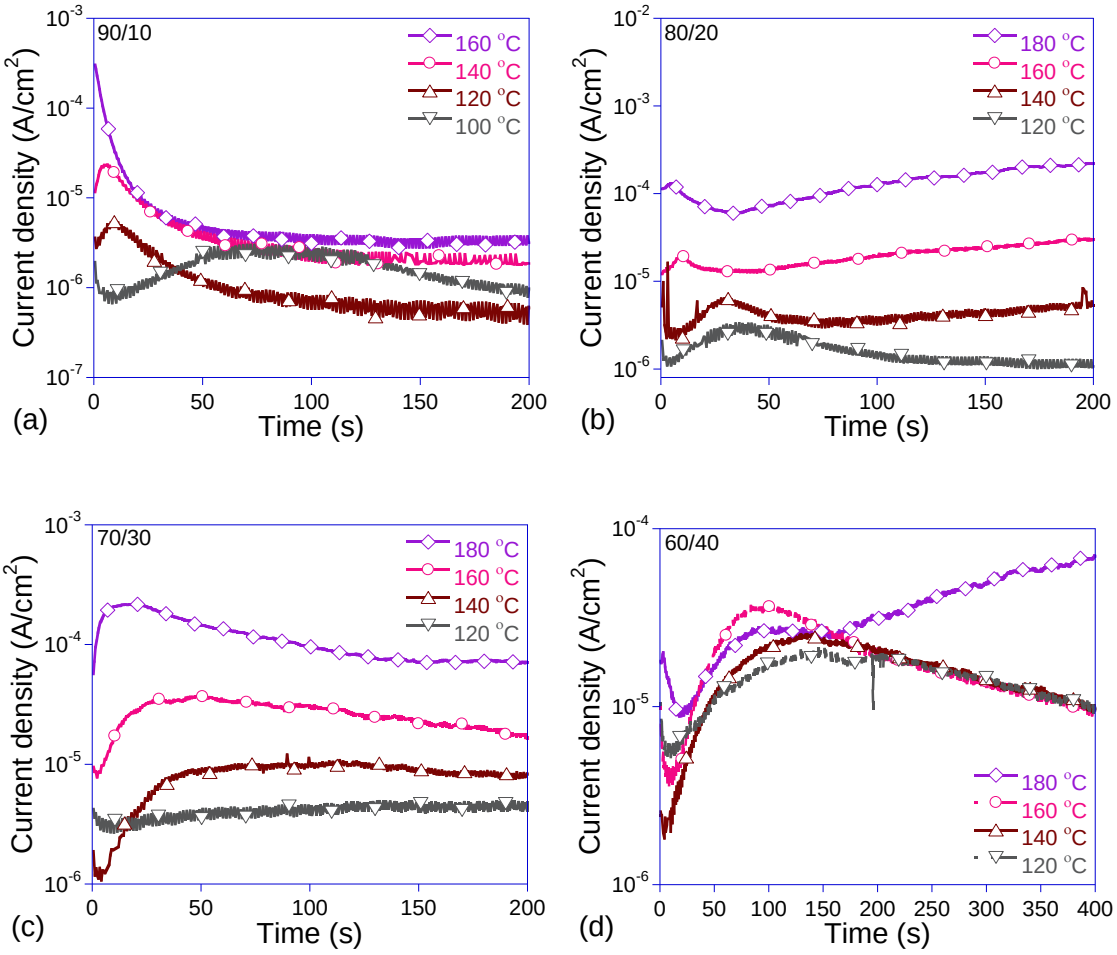

Figure 5.5 – *Transient current peaks for (a) 90/10, (b) 80/20, (c) 70/30, and (d) 60/40 films. The peaks became more diffuse and arrived at later times as the ratio Na/K decreased. Note that (d) is plotted on a longer time axis.*

Redistribution of charged defects in the presence of an electric field can cause a modulation of the electronic current, resulting in a peak in the *J-t* plot [12]. Zafar, *et al.* prescribed the equations describing the diffusion coefficient and ionic mobility to the study of such current peaks [19]. First, μ_{ion} is determined from

$$\tau = \frac{7.8\text{x}10^{-4}d}{\mu_{ion}E}, \qquad (5.2)$$

where τ is the peak time constant given in seconds, d is the film thickness in units of cm, and E is the electric field in units of kV/cm. Separately, the thermally activated diffusion coefficient, D_{ion}, is related to $E_{A,ion}$ by

$$D_{ion} = \gamma \exp\left(-\frac{E_{A,ion}}{k_B T}\right). \quad (5.3)$$

In Eq. (5.3), γ is a constant giving the maximum diffusion coefficient (at infinite temperature). Both Eqs. 1 and 2 are related via the Einstein relation,

$$k_B T \mu_{ion} = q D_{ion}. \quad (5.4)$$

which, upon substitution of Eq. (5.3) and some rearrangement becomes

$$T\mu_{ion} = \left(\frac{\gamma q}{k_B}\right) \exp\left(-\frac{E_{A,ion}}{k_B T}\right). \quad (5.5)$$

The peaks also broadened as the Na/K ratio decreased, so that obtaining a precise peak position from the 60/40 films was not possible. From the other compositions, Eq. (5.5) was used to determine $E_{A,ion}$ from the slope of $\ln T\mu_{ion}$ versus $1/T$. This analysis, illustrated in Fig. 5.6, yielded $E_{A,ion}$ in the range 0.66-0.99 eV which could reasonably correspond to oxygen vacancy migration [18][19][12][29][30].

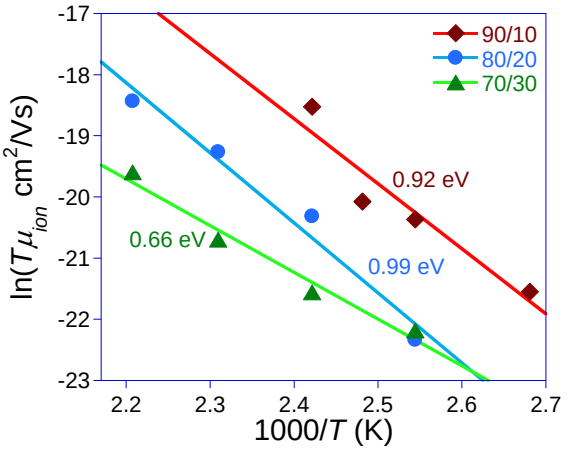

Figure 5.6 – *Arrhenius plots showing fits used for derivation of* $E_{A,ion}$.

The values of μ_{ion} roughly obtained at 140 °C, shown alongside $E_{A,ion}$ in Table 5.1, are similar to other reported values in thin films [19][12][31][32]. Although $V_O^{\bullet\bullet}$ migration appears to be the most likely cause, there are several other possibilities to consider. Na ions are notoriously mobile. Slightly lower $E_{A,ion}$≈0.4 eV have been found for Li, for example, in A-site deficient perovskites [33].

Much research has demonstrated ionic conduction in bulk BNT-based bulk ceramics, although we have not seen any reports showing dependence on the Na/K ratio [16][18][34][35][36]. We are aware only of our single previous report of ionic conduction in BNT-BKT thin films, which looked at Mn-doping in 80/20 films [5].

Current peaks came at shorter times as the Na/K ratio was increased, implying an increasing diffusivity of $V_O^{\bullet\bullet}$. The qualitative result was that a stoichiometry closer to the BNT side of the phase diagram resulted in increased oxygen conductivity, which could indicate a mechanism which relies upon the presence of Na or the symmetry of the lattice. The breadth of the peaks increased with the amount of K. This could be related to microstructure, with different mobilities for $V_O^{\bullet\bullet}$ diffusing through the bulk and grain boundaries resulting in peak spread. A more complicated picture includes polaron hopping of the Ti^{3+} and Ti^{4+} states in the cathode region, which can occur alongside $V_O^{\bullet\bullet}$ migration [37][38]. The net effect is a diffuse peak with some resistance degradation having some qualitative similarities to the *J-t* behavior in Fig. 5.5d. The resistance degradation effect appears weak, but this might be accounted for by some overlapping of dielectric relaxation.

Table. 5.1 – *Properties of (100-x)BNT-xBKT thin films.*

Na/K	$E_{A,ion}$ (eV)	μ_{ion} (cm^2/Vs)	E_c (kV/cm)	(100)/(101)	Surface Roughness
90/10	0.92	$2.2x10^{-11}$	66	0.099	7.8±1.1
80/20	0.99	$3.6x10^{-12}$	50	0.227	4.1±0.39
70/30	0.66	$1.1x10^{-12}$	41	0.924	3.4±0.32
60/40	N/A	$8.1x10^{-13}$	35	1.499	2.1±0.18

Polarization-electric field (*P-E*) hysteresis was performed in order to verify the time dependence of the ferroelectric polarization to exclude it as a possibility for causing the transient current peaks. The loops shown in Fig. 5.7 show that saturation was achieved in bipolar hysteresis using a 5 ms collection time. The transient currents in Fig. 5.5 were measured with E=100 kV/cm. The coercive fields, E_c, of these samples were well under this value (Table 5.1). Therefore, it is unlikely that the current peaks were due to the relatively rapid ferroelectric polarization.

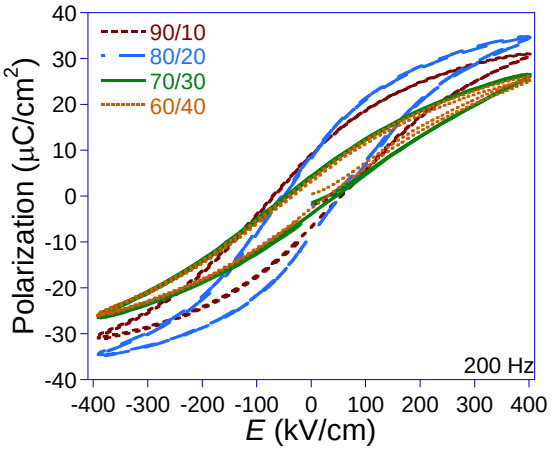

Figure 5.7 – *Polarization hysteresis loops for the films. The 80/20 MPB films had the highest polarizations. The 70/30 and 60/40 films showed the lowest* E_c.

Although the pronounced transient current peaks are only observed at higher temperatures, some initial increase in the *J* followed by a plateau, without a peak, occurs at lower temperatures (below 100 °C), particularly at higher fields. This could imply that some $V_O^{\bullet\bullet}$ redistribution is taking place during leakage current measurements which could affect, for instance, the ln*J*-ln*E* characteristics in Figs. 5.3 and 5.4. It may be possible to force $V_O^{\bullet\bullet}$ migration to one side of the device at high temperatures and quench the defects in place. If so, perhaps the effects on $V_O^{\bullet\bullet}$ distribution on leakage current could be studied directly.

This may also influence the fatigue behavior, where both the $V_O^{\bullet\bullet}$ distribution and electron injection are both thought to be relevant [39][40][41]. Efforts have been made to mitigate the effects of $V_O^{\bullet\bullet}$ migration on reliability in Ta_2O_5 and $(Ba,Sr)TiO_3$ capacitors. Strategies include embedding a thin, inert dielectric layer at the electrode interface, and doping [32][31]. Such methods may prove applicable to improving the fatigue resistance resistance degradation, as well.

Conduction properties are commonly attributed to changes in the oxygen vacancy concentration. In the case of BNT-BKT films, which are made from highly volatile cations, this is expected to be especially true. The more diffuse nature of the peaks in the *J-t* plots of the 70/30 and 60/40 films might imply a lower concentration of $V_O^{\bullet\bullet}$, and a lower concentration of charge carriers. In these films J_{Ohm} which proportional to charge carrier concentration and mobility, was consistently lower.

It is also possible that the variation in leakage current with N/K ratio is more dependent on the microstructure. Grain size, surface roughness, orientation, and tetragonality can play a strong role, and all of these were shown to vary with Na/K ratio as shown in Table 5.1. In the PZT system, films with tetragonal compositions were found to have higher leakage current than rhombohedral films, while leakage current was shown to increase with the degree of (111)/(100) orientation [42]. However, the (111) texture was enabled by an increase in the process temperature, which could have dominated trends seen in the leakage current. Other work has indicated that in films with similar microstructures and identical composition but different orientations, the leakage current is the same [43]. Microstructure can include many other factors such as grain size and grain boundary density, defect distributions through the grains and grain boundaries, and inhomogeneity through the film depth [44]. Surface properties such as roughness and the quality of the film-electrode interface, for example, can also have a strong effect on conduction. Poor quality interfaces are shown to lead to localized breakdown events [45].

For these films, there is a correlation between decreasing leakage current and increasing degree of (100) orientation. Both data sets seem to change rapidly from the 80/20 to 70/30 films. Other factors, including the μ_{ion} and the tetragonality (Fig. 5.1b) vary more gradually across the range of compositions tested. The leakage current, $V_O^{\bullet\bullet}$ diffusion, and E_c are all strongly affected by the Na/K ratio. The next steps are to directly examine the fatigue and leakage behavior dependence on the distribution of $V_O^{\bullet\bullet}$.

5.4 Conclusions

Thin film disc capacitor structures utilizing ferroelectric (100-*x*)BNT-*x*BKT, varying the ratio Na/K, were fabricated by CSD on $Pt/TiO_x/SiO_2/Si$ substrates. All films showed characteristics of the SCLC conduction mechanism in the steady state regime. However, leakage current through films of tetragonal compositions was markedly lower than those of rhombohedral or MPB compositions. This was also correlated to a marked increase in the ratio of the (200) and (101) orientations in the tetragonal films, which appear to show some form of incipient texture. Transient currents were also observed which appear to be due to oxygen vacancy diffusion

causing a modulation of the charge injection and transport properties of the film. A higher mobility for oxygen ion conduction was observed in films with higher Na/K ratios.

Acknowledgements

The authors acknowledge support of this work from the National Science Foundation under CAREER Grant No. DMR 115170.

References

[1] V. V. Schvartsman and D. C. Lupascu, "Lead-free relaxor ferroelectrics," *J. Am. Ceram. Soc.*, vol. 95, no. 1, pp. 1–26, 2011.

[2] J. Rödel, W. Jo, K. T. P. Seifert, E. M. Anton, T. Granzow, and D. Damjanovic, "Perspective on the development of lead-free piezoceramics," *J. Am. Ceram. Soc.*, vol. 92, no. 6, pp. 1153–1177, 2009.

[3] P. Muralt, "Recent progress in materials issues for piezoelectric MEMS," *J. Am. Ceram. Soc.*, vol. 91, no. 5, pp. 1385–1396, 2008.

[4] M. M. Hejazi and A. Safari, "Temperature-dependent leakage current behavior of epitaxial $Bi_{0.5}Na_{0.5}TiO_3$-based thin films made by pulsed laser deposition," *J. Appl. Phys.*, vol. 110, no. 10, p. 103710, 2011.

[5] J. Walenza-Slabe and B. J. Gibbons, "Leakage current phenomena in Mn-doped Bi(Na,K)TiO_3-based ferroelectric thin films," *J. Appl. Phys.*, vol. 120, p. 084102, 2016.

[6] T. Yu, K. W. Kwok, and H. L. W. Chan, "The synthesis of lead-free ferroelectric $Bi_{0.5}Na_{0.5}TiO_3$-$Bi_{0.5}K_{0.5}TiO_3$ thin films by sol-gel method," *Mater. Lett.*, vol. 61, no. 10, pp. 2117–2120, 2007.

[7] T. Y. Ansell and D. P. Cann, "High temperature piezoelectric ceramics based on $(1-x)[BiScO_3+Bi(Ni_{1/2}Ti_{1/2})O_3]-xPbTiO_3$," *Mater. Lett.*, vol. 80, pp. 87–90, 2012.

[8] S. E. Park and T. R. Shrout, "Characteristics of relaxor-based piezoelectric single crystals for ultrasonic transducers," *IEEE Trans. Ultrason. Ferroelectr. Freq. Control*, vol. 44, no. 5, pp. 1140–1147, 1997.

[9] P. Jarupoom, E. Patterson, B. Gibbons, G. Rujijanagul, R. Yimnirun, and D. Cann, "Lead-free ternary perovskite compounds with large electromechanical strains," *Appl. Phys. Lett.*, vol. 99, no. 15, pp. 1–4, 2011.

[10] H. Nagata, M. Yoshida, Y. Makiuchi, and T. Takenaka, "Large piezoelectric Constant and high Curie temperature of lead-free piezoelectric ceramic ternary system based on bismuth sodium titanate-bismuth potassium titanate-barium titanate near the morphotropic phase boundary," *Japanese J. Appl. Physics, Part 1 Regul. Pap. Short Notes Rev. Pap.*, vol. 42, no. 12, pp. 7401–7403, 2003.

[11] S. Lee and Y. Lee, "Dielectric properties of sol-gel derived PZT(40/60)/PZT(60/40) heterolayered thin films," *Thin Solid Films*, vol. 353, pp. 244–248, 1999.
[12] R. Meyer, R. Liedtke, and R. Waser, "Oxygen vacancy migration and time-dependent leakage current behavior of $Ba_{0.3}Sr_{0.7}TiO_3$ thin films," *Appl. Phys. Lett.*, vol. 86, no. 11, pp. 1–3, 2005.
[13] R. A. Eichel, "Structural and dynamic properties of oxygen vacancies in perovskite oxides-analysis of defect chemistry by modern multi-frequency and pulsed EPR techniques.," *Phys. Chem. Chem. Phys.*, vol. 13, no. 2, pp. 368–384, 2011.
[14] Y. A. Boikov, B. M. Goltsman, V. K. Yarmarkin, and V. V. Lemanov, "Slow capacitance relaxation in $(BaSr)TiO_3$ thin films due to the oxygen vacancy redistribution," *Appl. Phys. Lett.*, vol. 78, no. 24, pp. 3866–3868, 2001.
[15] H. Nagata, "Electrical properties and tracer diffusion of oxygen in some Bi-based lead-free piezoelectric ceramics," *J. Ceram. Soc. Japan*, vol. 116, pp. 271–277, 2008.
[16] S. Prasertpalichat, W. Schmidt, and D. P. Cann, "Effects of A-site nonstoichiometry on oxide ion conduction in $0.94Bi_{0.5}Na_{0.5}TiO_3$–$0.06BaTiO_3$ ceramics," *J. Adv. Dielectr.*, vol. 06, no. 02, p. 1650012, 2016.
[17] X. Liu, H. Fan, J. Shi, L. Wang, and H. Du, "Enhanced ionic conductivity of Ag addition in acceptor-doped $Bi_{0.5}Na_{0.5}TiO_3$ ferroelectrics," *RSC Adv.*, vol. 6, no. 36, pp. 30623–30627, 2016.
[18] M. Li, H. Zhang, S. N. Cook, L. Li, J. A. Kilner, I. M. Reaney, and D. C. Sinclair, "Dramatic influence of A-site nonstoichiometry on the electrical conductivity and conduction mechanisms in the perovskite oxide $Na_{0.5}Bi_{0.5}TiO_3$," *Chem. Mater.*, vol. 27, no. 2, pp. 629–634, 2015.
[19] S. Zafar, R. E. Jones, B. Jiang, B. White, P. Chu, D. Taylor, and S. Gillespie, "Oxygen vacancy mobility determined from current measurements in thin $Ba_{0.5}Sr_{0.5}TiO_3$ films," *Appl. Phys. Lett.*, vol. 73, no. 2, pp. 175–177, 1998.
[20] F. M. Pontes, L. S. Santos, S. R. Rissato, D. S. L. Pontes, E. Longo, E. R. Leite, S. Claro Neto, a. J. Chiquito, and P. S. Pizani, "Leakage current, ferroelectric and structural properties in $Pb_{1-x}Ba_xTiO_3$ thin films prepared by chemical route," *J. Phys. Chem. Solids*, vol. 69, no. 11, pp. 2796–2803, 2008.
[21] V. Bornand, S. Trolier-McKinstry, K. Takemura, and C. a. Randall, "Orientation dependence of fatigue behavior in relaxor ferroelectric–$PbTiO_3$ thin films," *J. Appl. Phys.*, vol. 87, no. 8, p. 3965, 2000.
[22] A. Wu, P. M. Vilarinho, V. V Shvartsman, G. Suchaneck, and A. L. Kholkin, "Domain populations in lead zirconate titanate thin films of different compositions via piezoresponse force microscopy," *Nanotechnology*, vol. 16, no. 11, pp. 2587–2595, 2005.
[23] F. Chiu, "A review on conduction mechanisms in dielectric films," *Adv. Mater. Sci. Eng.*, p. 578168, 2014.
[24] M. A. Lampert, "Double injection in insulators," *Phys. Rev.*, vol. 125, no. 1, pp. 126–141, 1962.
[25] M. A. Lampert and a. Rose, "Volume-controlled, two-carrier currents in solids: the injected plasma case," *Phys. Rev.*, vol. 121, no. 1, pp. 26–37, 1961.
[26] M. A. Lampert, "Volume-controlled current injection in insulators," *Reports Prog. Phys.*, vol. 27, no. 1, pp. 329–367, 1964.

[27] F. Neumann, Y. A. Genenko, R. Schmechel, and H. Von Seggern, “Role of diffusion on SCLC transport in double injection devices,” *Synth. Met.*, vol. 150, no. 3, pp. 291–296, 2005.
[28] I. Stolichnov and A. Tagantsev, “Control of leakage conduction of high-fatigue-endurance (Pb,La)(Zr,Ti)O_3 film ferroelectric capacitors with Pt/$SrRuO_3$ electrodes,” *Appl. Phys. Lett.*, vol. 75, no. 12, pp. 1790–1792, 1999.
[29] J. Zang, W. Jo, H. Zhang, and J. Rödel, “$Bi_{1/2}Na_{1/2}TiO_3$-$BaTiO_3$ based thick-film capacitors for high-temperature applications,” *J. Eur. Ceram. Soc.*, vol. 34, no. 1, pp. 37–43, 2014.
[30] R. Selvamani, G. Singh, V. S. Tiwari, and P. K. Gupta, “Oxygen vacancy related relaxation and conduction behavior in (1-x)NBT-x$BiCrO_3$ solid solution,” *Phys. Status Solidi Appl. Mater. Sci.*, vol. 209, no. 1, pp. 118–125, 2012.
[31] J. Wang and S. Trolier-Mckinstry, “Oxygen vacancy motion in Er-doped barium strontium titanate thin films,” *Appl. Phys. Lett.*, vol. 89, no. 17, pp. 1–4, 2006.
[32] J. P. Manceau, S. Bruyere, S. Jeannot, a. Sylvestre, and P. Gonon, “Metal-insulator-metal capacitors’ current instability improvement using dielectric stacks to prevent oxygen vacancies formation,” *Appl. Phys. Lett.*, vol. 91, no. 13, pp. 1–4, 2007.
[33] Y. Harada, H. Watanabe, J. Kuwano, and Y. Saito, “Lithium ion conductivity of A-site deficient perovskite solid solutions,” *J. Power Sources*, vol. 81–82, pp. 777–781, 1999.
[34] J. Hao, Z. Xu, R. Chu, W. Li, and J. Du, “Large electric-field-induced strain in $SrZrO_3$ modified $Bi_{0.5}(Na_{0.80}K_{0.20})_{0.5}TiO_3$ lead-free electromechanical ceramics with fatigue-resistant behavior,” *J. Alloys Compd.*, vol. 647, pp. 857–865, 2015.
[35] G. Liu, H. Fan, J. Shi, and Z. Liu, “Large strain and relaxation behavior in CeO_2 doped $Bi_{0.487}Na_{0.427}K_{0.06}Ba_{0.026}TiO_3$ piezoceramics,” *Ceram. Int.*, vol. 42, no. 3, pp. 3938–3946, 2016.
[36] J. Hao, Z. Xu, R. Chu, W. Li, and J. Du, “Lead-free electrostrictive $(Bi_{0.5}Na_{0.5})TiO_3$-$(Bi_{0.5}K_{0.5})TiO_3$-$(K_{0.5}Na_{0.5})NbO_3$ ceramics with good thermostability and fatigue-free behavior,” *J. Mater. Sci.*, vol. 50, no. 15, pp. 5328–5336, 2015.
[37] Y. Cao, S. Bhattacharya, J. Shen, C. a. Randall, and L. Q. Chen, “Role of polaron hopping in leakage current behavior of a $SrTiO_3$ single crystal,” *J. Appl. Phys.*, vol. 114, no. 22, 2013.
[38] W. Liu, G. Y. Yang, and C. A. Randall, “Evidence for increased polaron conduction near the cathodic interface in the final stages of electrical degradation in $SrTiO_3$ crystals,” *Jpn. J. Appl. Phys.*, vol. 48, no. 5, pp. 0514041–0514046, 2009.
[39] A. K. Tagantsev, I. Stolichnov, E. L. Colla, and N. Setter, “Polarization fatigue in ferroelectric films: basic experimental findings, phenomenological scenarios, and microscopic features,” *J. Appl. Phys.*, vol. 90, no. 3, pp. 1387–1402, 2001.
[40] M. Dawber, K. M. Rabe, and J. F. Scott, “Physics of thin-film ferroelectric oxides,” *Rev. Mod. Phys.*, vol. 77, no. October, pp. 1083–1130, 2005.
[41] R. Waser, T. Baiatu, and K.-H. Hardtl, “dc electrical degradation of perovskite-type titanates: 1, ceramics,” *J. Am. Ceram. Soc.*, vol. 73, no. 6, pp. 1645–1653, 1990.

[42] H. Funakubo, K. Tokita, T. Oikawa, M. Aratani, and K. Saito, “Comparison of crystal structure and electrical properties of tetragonal and rhombohedral Pb(Zr,Ti)O_3 films prepared at low temperature by pulsed-metalorganic chemical vapor deposition,” *J. Appl. Phys.*, vol. 92, no. 9, pp. 5448–5452, 2002.

[43] S. Kim, D. Park, H. Woo, D. Lee, J. Ha, C. Seong, I. Shim, and A. I. Kingon, “Orientation effects in chemical solution derived Pb($Zr_{0.3}$,$Ti_{0.7}$)O_3 thin films on ferroelectric properties,” *Thin Solid Films*, vol. 416, pp. 264–270, 2002.

[44] G. W. Dietz, M. Schumacher, R. Waser, S. K. Streiffer, C. Basceri, and a I. Kingon, “Leakage currents in $Ba_{0.7}Sr_{0.3}TiO_3$ thin films for ultrahigh-density dynamic random access memories,” *J. Appl. Phys.*, vol. 82, no. 1997, pp. 2359–2364, 1997.

[45] I. P. Lipscomb, P. M. Weaver, J. Swingler, and J. W. McBride, “The effect of relative humidity, temperature and electrical field on leakage currents in piezo-ceramic actuators under dc bias,” *Sensors Actuators, A Phys.*, vol. 151, no. 2, pp. 179–186, 2009.

6. Effect of annealing atmosphere pO_2 on leakage current in $80(Bi_{0.5}Na_{0.5})TiO_3$-$20(Bi_{0.5}K_{0.5})TiO_3$ thin films

6.1 Introduction

In the last decade, intense effort has been invested to find Pb-free alternatives to be used in ferroelectric and piezoelectric devices currently based on $Pb(Zr,Ti)O_3$ (PZT). These efforts are being driven by the Restrictions on Hazardous Substances (RoHS) guidelines enacted by the European Union, which aim to remove Pb from consumer devices. One likely candidate to replace PZT in at least some applications are solid solutions based upon $(100\text{-}x)(Bi_{0.5}Na_{0.5})TiO_3$-$x(Bi_{0.5}K_{0.5})TiO_3$ (BNT-BKT) . Among Pb-free films, BNT-based materials achieve a balance between large piezoelectric coefficients and high depolarization temperatures [1][2].

Thin film leakage currents in BNT-based thin films are not well understood relative to their Pb-based counterparts. Excess current can impair device efficiency and lead to early failure through resistance degradation [3][4][5]. The goal of this work is to iteratively optimize the properties of BNT-based thin films until they become competitive with PZT. Taking lessons from the development of PZT thin films through the past four decades, a deep understanding of the defects and microstructure of BNT-BKT is necessary for this to occur. It is known is that the A-site cations are highly volatile, making thin films prone to significant effects from defects. But, to date only a handful of studies have characterized the leakage current in BNT-based thin films [6][7][8].

Much more has been studied on the conductivity behavior of bulk ceramics. Recently, several studies have used annealing in different oxygen partial pressures (pO_2) to determine the carrier type of bulk ceramics. Kumar, *et al.* studied the effect of annealing at various pO_2 *in-situ* on $70BaTiO_3$-$30BiScO_3$ (BT-BS) and $95SrTiO_3$–$5Bi(Zn_{0.5}Ti_{0.5})O_3$ (ST–BZT) ceramics [9]. The stoichiometry was intentionally modified using deficient or excess quantities of A-site cations, causing the samples to be either *n*-type or *p*-type. The carrier type was inferred from impedance spectroscopy measurements in O_2, air, and ultra-high purity (UHP) N_2. The sample reoxidation fills oxygen vacancies, $V_O^{\bullet\bullet}$, which can be charge balanced either by generation of $h^{\bullet}$ or the trapping of $e^{/}$, modulating the carrier concentration and thus the sample resistivity and leakage current.

This technique was also used to characterize BNT-BT ceramics [10]. Another work demonstrated the effect of high temperature annealing at various pO_2 followed by measurements at lower temperatures [11]. Impedance spectroscopy is a difficult technique to implement in thin films, but similar inferences can also be applied to DC leakage current measurements in thin films. This is the approach taken here.

6.2 Experimental

Solution and film fabrication procedures above were based on those of Jeon, *et al.*, with slight modifications [12][13]. $(100\text{-}x)(Bi_{0.5}Na_{0.5})TiO_3\text{-}x(Bi_{0.5}K_{0.5})TiO_3$ solutions were prepared with optimized molar excesses of 8 mol% Bi, and 16 mol% each Na and K. Bismuth (III) acetate (99.9999%, Alpha Aesar) was dissolved in propionic acid (PAc). Sodium (I) acetate trihydrate (99%, Macron) and potassium (I) acetate (99%, Macron) were dissolved in dry methanol. In a glove box, titanium isopropoxide (98+ %, but better than 99% by assay, Alfa Aesar) was added to four molar equivalents of acetic acid pre-mixed with an equal volume of PAc. All precursors were measured by weight. The Bi solution was quickly added first to the Ti solution dropwise and stirred for at least one hour. Then, the Na/K solution was added and stirred for at least one hour. The resulting solution concentration was approximately 0.5 mol/L solvent.

Solutions were spin-cast on sputtered platinized silicon substrates (MEMS Exchange) at 3000 rpm for 30 s. Each layer was pyrolyzed at 325 °C for 4 min and crystallized at 700 °C for 10 min in a box furnace (Carbolite, CWF 1200). Platinum top electrodes were deposited by dc magnetron sputtering to complete the parallel plate capacitors.

Film thickness was obtained by variable angle spectroscopic ellipsometry (V-VASE, J.A. Woollam Co. Inc.), and x-ray diffraction (XRD) was used to ascertain phase purity (Bruker AXS D8 Discover).

Post-annealing of films was performed in a tube furnace flowing O_2, air, UHP (99.9999% pure) N_2, or a forming gas mixture of UHP 0.1 % H_2 balanced with N_2 (H_2/N_2), all at 400 °C for 20 min. Dielectric properties were measured on a HP 4192A impedance analyzer, using a 50 mV_{RMS} test signal. Leakage current and polarization

measurements were performed on a Radiant RT66B ferroelectric tester. Leakage current was determined by a 1 s combined soak and measure time. We adopt the convention where bias is considered to be applied to the top electrode.

6.3 Results and discussion

As-deposited films were 3 layers total, with a final thickness of 210 nm. There was no sign of second phases within the detection limits of the laboratory scale x-ray diffraction instrument, as demonstrated by Fig. 6.1. Films were polycrystalline with no apparent preferred orientation.

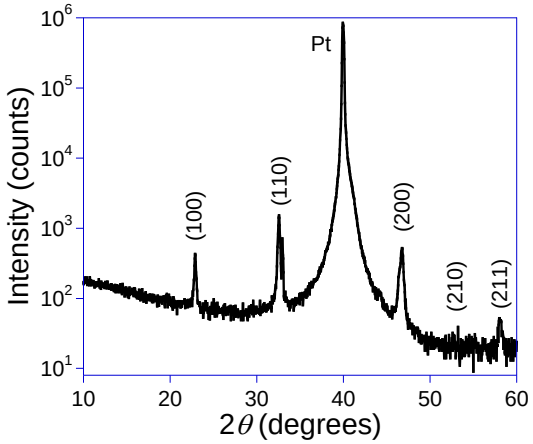

Figure 6.1 – *Films were crystallized phase pure, with no evidence of preferential orientation.*

The dielectric constant, ε_r, and loss, tanδ, were measured after the post-annealing procedures. These are shown in Fig. 6.2. In all of the films tanδ was low with no obvious trend (< 5% between 0.1~100 kHz), despite the presumed increase in the concentration of $V_O^{\bullet\bullet}$ caused by the reducing post-anneal. There was, however, a great disparity in ε_r which increased as the pO_2 during annealing increased. There are several explanations for this. Greater concentrations of defects (such as $V_O^{\bullet\bullet}$) can create a random potential field, which then can impede domain wall oscillations which are thought to contribute to ε_r, even at low fields [14][15]. A thin, low-ε_r dead layer formed at the top electrode interface could also lower the measured ε_r of the film, as well as diluting the ac measuring field across the sample [4][15][16].

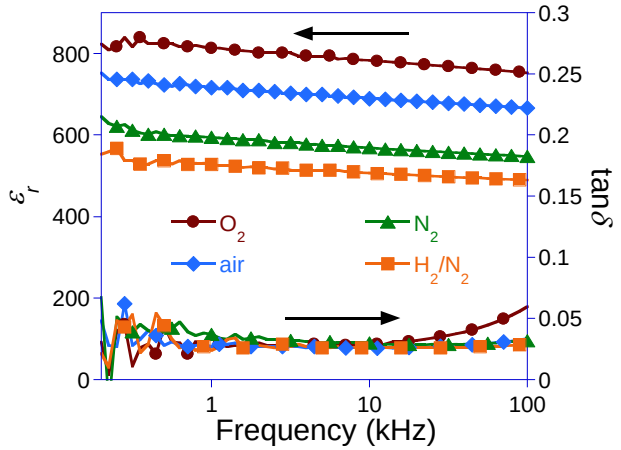

Figure 6.2 – *ε_r decreased after annealing in N_2 or H_2/N_2, and was increased by annealing in O_2. tanδ was not dependent upon the annealing pO_2.*

Leakage current plots measured at 100 °C are shown in Fig. 6.3. The measurements were made at elevated temperature in order to clearly see the full characteristics of the leakage current, while avoiding some low temperature anomalies described previously [8]. Incidentally, practical device design may also benefit from operation at elevated temperatures, since maintaining a constant temperature (and properties) above the ambient requires heating only, which is more simple to implement than active cooling. The leakage current increased consistently as the annealing atmosphere became more reducing. Oxygen annealing slightly decreased the leakage current. During post-annealing, the reoxidation and reduction reactions will affect the carrier type in the following ways, which can depend upon the atmosphere and temperature [9][11][17]. The reoxidation reaction generates holes,

$$\frac{1}{2}O_2 + V_O^{\cdot\cdot} \rightarrow O_O^x + 2h^{\cdot}, \qquad (6.1)$$

or traps electrons,

$$\frac{1}{2}O_2 + V_O^{\cdot\cdot} + 2e^{/} \rightarrow O_O^x. \qquad (6.2)$$

The effects of reducing atmospheres, given by the reverse of Eq. 6.2, during thin film crystallization have been extensively studied for the integration of ferroelectric films on base metal substrates [18][19]. Although there are significant differences between a crystallization step and a post-anneal, a reducing anneal is known to generate many oxygen vacancies which can degrade the film properties [4][20].

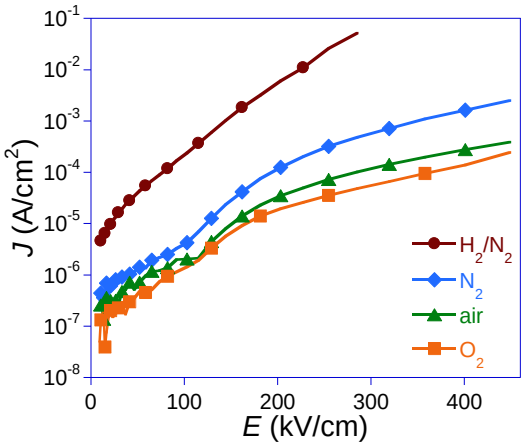

Figure 6.3 – *J-E plots for different pO_2 annealing atmospheres. Data were measured with sample held at 100 °C.*

There are many reports which note different results than reported here, i.e. increasingly lossy behavior upon an O_2 post-anneal, which recovers upon N_2 annealing. Specifically, it was shown that post-annealing symmetric $BaTiO_3$ (BTO) and $Ba(Sr,Ti)O_3$ (BST) thin film capacitors (with Pt top and bottom electrodes) in O_2 resulted in a large space charge along with a relaxation in tanδ near 100 Hz. Annealing in N_2 reversed this effect and regained the as-fabricated properties [21][22]. The proposed explanation was an interfacial accumulation of oxygen ions generated by charge transfer from the metal vacancy to an adsorbed oxygen. Other studies have observed an increase in ε_r and a decrease in tanδ and J upon annealing PZT and BST films in N_2 [23][24]. They formulated a mechanism based on nitrogen adsorption at film interfaces and grain boundaries, although no direct evidence for this was given.

Here, there was no dielectric relaxation peak observed in the expected frequency range of the tanδ plots of Fig. 6.2 after annealing in O_2. The apparent increase in the dielectric loss at high frequencies for the O_2 post-annealed samples is an artifact caused by a resonance in the LCR properties measurement circuit [25]. The current density in Fig. 6.3 increased after a reducing atmosphere post-anneal. The changes in leakage current are likely related to differences in the carrier concentration. Thus, the mechanism which most correctly describes the leakage data in terms of annealing atmosphere is that described by Eq. 6.2 (for oxidizing atmospheres) and its reverse path (for reducing atmospheres).

The data were generally a good fit for the space charge-limited current (SCLC) model, as can be seen in the ln*J*-ln*E* plots of Fig. 6.4. However, the SCLC characteristic curves were affected by the post-annealing. Current was largely Ohmic at low fields, $J_{Ohm} \propto E$, which occurs when the time required for the carriers to transit the film, τ_c, is greater than the time required for the dielectric relaxation of free carriers in the film, τ_d.

$$J_{Ohm} = q\mu n_0 E, \qquad (6.3)$$

where μ is the charge carrier mobility and q is the charge constant.

As voltage increases, eventually $\tau_c = \tau_d$, and the number of injected carriers n becomes comparable to the number of thermally generated carriers, n_0 [26]. At that point a space charge appears, and the SCLC appears. In the simple case of a single trap energy level (for instance a lone $V_O^{\bullet\bullet}$) this current, should exhibit a quadratic voltage dependence.

$$J_{tr} = \frac{9}{8}\frac{\mu\varepsilon_r\theta}{d}E^2, \qquad (6.4)$$

where θ is the ratio indicating the fraction of untrapped free charge carriers and d is the film thickness. As more electrons are injected into the device, the Fermi level begins to rise until it reaches the trap energy level. At that point there would be an instantaneous jump in current to a trap-free SCLC.

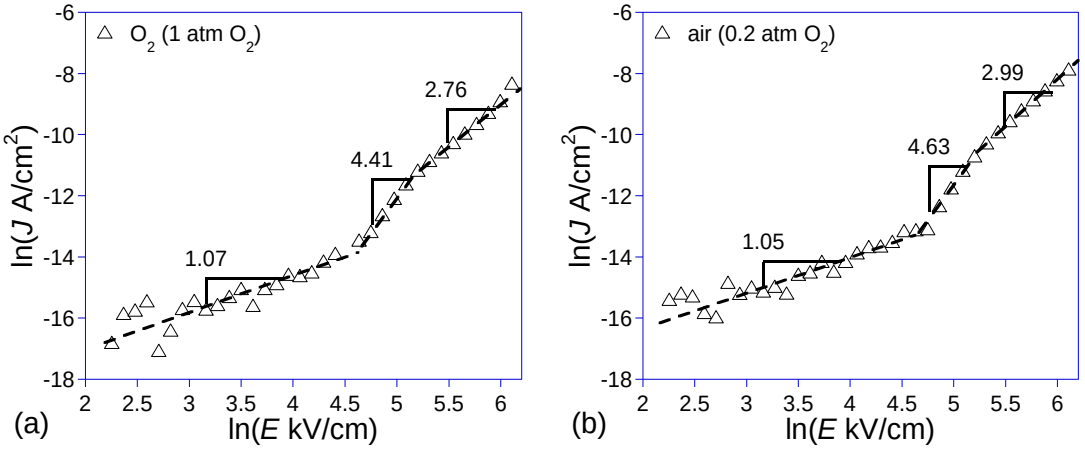

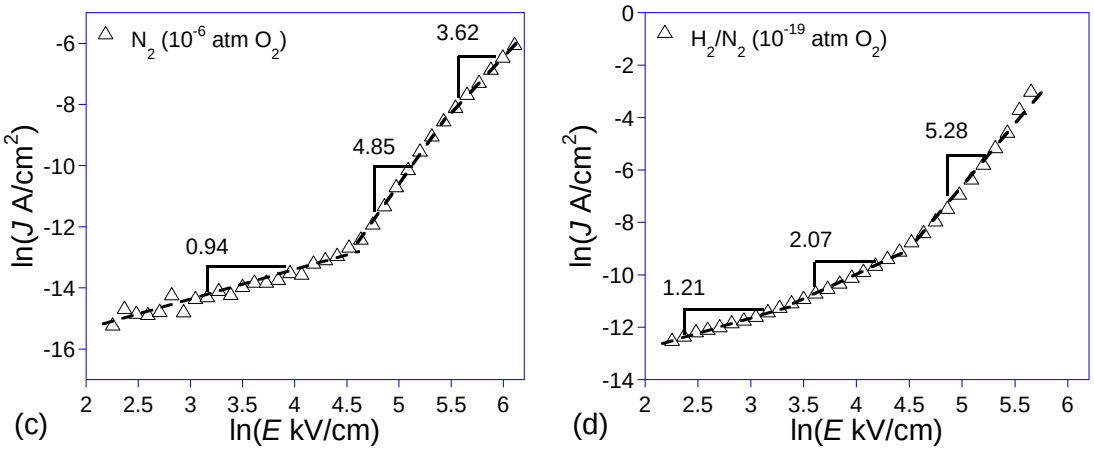

Figure 6.4 – *lnJ-lnE plots of films annealed in (a) O_2, (b) air, (c) N_2, and (d) H_2/N_2 showing the characteristic curves of the SCLC mechanism.*

The J_{tr} described above is not exactly what is seen in Fig. 6.4, which shows instead a region of slope of ln*J*-ln*E* around 4.5~6. This is likely caused by a distribution of trap levels resulting in the observed slope [27][28]. In a complex oxide with mixed volatile A-site cations, the defect levels may depend on the arrangement of the surrounding cations and vacancies. The polarization state of the individual domains may further split defect levels. Therefore, a distribution of trap levels is a reasonable scenario. The relationship for an exponential distribution of traps takes the form: [29]

$$J_{tr} = \frac{q^{1-l}\mu N_C}{d^l}\left(\frac{\varepsilon_r l}{n_t(l+1)}\right)^l \left(\frac{2l+1}{l+1}\right)^{l+1} E^{l+1}, l > 1. \qquad (6.5)$$

In Eq. 6.5, l is a parameter indicating the energy distribution of the trap levels, N_C is the density of states in the conduction band, and n_t is the density of traps. The characteristic curves appear to follow Eq. 6.5 for $J_{tr} \propto E^{(l+1)}$ for at least the O_2, air, and N_2 post-annealed films. The H_2/N_2 post-annealed films (the most reducing atmosphere) appear to show $J_{tr} \propto E^2$, followed by a second region $J_{tr} \propto E^{(l+1)}$. This could be explained by differences in the ratio of free charges to traps following post-annealing. Following crystallization, the leakage current is dominated by the high concentration of distributed traps, leading to $J_{tr} \propto E^{(l+1)}$. This is because of the loss of volatile cations during crystallization that are expected to create a large number of compensated defects such as $V_{Bi}^{'''}$ and $V_O^{\bullet\bullet}$.

$$2Bi_{Bi}^{X} + 3O_O^{X} \rightarrow 2V_{Bi}^{'''} + 3V_O^{\cdot\cdot} + \uparrow Bi_2O_3 \qquad (6.6)$$

This situation is maintained for higher pO_2 post-anneals. However, the ratio of free carrier to trap density is greatly increased through the formation of $V_O^{\cdot\cdot}$ during the highly reducing H_2/N_2 anneal. The excess of free carriers comes to dominate the response by filling more traps, leading to the $J_{tr} \propto E^2$ region in Fig. 6.4d [30].

At the highest fields, the current is normally given by the trap-free Child's law current,

$$J_{Ch} = \frac{9}{8}\frac{\mu\varepsilon_r}{d}E^2. \qquad (6.7)$$

The films annealed in O_2 and air showed instead a region $J_{Ch} \propto E^{\beta}$ (β is 2~3). The higher power can be caused by double injection of electrons and holes [31][32]. However, the analysis of the pO_2 post-annealed samples above suggests that electrons dominate the leakage current. A greater *E*-field dependence can also be caused by SCLC overlaid with the Frenkel effect, where the potential barrier for electrons to be emitted from a trap is lowered at high fields [33][34][35]. The exponent β varied from 2~3 from sample to sample, though the value is stable for subsequent measurements and consistent between different electrodes on the same sample. The cause of this variation is still under investigation, but β is clearly sensitive the fabrication process.

To summarize, while all of the films exhibited SCLC there were some differences in their characteristics. Annealing in a highly reducing atmosphere caused an apparent second SCLC region at lower *E*-fields, which could be caused by a distinct, deeper trap level. At higher fields the trap-free Child's law current appeared to be modified to a higher power dependence in the O_2 and air annealed samples. Films annealed in H_2/N_2 did not show a clear Child's law region, simply because the currents became too large to measure. J_{Ch} of films annealed in N_2 was ambiguous because the slope was generally greater than that annealed in O_2 and air, but seemed to be distinct from J_{tr}.

The same annealing experiments were conducted on films having the ternary compositions 95(80BNT-20BKT)-5Bi$(Ni_{0.5}Ti_{0.5})O_3$ and 95(80BNT-20BKT)-5$BaTi_{0.5}O_3$. The results were qualitatively identical to those presented above. Further experiments with higher percentages of the ternary compounds are planned which may reveal a more interesting trend.

It is common for thin film capacitor structures to be post-annealed in variously O_2, air, or N_2 to improve and stabilize the properties [36][37][38]. The reasons for the choice of gas are rarely given, although it the composition and previous processing of the film and electrodes will certainly have some bearing on the optimal gas type. Evidently, in the case of MPB 80BNT-20BKT films the optimal atmosphere for post-annealing is O_2 or air. It is suggested that this is because the films are primarily *n*-type conductive.

6.4 Conclusions

Thin films of 80BNT-20BKT were fabricated using CSD processing on platinized silicon substrates. The leakage current and dielectric properties were measured following post-annealing in different atmospheres. Leakage current followed the space charge-limited current mechanism. Post-annealing in the N_2 and H_2/N_2 also resulted in a reduction of the dielectric constant. Current density decreased after O_2 annealing, and increased after N_2 and H_2/N_2 annealing, which suggests *n*-type electron conduction. Characteristic ln*J*-ln*E* curves suggest that a distribution of trap levels in the films was consistently modified by exposure to the different atmospheres.

Acknowledgements

The authors acknowledge support of this work from the National Science Foundation under CAREER Grant No. DMR 115170.

References

[1] J. Rödel, W. Jo, K. T. P. Seifert, E. M. Anton, T. Granzow, and D. Damjanovic, "Perspective on the development of lead-free piezoceramics," *J. Am. Ceram. Soc.*, vol. 92, no. 6, pp. 1153–1177, 2009.

[2] S. O. Leontsev and R. E. Eitel, "Progress in engineering high strain lead-free piezoelectric ceramics," *Sci. Technol. Adv. Mater.*, vol. 11, no. 4, p. 044302, 2010.

[3] H. N. Al-Shareef and D. Dimos, "Leakage and Reliability Characteristics of Lead Zirconate Titanate Thin-Film Capacitors," *J. Am. Ceram. Soc.*, vol. 80, no. 12, pp. 3127–3132, 1997.

[4] W. L. Warren, D. Dimos, B. A. Tuttle, G. E. Pike, R. W. Schwartz, P. J. Clews, and D. C. McIntyre, "Polarization suppression in $Pb(Zr,Ti)O_3$ thin films," *J. Appl. Phys.*, vol. 77, no. 12, pp. 6695–6702, 1995.

[5] G. W. Dietz, M. Schumacher, R. Waser, S. K. Streiffer, C. Basceri, and a I. Kingon, "Leakage currents in $Ba_{0.7}Sr_{0.3}TiO_3$ thin films for ultrahigh-density dynamic random access memories," *J. Appl. Phys.*, vol. 82, no. 1997, pp. 2359–2364, 1997.
[6] M. M. Hejazi and A. Safari, "Temperature-dependent leakage current behavior of epitaxial $Bi_{0.5}Na_{0.5}TiO_3$-based thin films made by pulsed laser deposition," *J. Appl. Phys.*, vol. 110, no. 10, p. 103710, 2011.
[7] M. M. Hejazi, E. Taghaddos, and A. Safari, "Reduced leakage current and enhanced ferroelectric properties in Mn-doped $Bi_{0.5}Na_{0.5}TiO_3$-based thin films," *J. Mater. Sci.*, vol. 48, no. 9, pp. 3511–3516, 2013.
[8] J. Walenza-Slabe and B. J. Gibbons, "Leakage current phenomena in Mn-doped Bi(Na,K)TiO_3-based ferroelectric thin films," *J. Appl. Phys.*, vol. 120, p. 084102, 2016.
[9] N. Kumar and D. P. Cann, "Tailoring transport properties through nonstoichiometry in BaTiO3-$BiScO_3$ and $SrTiO_3$-Bi$(Zn_{1/2}Ti_{1/2})O_3$ for capacitor applications," *J. Mater. Sci.*, vol. 51, no. 20, pp. 9404–9414, 2016.
[10] J. Zang, M. Li, D. C. Sinclair, T. Frömling, W. Jo, and J. Rödel, "Impedance spectroscopy of $(Bi_{1/2}Na_{1/2})TiO_3$-$BaTiO_3$ based high-temperature dielectrics," *J. Am. Ceram. Soc.*, vol. 97, no. 9, pp. 2825–2831, 2014.
[11] N. Kumar, E. A. Patterson, T. Fromling, and D. P. Cann, "Conduction mechanisms in $BaTiO_3$-Bi $(Zn_{1/2}Ti_{1/2})O_3$ ceramics," *J. Am. Ceram. Soc.*, vol. 99, no. 9, pp. 3047–3054, 2016.
[12] Y. H. Jeon, E. A. Patterson, D. P. Cann, P. Mardilovich, W. Stickel, and B. J. Gibbons, "Large piezoresponse and ferroelectric properties of $(Bi_{0.5}Na_{0.5})TiO_3$-$(Bi_{0.5}K_{0.5})TiO_3$-Bi$(Mg_{0.5}Ti_{0.5})O_3$ thin films prepared by chemical solution deposition," *J. Am. Ceram. Soc.*, vol. 96, no. 7, pp. 2172–2178, 2013.
[13] Y. H. Jeon, E. A. Patterson, D. P. Cann, and B. J. Gibbons, "Dielectric and ferroelectric properties of $(Bi_{0.5}Na_{0.5})TiO_3$-$(Bi_{0.5}K_{0.5})TiO_3$-$BaTiO_3$ thin films deposited via chemical solution deposition," *Mater. Lett.*, vol. 106, pp. 63–66, 2013.
[14] G. Robert, D. Damjanovic, N. Setter, and a. V. Turik, "Preisach modeling of piezoelectric nonlinearity in ferroelectric ceramics," *J. Appl. Phys.*, vol. 89, no. 9, pp. 5067–5074, 2001.
[15] N. Bassiri-Gharb, I. Fujii, E. Hong, S. Trolier-Mckinstry, D. V. Taylor, and D. Damjanovic, "Domain wall contributions to the properties of piezoelectric thin films," *J. Electroceramics*, vol. 19, no. 1, pp. 47–65, 2007.
[16] I. Fujii, E. Hong, and S. Trolier-Mckinstry, "Thickness dependence of dielectric nonlinearity of lead zirconate titanate films," *IEEE Trans. Ultrason. Ferroelectr. Freq. Control*, vol. 57, no. 8, pp. 1717–1723, 2010.
[17] A. Podpirka, B. Viswanath, and S. Ramanathan, "Active low temperature oxidation as a route to minimize electrode-oxide interface reactions in nanoscale capacitors," *J. Appl. Phys.*, vol. 108, no. 2, 2010.
[18] J. Maria, K. Cheek, S. Streiffer, S. Kim, G. Dunn, and A. Kingon, "Lead zirconate titanate thin films on base-metal foils : an approach for embedded high-permittivity passive components," *J. Am. Ceram. Soc.*, vol. 84, no. 10, pp. 2436–2438, 2001.
[19] M. D. Losego, L. H. Jimison, J. F. Ihlefeld, and J. P. Maria, "Ferroelectric response from lead zirconate titanate thin films prepared directly on low-resistivity copper substrates," *Appl. Phys. Lett.*, vol. 86, no. 17, pp. 1–3, 2005.

[20] I. Bretos, T. Schneller, R. Waser, D. F. Hennings, S. Halder, and F. Thomas, "Compositional substitutions and aliovalent doping of $BaTiO_3$-based thin films on nickel foils prepared by chemical solution deposition," *J. Am. Ceram. Soc.*, vol. 93, no. 2, pp. 506–515, 2010.
[21] E. J. H. Lee, F. M. Pontes, E. R. Leite, E. Longo, R. Magnani, P. S. Pizani, and J. a Varela, "Effects of post-annealing on the dielectric properties of Au/$BaTiO_3$/Pt thin film capacitors," *Mater. Lett.*, vol. 58, no. 11, pp. 1715–1721, 2004.
[22] F. Pontes, E. Leite, and E. Longo, "Effects of the postannealing atmosphere on the dielectric properties of (Ba,Sr)TiO_3 capacitors: Evidence of an interfacial space charge layer," *Appl. Phys. Lett.*, vol. 76, no. 2000, pp. 2433–2435, 2000.
[23] G. Zhang, Q. Zou, P. Sun, X. Mei, and H. E. Ruda, "Influence of nitrogen annealing on electrical properties of lead zirconate titanate thin film deposited on titanium metal foil," *Mater. Lett.*, vol. 58, no. 5, pp. 706–710, 2004.
[24] C. S. Hwang, B. T. Lee, C. S. Kang, J. W. Kim, K. H. Lee, H. J. Cho, H. Horii, W. D. Kim, S. I. Lee, Y. B. Roh, and M. Y. Lee, "A comparative study on the electrical conduction mechanisms of ($Ba_{0.5}Sr_{0.5}$)TiO_3 thin films on Pt and IrO_2 electrodes," *J. Appl. Phys.*, vol. 83, no. 7, pp. 3703–3713, 1998.
[25] P. C. Joshi and S. B. Desu, "Structural and electrical studies on rapid thermally processed ferroelectric $Bi_4Ti_3O_{12}$ thin films by metallo-organic solution deposition," *J. Appl. Phys.*, vol. 80, p. 2349, 1996.
[26] F. Chiu, "A review on conduction mechanisms in dielectric films," *Adv. Mater. Sci. Eng.*, p. 578168, 2014.
[27] A. Rose, "Space-charge-limited currents in solids," *Phys. Rev.*, vol. 97, no. 6, pp. 1538–1544, 1955.
[28] M. A. Lampert, "Simplified theory of space-charge-limited currents in an insulator with traps," *Phys. Rev.*, vol. 103, no. 6, pp. 1648–1656, 1956.
[29] P. Mark and W. Helfrich, "Space-charge-limited currents in organic crystals," *J. Appl. Phys.*, vol. 33, no. 1, pp. 205–215, 1962.
[30] D. Joung, A. Chunder, L. Zhai, and S. I. Khondaker, "Space charge limited conduction with exponential trap distribution in reduced graphene oxide sheets," *Appl. Phys. Lett.*, vol. 97, no. 9, 2010.
[31] M. A. Lampert and a. Rose, "Volume-controlled, two-carrier currents in solids: the injected plasma case," *Phys. Rev.*, vol. 121, no. 1, pp. 26–37, 1961.
[32] M. A. Lampert, "Double injection in insulators," *Phys. Rev.*, vol. 125, no. 1, pp. 126–141, 1962.
[33] P. N. Murgatroyd, "Theory of space-charge-limited current enhanced by Frenkel effect," *J. Phys. D. Appl. Phys.*, vol. 3, no. 2, p. 308, 1970.
[34] D. Poplavskyy, W. Su, and F. So, "Bipolar charge transport, injection, and trapping studies in a model green-emitting polyfluorene copolymer," *J. Appl. Phys.*, vol. 98, no. 1, 2005.
[35] H. J. Chung, J. H. Jeong, T. K. Ahn, H. J. Lee, M. Kim, K. Jun, J. S. Park, J. K. Jeong, Y. G. Mo, and H. D. Kim, "Bulk-limited current conduction in amorphous InGaZnO thin films," *Electrochem. Solid-State Lett.*, vol. 11, no. 3, p. H51, 2008.
[36] Y. Masuda and T. Nozaka, "Investigation into electrical conduction mechanisms of Pb(Zr,Ti)O_3 thin-film capacitors with Pt, IrO_2 and $SrRuO_3$ top electrodes," *Japanese J.*

Appl. Physics, Part 1 Regul. Pap. Short Notes Rev. Pap., vol. 43, no. 9 B, pp. 6576–6580, 2004.
[37] B. A. Tuttle, T. J. Garino, J. A. Voigt, T. J. Headley, D. Dimos, and M. O. Eatough, "Relationships between ferroelectric 90 domain formation and electrical properties of chemically prepared $Pb(Zr,Ti)O_3$ thin films," in *Science and Technology of Electroceramic Films*, 1995.
[38] L. F. Schloss and P. C. McIntyre, "Polarization recovery of fatigued $Pb(Zr,Ti)O_3$ thin films: switching current studies," *J. Appl. Phys.*, vol. 93, no. 3, pp. 1743–1747, 2003.

7. Summary and future work

7.1 Summary

Thin films based on (100-*x*)BNT-*x*BKT were deposited on platinized silicon substrates via chemical solution deposition. Symmetric parallel plate capacitor structures were then fabricated by sputtering Pt top electrodes. Leakage current of all the films could be modeled using the space charge-limited current model. In general, the ln*J*-ln*E* characteristics of as-fabricated films indicated a distribution of shallow trap energy levels. Oxygen vacancy migration was studied from transient current peaks. These were found to be strongly dependent on the composition.

Mn-doping was studied as a function of Mn-dopant concentration and temperature in 80BNT-20BKT thin film capacitors. The onset *E*-field of strong injection increased with Mn-dopant concentration. At 2 mol% Mn, only Ohmic current was observed up to the highest temperatures and *E*-fields tested. Transient oxygen vacancy vacancy migration was observed and a marked difference was found between undoped and Mn-doped thin films which may indicate a difference in the mechanisms. Transient current peaks in Mn-doped films appeared to occur at short times but were not temperature dependent.

The binary system, (100-*x*)BNT-*x*BKT, was studied with *x*=10, 20, 30, and 40. Leakage current in the tetragonal compositions was markedly lower than those of rhombohedral or MPB compositions. Structural changes in the films included a change in the (100)/(101) XRD peak ratio which may indicate some incipient texture. The mobility for oxygen ion conduction appeared to increase with *x*. This was consistent, at least, with the large number of reports for oxygen vacancy migration in BNT and the relative scarcity of data for other compositions.

Capacitors made from films having the MPB composition 80BNT-20BKT, as well as the ternary compositions 95(80BNT-20BKT)-5Bi($Ni_{0.5}Ti_{0.5}$)O_3 and 95(80BNT-20BKT)-5$BaTiO_3$ were fabricated. Dielectric and leakage current characteristics were

measured following post-annealing in different atmospheres. Qualitatively, the response to post-annealing pO_2 was the same for all three compositions. ε_r was smaller in films post-annealed in reducing atmospheres, although the tanδ below 5 % remained unchanged. Current density decreased or remained nearly constant after annealing in oxidizing atmospheres, and increased after annealing in reducing atmospheres. This strongly suggests that *n*-type electron conduction is dominant in these films. Consequently, it should be possible to improve the properties of the films by crystallizing or post-annealing them in an oxygen environment. The ln*J*-ln*E* characteristics of H_2/N_2 post-annealed films were consistently altered. The curves could be explained by a transition from an excess of traps to an excess of electrons.

7.2 Future work

i. The effects of Mn-doping on BNT-BKT films was well established by the results presented in this work. However, a side effect of the improvement in leakage current was a decrease in the P_{max}, ε_r, and $d_{33,f}$. As noted before, previous reports have noted improvements in those same properties upon Mn-doping. The reason may be the creation of point defects which can pin domains, reducing the extrinsic contributions to polarization. Previous work on the PZT system has shown some improvement in the same properties with the addition of niobium to Bi-based thin films [1]. And PZT is commonly doped with lanthanum [2]. It is proposed to study the effects of co-doping BNT-BKT films with the acceptor species Mn^{2+} and the donors La^{3+} (on the A-site) and Nb^{5+} (on the B-site). Purposeful co-doping of acceptors and donors may also allow more direct control over the $V_O^{\bullet\bullet}$ stoichiometry and free charge density than modifying the cation excess, which has already been optimized. These

ii. A study should be undertaken of the relationship between $V_O^{\bullet\bullet}$ migration and fatigue in BNT-based films. The extent to which $V_O^{\bullet\bullet}$ participate in the fatigue and ageing process may be studied by analyzing these phenomena as a function of temperature using films with different initial distributions of defects. The first step is polarizing the point defects near the cathode under an *E*-field at temperature, then freezing them in by reducing the temperature under applied field. The films may then be aged under

ac and dc *E*-fields. The information from such experiments might be utilized to determine optimized heterostructures which preserve piezoelectric properties while minimizing fatigue and film ageing.

iii. Transient currents should be studied by observing relaxation phenomena such as thermally stimulated depolarization currents (TSDC) capacitance relaxation [3][4]. In a TSDC measurement, for example, the sample is poled as the sample cools from high temperature, freezing in the polarization. Depolarization currents corresponding to different polarization mechanisms are then measured in the absence of external field as the sample is again heated. An example for 80BNT-20BKT is shown in Fig. 7.1, where the peak around 160 °C coincides with the temperatures at which transient current were observed. By controlling the heating rate the kinetics of depolarization processes can be studied. Such measurements should be used to confirm new strategies for improving fatigue and ageing resistance in BNT-based thin films.

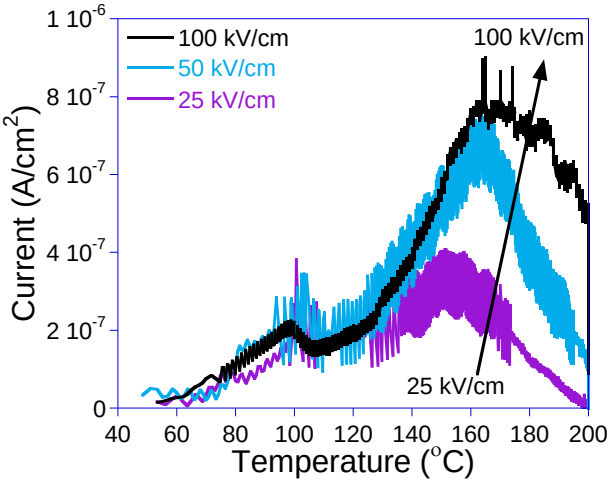

Figure 7.1 – TSDC measurements of an 80BNT-20BKT film poled at 200 °C.

iv. A study of the carrier type and concentration should be undertaken which compares the Hall voltage to results obtained from leakage current measurement of post-annealed films. While the post-annealing data given provides some evidence as to the carrier type, additional confirmation (including carrier concentration) might be achieved by using a Hall effect measurement. The measurement is typically done

with insulating bottom electrodes, such as MgO or SiO_2/Si. It is proposed to study the Hall effect in BNT-BKT-based films with Mn-doping and with the ternary end members $Bi(Ni_{0.5}Ti_{0.5})O_3$ and $Bi(Mg_{0.5}Ti_{0.5})O_3$.

References

[1] C. F. Chung, J. P. Lin, and J. M. Wu, "Influence of Mn and Nb dopants on electric properties of chemical-solution-deposited $BiFeO_3$ films," *Appl. Phys. Lett.*, vol. 88, no. 24, pp. 3–6, 2006.

[2] G. H. Haertling, "Ferroelectric thin films for electronic applications," *J. Vac. Sci. Technol. A Vacuum, Surfaces, Film.*, vol. 9, no. 3, p. 414, 1991.

[3] W. Liu and C. a. Randall, "Thermally stimulated relaxation in Fe-doped $SrTiO_3$ systems: II. degradation of $SrTiO_3$ dielectrics," *J. Am. Ceram. Soc.*, vol. 91, no. 10, pp. 3251–3257, 2008.

[4] Y. a. Boikov, B. M. Goltsman, V. K. Yarmarkin, and V. V. Lemanov, "Slow capacitance relaxation in $(BaSr)TiO_3$ thin films due to the oxygen vacancy redistribution," *Appl. Phys. Lett.*, vol. 78, no. 24, pp. 3866–3868, 2001.